2014/4

> From roads to fields, slag is safely used in a wide range of activities with high quality expectations.

EUROSLAG

The European Association representing metallurgical slag producers and processors

Applications

The steel industry produces not only metal, but also a by-product which has been successfully used in many construction or agriculture applications. Nowadays, about 87 wt% of ferrous slag produced in Europe is used for building purposes. Using slag instead of natural materials is a sustainable alternative with high durability in several applications.

Slag is…

… **proven over centuries.** From the beginning of the Iron Age, 800 B.C., through the invention of the blast furnace process in the 18th century, **slag products have been successfully marketed and put to beneficial** use.

… **ecological and intelligent.** With various techniques for further processing, slag is prepared for a wide range of applications - as building materials or fertilisers. Through recycling, a portion of the steel slag is reused in the blast furnace as calcium and iron bearing material.

… **for roads.** Slag is exceptionally well suited for road construction: as porous asphalt and as other construction materials with positive characteristics like durability and high skid resistance.

… **for bridges.** Slag is used for demanding construction projects such as bridges and skyscrapers.

… **for waterways.** In hydraulic engineering - such as in building locks, river bottoms and bank reinforcements - slag is a proven material.

… **as fertiliser.** Slag products have been successfully used as fertilisers for generations.

The use of slag is ecologically sound and economically smart.

"Porous asphalt" designed for noise reduction

Rheinkniebrücke in Düsseldorf, Germany

Steel slag asphalt used on heavily trafficked road

építőanyag

Journal of Silicate Based and Composite Materials

TARTALOM

CONTENT

Variability case study based on in-situ rebound hardness testing of concrete
Part 2. Statistical analysis of spatial variability parameters

ADORJÁN BOROSNYÓI ▪ Assoc. Prof., BME, Dept. of Construction Materials and Engineering Geology
▪ borosnyoi.adorjan@epito.bme.hu

Adorján Borosnyói
Civil engineer (MSc), PhD, Associate Professor at BME Dept. of Construction Materials and Engineering Geology. Main fields of interest: cracking and deflection of reinforced concrete, application of non-metallic (FRP) reinforcements for concrete structures, bond in concrete, nondestructive testing of concrete, supplementary cementing materials for high performance concretes, concrete technology. Member of the fib Task Group 4.1 „Serviceability Models", corresponding member of RILEM Technical Committee 249-ISC „Non destructive in situ strength assessment of concrete" and Chairman of the SZTE Concrete Division.

Abstract

Spatial variographic analysis has been performed on rebound index data collected in-situ at the bottom surface of a concrete floor over 130 m² of testing area. Possible use of geostatistical methods in terms of semivariogram, madogram and rodogram analysis was demonstrated. It has been revealed that the classical methods of geostatistics may be further refined for more satisfactory use in the spatial variability analysis of in-situ rebound hardness test results on concrete structures and a possible direction toward the use of empirical estimation of extremal coefficient functions is proposed.

Keywords: Structural concrete; Nondestructive testing (NDT); Rebound index; Spatial variability; Variogram

1. Introduction

Geostatistical methods are widely used in mining, geology, soil science, environmental science, hydrology, meteorology and recently, in engineering sciences for remote sensing, surface texture modelling, reliability and risk analysis, service life design and analysis of non-destructive testing [1-10]. The spatial variability analysis is well-described in the geostatistical literature for a long time; the reader may refer to the several textbooks available in geostatistics [11-16]. The use of the geostatistical methods for concrete structures is, however, still very much limited today [8-10].

In-situ non-destructive testing (NDT) of concrete structures may target strength estimation of structural concrete either to complete destructive testing or in the absence of drilled cores for laboratory testing [17-20]. In-situ assessment is frequently initiated by corrosion problems [21-23].

Structural concrete is a multiple-level heterogeneous composite material [24-25]. This multiple-level heterogeneity results both *inherent* (local) variability and *spatial* (regional) variability of the performance properties. Local variability can be analysed by conventional mathematical statistical methods. Analysis of regional variability needs spatial models – that are typically used in geostatistics.

2. Scope of the studies

In the first part of the present series of papers, inherent variability parameters were analysed corresponding to the independent test areas of a reinforced concrete slab, in terms of statistical location parameters, statistical variance parameters, statistical dispersion parameters and normality parameters [26].

In this second part, spatial variability is studied by contour plot, omnidirectional semivariogram (variogram of order 2), omnidirectional madogram (variogram of order 1) and omnidirectional rodogram (variogram of order 1/2).

3. Experimental

The experimental background was provided by the same structural element that was analysed in [26], i.e. the bottom surface of the top concrete slab of a framed, monolithic, subsoil concrete tunnel was studied, with dimensions of 25.0 m × 7.5 m and a thickness of 0.48 m [10]. The measuring region on the bottom surface was 22.0 m × 6.0 m. A total number of 42 test areas were selected for Schmidt rebound hammer testing. N-type original Schmidt rebound hammer was used. Eleven individual rebound index readings were recorded at each test area. The measurements were performed by the same operator.

4. Spatial variability analysis of the statistical parameters

In a practical situation, when eventually weaker regions of structural concrete within the element are present, it can be interesting to know that at which extent and in which directions the discrepancy is present and has influence on the performance properties. Geostatistical approaches can be adapted for the analysis of spatial variation. Geostatistics deals with spatially autocorrelated data (autocorrelation = correlation between elements of a series and others from the same series separated from each other by a given interval) and usually assumes that the differences between the values of samples are determined by the relative spatial distance of the samples and the mean and variance of the differences depend only on the relative distance [13]. Different *variograms* are introduced in geostatistical spatial correlation analysis that plot different correlation parameters of samples as the function of the separation between two spatial locations (referred to as *lag*; indicated with **h** in the present paper). Empirical *semivariogram* can be composed by the empirical semivariances of order 2 (see *Appendix*). Empirical *madogram* can be composed by the empirical semivariances of order 1. Empirical *rodogram* can be composed by the empirical semivariances of order 1/2. It is possible to compose *omnidirectional* variograms by taking into account all pairs of data in any possible relative distance, and it is possible to compose *unidirectional* variograms by taking those pairs of data into account that correspond to a given direction. This latter method was not applied in the present studies but would be used to find anisotropy in the
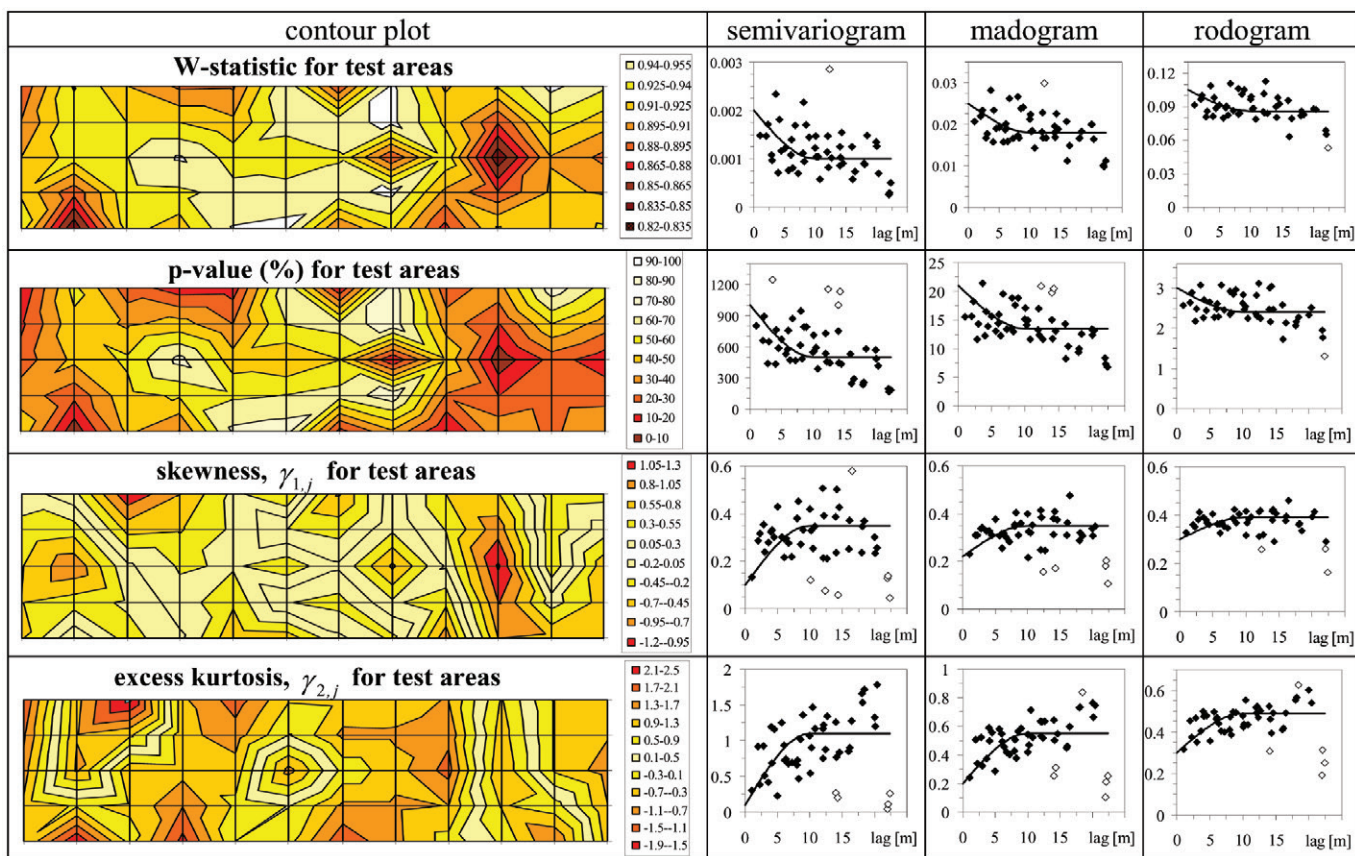
Fig. 1. Variographic analysis for the normality parameters
1. ábra Normalitási paraméterek variográfiai vizsgálata
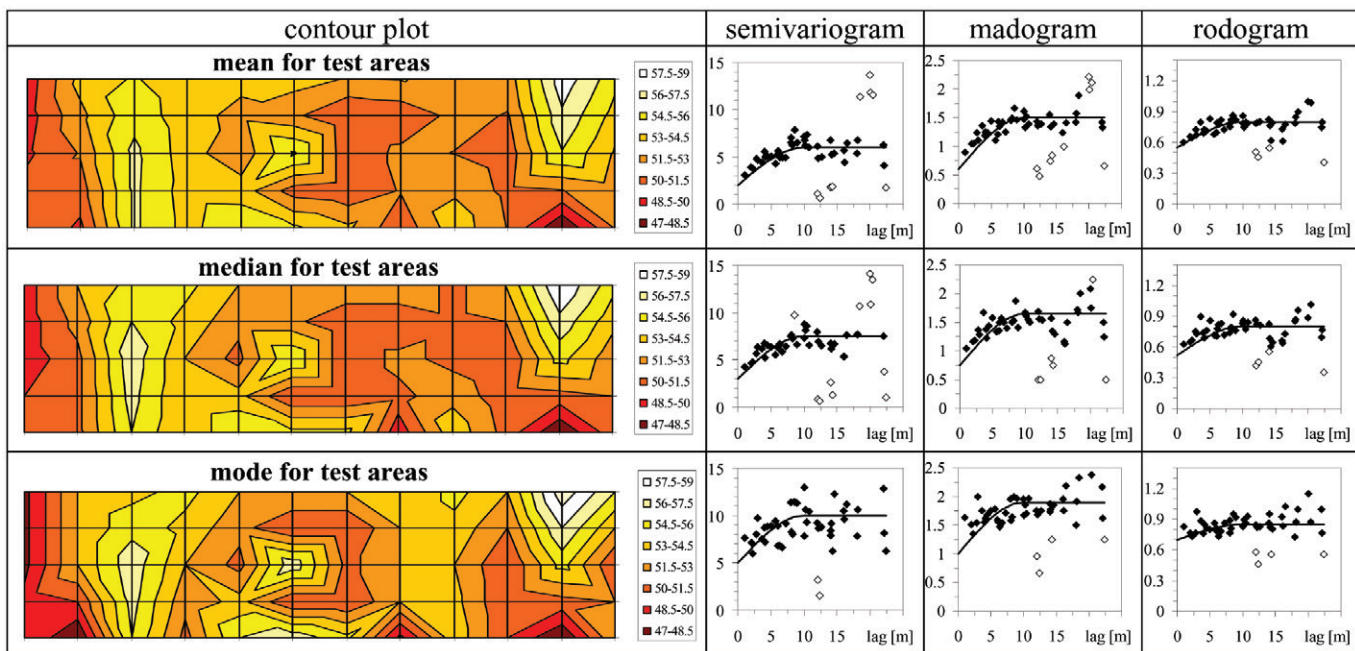
Fig. 2. Variographic analysis for the statistical location parameters
2. ábra Helyzeti statisztikai paraméterek variográfiai vizsgálata

spatial variability in a practical situation. In our nomenclature, the term variogram generally covers either semivariogram, or madogram or rodogram throughout the present paper.

If a variogram levels off (bounded) then a stationary random field can be used to model the observations [27].

According to the geostatistical modelling nomenclature, the *sill* is the value of the actual correlation parameter at which the variogram levels off and the *range* is the lag distance over which the actual correlation parameter is constant. The range distance can be referred to as *correlation distance,* over which
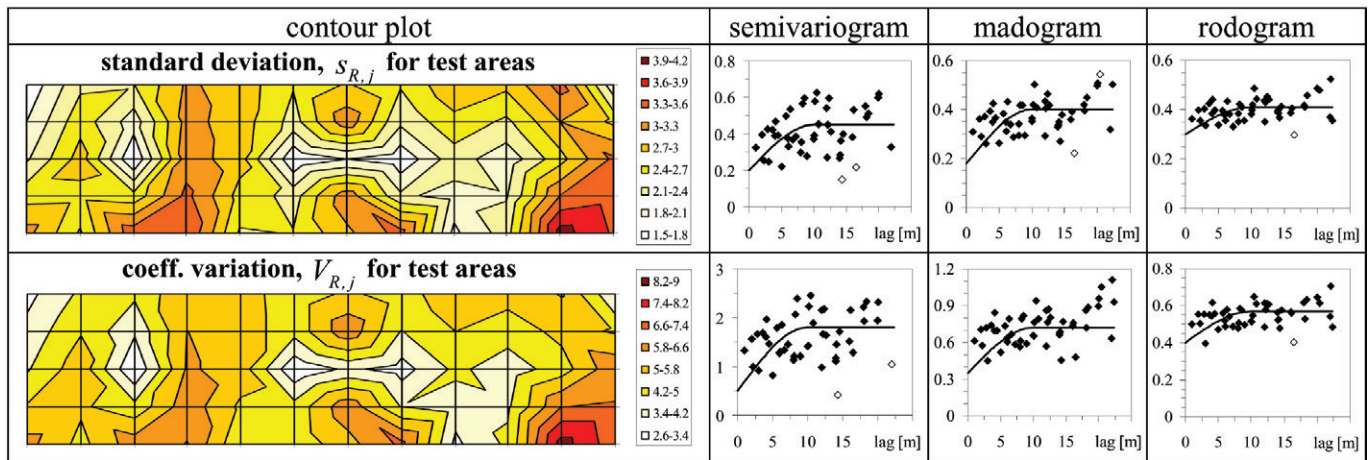
Fig. 3. Variographic analysis for the statistical variance parameters
3. ábra Variancia paraméterek variográfiai vizsgálata
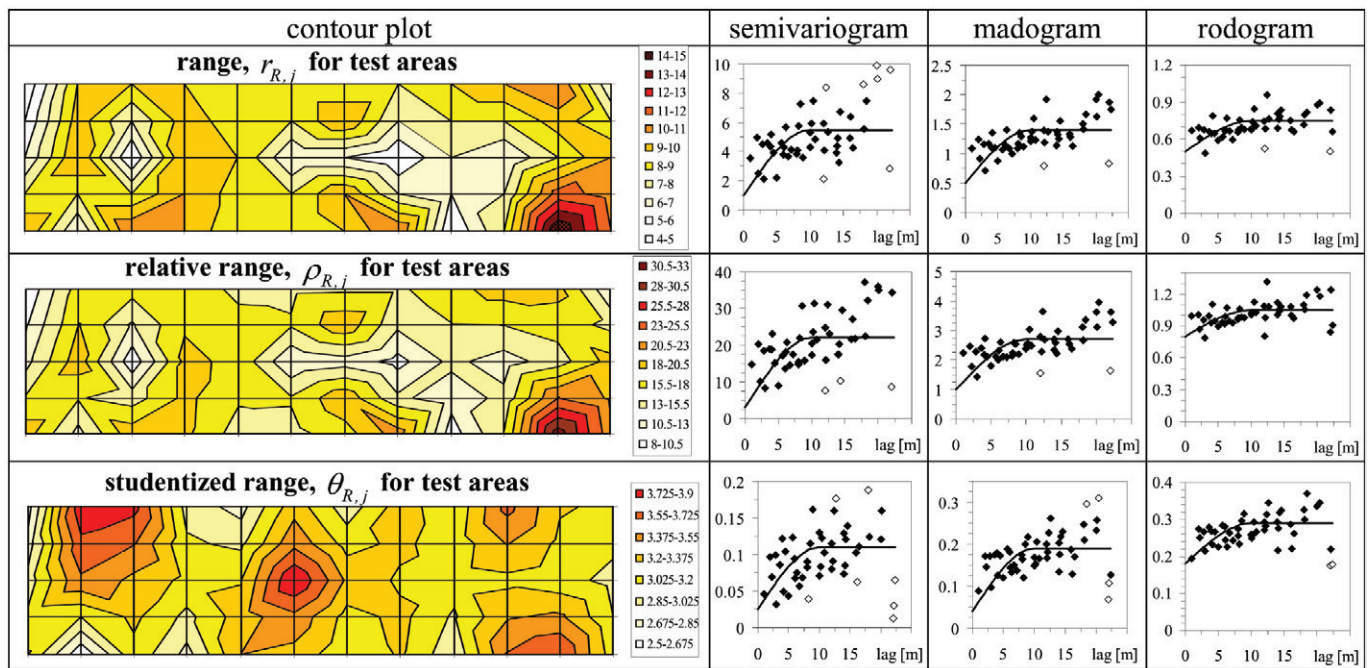
Fig. 4. Variographic analysis for the statistical dispersion parameters
4. ábra Terjedelem paraméterek variográfiai vizsgálata

lag the values of the variable are not correlated (independent). The correlation distance indicates the degree of similarity of the variable between two points as a function of the distance that separates them. The *nugget* is the value of the actual correlation parameter at distances smaller than the minimum lag of observations [13,16]. The nugget effect may provide information on strong differences in value within very short distances, or on a structural discontinuity, or on local material deterioration, or on an erroneous measurement [27].

Experimental variograms cannot be used directly for modelling and simulation. A wide range of variogram models are introduced in the literature of geostatistics. Typical models are the spherical, exponential, Gaussian, wave, nugget models [13,16]. Combined models are also used.

Figs. 1 to *4* summarize the empirical omnidirectional semivariograms, madograms and rodograms corresponding to the statistical parameters analysed. In the present study, the concrete slab has dimensions of 25.0 m × 7.5 m of which the studied region is 22.0 m × 6.0 m. In geostatistics, a common rule of thumb is accepted for the maximum lag in a variogram restricted to half of the diagonal of data extent [28]. It should be noted that lag is intentionally not limited to about 12 meters since one dimension of the slab is three times larger than the other. Restricting the variograms at maximum lag about half of the diagonal of data extent would not allow the diagrams to visibly level off and the sill could not be clearly determined. It should be also noted that intentionally no filtering was applied for the calculated correlation parameters but the suspected outlier values are indicated with empty markers in the variograms. Spherical model is fitted for all the 36 variograms that is also indicated in *Figs. 1* to *4*.

5. Discussion

The strength estimation of concrete by rebound hammer testing usually applies empirical relationships between statistical location parameters (mostly the mean and the median) and the compressive strength. It can be realized by studying the contour plots (*Fig. 2*) and as was shown earlier by linear correlations that the statistical location parameters are interrelated and a rather strong correlation is found between the mean and median values for the concrete floor in the present study [10,26]. It was also demonstrated that no correlation is found between the statistical location parameters and the statistical dispersion parameters; no correlation is found between the statistical location parameters and normality parameters; as well as no correlation is found between the statistical dispersion parameters and normality parameters [26].

It can be realized by studying the contour plots of *Fig. 3* and *4* that the interrelated nature of the range and the standard deviation demonstrated earlier [26] is visible for the concrete floor in the present study.

Contour plots of *Fig. 1* and *4* confirm the earlier findings [26] about the interrelated nature of the studentized range and excess kurtosis.

It can be realized in the spatial variability analysis that the semivariograms, madograms and rodograms can be constructed for all the twelve statistical parameters and all variograms are bounded and level off at a more or less clearly recognizable sill. Nugget is visible in all cases. It can be generally concluded that semivariograms are the most structured and rodograms are the least structured. The relative nugget effect (ratio of nugget and sill) is the strongest for the semivariograms and the least pronounced for the rodograms. Correlation ranges are very much similar for all types of variograms and for all the twelve statistical parameters studied. The correlation range was found to be about ten meters for the concrete floor in the present study.

The variograms constructed do not clearly demonstrate recognizable differences in the spatial variability *behaviour* (or trend) of the twelve statistical parameters studied, therefore, another direction for the spatial variability analysis is presented here towards the analogues of the analyses of max-stable stochastic processes.

6. Outlook

Skewed distributions were found to be fit with the best goodness of fit for the vast majority of frequency histograms of the local statistical parameters analysed for the concrete floor in the present study [26]. It was also demonstrated that best goodness of fit of the Fisher-Tippett (Generalized extreme value, GEV) distribution could be found for the individual rebound indices collected at the 42 individual test areas if no separation of data by location is applied [26]. Therefore, an analogue for the empirical estimation of the extremal coefficient function $\theta(\mathbf{h})$ is introduced in the present spatial variability analysis.

Extremal coefficient provides a measure of the degree of spatial dependence between locations for max-stable stochastic processes [29]. Similarly to the semivariogram that can be a tool for measuring dependence of Gaussian stochastic processes (due to the relationship with covariance), the madogram is proposed as a tool for measuring dependence in max-stable stochastic processes (due to the relationship with the extremal coefficient) [30]. It was shown that an empirical estimation of the extremal coefficient function can be constructed with the introduction of a modified madogram, the *F*-madogram $\upsilon(\mathbf{h})$, proposed for the distribution function *F* (values of *F*-madograms range from 0 to 1/6 corresponding to complete dependence and independence, respectively) [31]. The empirical estimation of the extremal coefficient function becomes:

$$\theta(\mathbf{h}) = \frac{1 + 2 \cdot \upsilon(\mathbf{h})}{1 - 2 \cdot \upsilon(\mathbf{h})}$$

where $\upsilon(\mathbf{h}) = \frac{1}{2N(\mathbf{h})} \sum_{i=1}^{N(\mathbf{h})} \left| F(\mathbf{u}_i + \mathbf{h}) - F(\mathbf{u}_i) \right|$

Since extreme value distributions were found to provide best goodness of fit for the statistical parameters tested in the present analyses, a simple analogue of the extremal coefficient function is proposed for the empirical madograms as follows:

$$\theta^{(1)}(\mathbf{h}) = \frac{1 + 2 \cdot \gamma^{(1)}(\mathbf{h})}{1 - 2 \cdot \gamma^{(1)}(\mathbf{h})}$$

where $\gamma^{(1)}(\mathbf{h})$ is the empirical semivariance of order 1 (see *Appendix*).

Results are indicated in *Fig. 5*. It should be noted that outliers (if any) were filtered and were not plotted in the graphical representation. It can be realized – on the contrary to the quite similar semivariogram, madogram or rodogram profiles – that the performance of the proposed dependence measure $\theta^{(1)}(\mathbf{h})$ is apparently separated to quite different behaviours.

There are statistical parameters for which *no trend* or very weak trend is visible: this is the case for *normality parameters* and for *statistical variance parameters*. Clear *linear trend* is visible for the *statistical dispersion parameters*. An *exponential variogram model* can be fitted to the *statistical location parameters*. The relative nugget effect of the proposed dependence measure $\theta^{(1)}(\mathbf{h})$ is found to be considerably different for the mean, for the median and for the mode.

At this time it is not clear how the proposed $\theta^{(1)}(\mathbf{h})$ dependence measure can be applicable for the spatial analysis of real in-situ measurements, but it emphasizes that some more sensitive parameters may be formulated than the semivariogram, madogram and rodogram, which behaviour was not found to be satisfactorily distinctive for the statistical parameters studied in the present analyses of rebound index data collected in-situ on a concrete floor. Future research is needed in this field.

7. Conclusions

Spatial variability analyses were carried out on in-situ rebound hammer test results collected at the bottom surface of a concrete floor over 130 m² of area tested. The following observations can be highlighted:
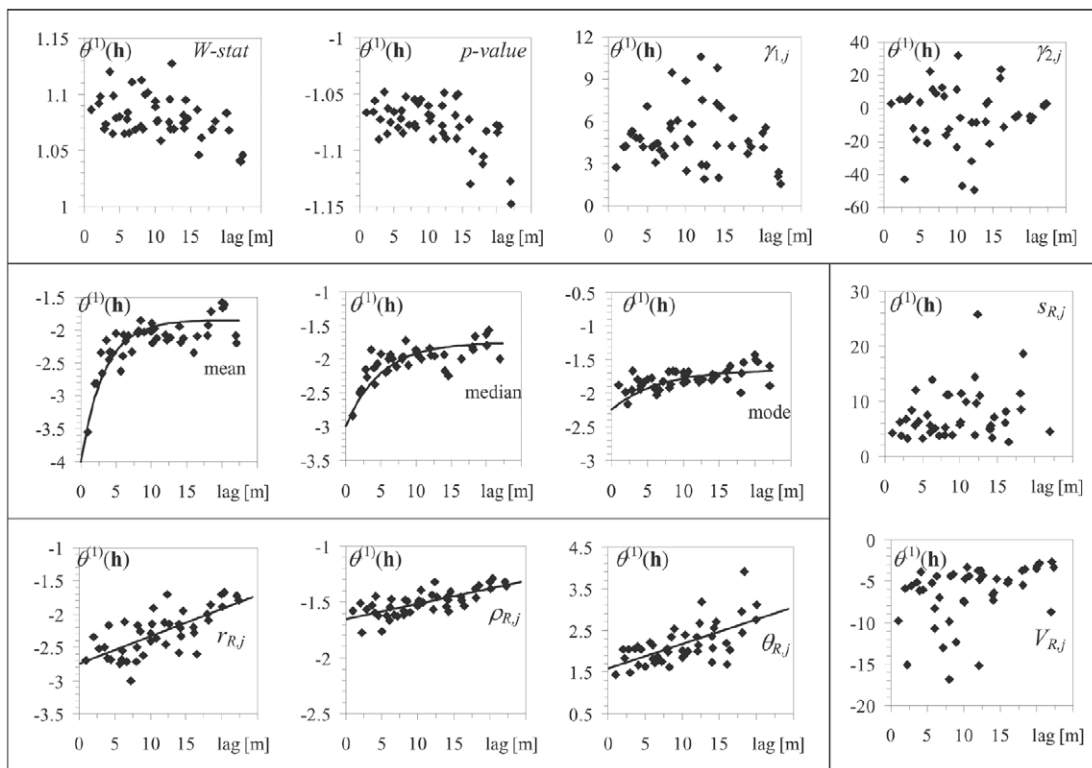
Fig. 5. Analogue for the empirical estimation of the extremal coefficient function for the statistical parameters studied
5. ábra Tapasztalati szélsőérték együttható függvény analógiájának illusztrálása a vizsgált statisztikai paraméterekre vonatkozóan

1. Semivariogram, madogram and rodogram can be successfully constructed for any statistical parameter to visualize spatial variability. Variograms always level off and nugget is clearly observed as well. It was found that restricting of the variograms at maximum lag about half of the diagonal of data extent is not practical for the geometry of the concrete floor studied.

2. It was found that semivariograms are the most structured and rodograms are the least structured. The relative nugget effect is the strongest for the semivariograms and the least pronounced for the rodograms. Correlation range was found to be about ten meters for the concrete floor in the present study, independently of the statistical parameter tested. Further studies on the influence of outlier filtering in the spatial variability analysis for rebound index data sets is addressed to future work since outliers may considerably increase both nugget and sill in variograms, as indicated in [32].

3. It was found that variograms constructed do not clearly demonstrate recognizable differences in the spatial variability behaviour for different statistical parameters, therefore, a dependence measure was introduced as an analogue for the empirical estimation of the extremal coefficient function (defined for *F*-madogram), with the simple adaptation of the idea to madograms. It was demonstrated that the performance of the proposed dependence measure is apparently separated to quite different behaviours; providing more sensitivity than semivariograms, madograms and rodograms.

8. Acknowledgements

References
[1] Matheron, G.: (1971) The Theory of Regionalized Variables and its Applications. École Nationale Supérieure des Mines de Paris
[2] Goovaerts, P.: (1999) Geostatistics in soil science: state-of-the-art and perspectives. *Geoderma,* Vol. 89, No. 1-2, 1999, pp. 1–45.
http://dx.doi.org/10.1016/S0016-7061(98)00078-0
[3] Tutmez, B. – Hatipoglu, Z.: (2007) Spatial estimation model of porosity. *Computers & Geosciences*, Vol. 33, No. 4, 2007, pp. 465–475.
http://dx.doi.org/10.1016/j.cageo.2006.07.008
[4] Balaguer, A. – Ruiz, L. A. – Hermosilla, T. – Recio, J. A.: (2010) Definition of a comprehensive set of texture semivariogram features and their evaluation for object-oriented image classification. *Computers & Geosciences*, Vol. 36, No. 2, 2010, pp. 231–240.
http://dx.doi.org/10.1016/j.cageo.2009.05.003
[5] Mlynarczuk, M.: (2010) Description and classification of rock surfaces by means of laser profilometry and mathematical morphology. *International Journal of Rock Mechanics and Mining Sciences,* Vol. 47, No. 1, 2010, pp. 138–149. http://dx.doi.org/10.1016/j.ijrmms.2009.09.004
[6] Stewart, M. G. – Mullard, J. A.: (2007) Spatial time-dependent reliability analysis of corrosion damage and the timing of first repair for RC structures. *Engineering Structures,* Vol. 29, No. 7, 2007, pp. 1457–1464. http://dx.doi.org/10.1016/j.engstruct.2006.09.004
[7] Li, J. – Masia, M. J. – Stewart, M. G., Lawrence, S. J.: (2014) Spatial variability and stochastic strength prediction of unreinforced masonry walls in vertical bending. *Engineering Structures,* Vol. 59, 2014, pp. 787–797.
http://dx.doi.org/10.1016/j.engstruct.2013.11.031
[8] Nguyen, N. T. – Sbartaï, Z. M. – Lataste, J. F. – Breysse, D. – Bos, F.: (2013) Assessing the spatial variability of concrete structures using NDT

techniques – Laboratory tests and case study. *Construction and Building Materials*, Vol. 49, 2013, pp. 240–250. http://dx.doi.org/10.1016/j.conbuildmat.2013.08.011

[9] Gomez-Cardenas, C. – Sbartaï, Z. M. – Balayssac, J. P. – Garnier, V. – Breysse, D.: (2012) Spatial sampling optimization of non-destructive testing measurements. 31ᵉᵐᵉˢ Rencontres Universitaires de l'AUGC, ENS Cachan, 29-31 May 2013. http://augc2013.ens-cachan.fr/Data/Articles/Contribution1187.pdf

[10] Borosnyói, A. – Szilágyi, K.: (2013) Studies on the spatial variability of rebound hammer test results recorded at in-situ testing. Építőanyag-JSBCM, Vol. 65, No. 4, 2013, pp. 102–106. http://dx.doi.org/10.14382/epitoanyag-jsbcm.2013.19

[11] Cressie, N. A. C.: (1993) Statistics for Spatial Data. *John Wiley & Sons* ISBN 978-0-471-00255-0

[12] Chilés, J. P. – Delfiner, P.: (1999) Geostatistics - Modeling Spatial Uncertainty. *John Wiley & Sons* ISBN 0-471-08315-1

[13] Clark, I.: (2000) Practical Geostatistics. *Geostokos Limited* ISBN 9780-9548911-1-4

[14] Wackernagel, H.: (2003) Multivariate Geostatistics - An Introduction with Applications. *Springer* ISBN 978-3-662-05294-5

[15] Diggle, P. – Ribeiro, J. P.: (2007) Model-based Geostatistics. *Springer* ISBN 978-0-387-48536-2

[16] Webster, R., Oliver, M. A. (2007) Geostatistics for Environmental Scientists. *John Wiley & Sons* ISBN 978-0-470-02858-2

[17] Breysse, D. – Martinez-Fernandez, J. L.: (2013) Assessing concrete strength with rebound hammer: review of key issues and ideas for more reliable conclusions. *Materials and Structures*, Vol. 46, 2013, Published online: 25 July 2013 http://dx.doi.org/10.1617/s11527-013-0139-9

[18] Vona, M. – Nigro, D.: (2013) Evaluation of the predictive ability of the in situ concrete strength through core drilling and its effects on the capacity of the RC columns. *Materials and Structures*, Vol. 46, 2013, Published online: 23 November 2013 http://dx.doi.org/10.1617/s11527-013-0214-2

[19] Antonaci, P. – Bocca, P. – Grazzini, A.: (2006) In situ determination of toughness indices of fibre reinforced concrete. *Materials and Structures*, Vol. 39, pp. 283–290. http://dx.doi.org/10.1617/s11527-005-9003-x

[20] Masi, A. – Chiauzzi, L.: (2013) An experimental study on the within-member variability of in situ concrete strength in RC building structures. *Construction and Building Materials,* Vol. 47, 2013, pp. 951–961. http://dx.doi.org/10.1016/j.conbuildmat.2013.05.102

[21] Long, A. E. – Henderson, G. D. – Montgomery, F. R.: (2001) Why assess the properties of near-surface concrete? *Construction and Building Materials,* Vol. 15, No. 2-3, 2001, pp. 65–79. http://dx.doi.org/10.1016/S0950-0618(00)00056-8

[22] Villagrán Zaccardi, Y. A. – Bértora, A. – Di Maio, A. A.: (2013) Temperature and humidity influences on the on-site active marine corrosion of reinforced concrete elements. *Materials and Structures,* Vol. 46, 2013, pp. 1527–1535 http://dx.doi.org/10.1617/s11527-012-9994-z

[23] Tay, D. C. K. – Tam, C. T.: (1996) In situ investigation of the strength of deteriorated concrete. *Construction and Building Materials,* Vol. 10, No. 1, 1996, pp. 17–26. http://dx.doi.org/10.1016/0950-0618(95)00057-7

[24] Pekár, G.: (2013) Simple basic model for concrete and its application. Part 2 - Factors that influence compressive strength and drying shrinkage. Építőanyag-JSBCM, Vol. 65, No. 3, 2013, pp. 76–84. http://dx.doi.org/10.14382/epitoanyag-jsbcm.2013.15

[25] Pekár, G.: (2013) Simple basic model for concrete and its application. Part 3 - Factors affecting consistency, material balance equations and mix design. Építőanyag-JSBCM, Vol. 65, No. 4, 2013, pp. 118–126. http://dx.doi.org/10.14382/epitoanyag-jsbcm.2013.22

[26] Borosnyói, A.: (2014) Variability case study based on in-situ rebound hardness testing of concrete. Part 1. Statistical analysis of inherent variability parameters. Építőanyag-JSBCM, Vol. 66, No. 3, pp. 85–91. http://dx.doi.org/10.14382/epitoanyag-jsbcm.2014.16

[27] Breysse, D. – Marache, A.: (2011) Some Estimates on the Variability of Material Properties. In: Construction Reliability Safety, Variability and Sustainability (Eds. Baroth, J., Schoefs, F., Breysse, D.). *John Wiley & Sons* ISBN 978-1-84821-230-5

[28] Coombes, J.: (2005) Handy Hints For Variography - Guidelines for variogram analysis. *Snowden Associates Pty Ltd.*

[29] Ribatet, M.: (2009) A User's Guide to the SpatialExtremes Package. École *Polytechnique Fédérale de Lausanne Switzerland*

[30] Cooley, D. S.: (2005) Statistical Analysis of Extremes Motivated by Weather and Climate Studies: Applied and Theoretical Advances. PhD thesis. *University of Colorado*

[31] Cooley, D. S. – Cisewski, J. – Erhardt, R. J. – Jeon, S. – Mannshardt, E. – Omolo, B. O. – Sun, Y.: (2012) A Survey of Spatial Extremes: Measuring Spatial Dependence and Modeling Spatial Effects. *REVSTAT-Statistical Journal*, Vol. 10, 2012, pp. 135–165. ISSN 1645-6726

[32] Oliver, M. A. – Webster, R.: (2014) A tutorial guide to geostatistics: Computing and modelling variograms and kriging. *Catena,* Vol. 113, 2014, pp. 56–69. http://dx.doi.org/10.1016/j.catena.2013.09.006

Appendix. Formulae

The following regional statistical measures were calculated for the spatial variability during the present analyses:

empirical semivariance of order 2:

$$\gamma^{(2)}(\mathbf{h}) = \frac{1}{2N(\mathbf{h})}\sum_{i=1}^{N(\mathbf{h})}\left[f(\mathbf{u}_i + \mathbf{h}) - f(\mathbf{u}_i)\right]^2$$

empirical semivariance of order 1:

$$\gamma^{(1)}(\mathbf{h}) = \frac{1}{2N(\mathbf{h})}\sum_{i=1}^{N(\mathbf{h})}\left|f(\mathbf{u}_i + \mathbf{h}) - f(\mathbf{u}_i)\right|$$

empirical semivariance of order 1/2:

$$\gamma^{(1/2)}(\mathbf{h}) = \frac{1}{2N(\mathbf{h})}\sum_{i=1}^{N(\mathbf{h})}\left|f(\mathbf{u}_i + \mathbf{h}) - f(\mathbf{u}_i)\right|^{1/2}$$

where:

$\mathbf{u}$ vector of spatial coordinates (with 2D components x and y),
$f(\mathbf{u})$ variable under consideration as a function of spatial location,
$\mathbf{h}$ lag vector representing separation between two spatial locations,
$f(\mathbf{u+h})$ lagged value of variable under consideration,
$N(\mathbf{h})$ the number of data pairs separated by lag $\mathbf{h}$.

Local statistical measures were defined in Part 1. of present series of papers.

Esettanulmány betonszerkezet helyszíni keménységméréséről
2. rész. A mérőhelyek közötti változékonyság statisztikai elemzése
A cikk egy vasbeton födém alsó felületének 130 m²-es szakaszán végzett, helyszíni Schmidt-kalapácsos vizsgálatok eredményeinek statisztikai elemzését mutatja be. A mérőhelyek közötti változékonyság statisztikai paramétereinek elemzése és az egyes paraméterek közötti korreláció vizsgálata történik meg. Bemutatásra kerül, hogy a vizsgálat alá vont statisztikai jellemzőkre elkészíthető olyan félvariogram, madogram és rodogram, amely szférikus modellel modellezhető. A cikk ismertet egy új eljárást a tapasztalati szelsőérték együttható függvény analógiájaként megfogalmazott variográfiai elemzésre.
Kulcsszavak: betonszerkezet; roncsolásmentes vizsgálat; keménység; visszapattanási érték; mérőhelyek közötti változékonyság; variogram

Formation of Catalyst Model Dispersed of Pd on a thin MgO (100)

Baara Fatma
is a lecturer at the Department of Physics in the Badji Mokhtar University Annaba and has wide range experiments in investigation of surface properties of solids. Dr. Baara is author of several scientific papers in which the interface properies and behaviors of solids are described.

Abdelbaki Chemam
is an expert of applied physics and has a wide range experiments in scanning tunneling microscopy. He is author of several scientific papers in field of condensed matter physics and theory. Prof. Cheman is a regular participant of ic-cmtp conferences in Lillafüred (Hungary) and at present his Research Gate ranking has achived the 6.06 value.

Dr. Fatma BAARA ▪ Laboratory of surfaces and interfaces of solids studies - (LESIMS) – Department of Physics, Faculty of Sciences,Badji Mokhtar University-Annaba-Algeria. ▪ baarafatma@yahoo.fr
Prof. Abdelbaki CHEMAM ▪ Preparatory School for Science and Technology of Annaba, Annaba 23000, Algeria. ▪ a.chemam@epst-annaba.dz

Abstract

The nucleation kinetics or the formation of a catalyst model dispersed for the system Pd /thin MgO (100) are calculated by developing many programs using Fortran software. This simulation is based upon parameters studied in situ by transmission electron microscopy (TEM), related to the first quantitative study on the nucleation and the growth. Palladium nanoparticles deposited on thin MgO are tested in the temperature range 573–1073 K and deposition time of 1000 s. The nucleation kinetics are interpreted according to the theory of random nucleation. The general scheme is consisting of three stages namely, nucleation, growth and coalescence. The saturation density of clusters decreases when the substrate temperature increases following Arrhenius law. This behavior is in agreement with a recent AFM study for Ag/MgO and Au/MgO. The phenomenon of coalescence is explained via island migration process. It is shown that the coalescence occurs more rapidly when the substrate temperature is high.
Keywords: catalists, crystals, magnesium-oxide, nucleation kinetics, palladium

1. Introduction

Nowadays, nano-objects provide a promising research for the identification of new fundamental properties of the materials and their potential technological applications. Much effort is devoted to understand the physical and chemical properties of materials, which can serve as model catalyst systems. Consequently, fundamental studies have been carried out on a range of heterogeneous catalyst, for example, metal islands grown on thin films [1-11] or on single-crystals surfaces [12-18]. Palladium deposits on the MgO(1 0 0) surface have become one of the most widely used model systems, and have given rise to many detailed experimental studies [19-21]. Although the main microscopic steps governing nucleation and growth of the films are now understood, detailed characterization of these processes has proven difficult. Earlier, empirical and theoretical studies of Pd over single crystals MgO, investigated defect nucleation [22-28] when nucleation centres occupy minority of sites. On the other hand, the results of nucleation kinetics over thin films governed by random nucleation [1,29], each atomic site is potentially a nucleation centre. In this study, we build upon many experimental and theoretical studies [1, 30-32] have been carried out to understand these processes. The aim of this work is to investigate the microscopic mechanisms, which can calculate various parameters related to the quantitative study focusing on the nucleation, growth and coalescence of Pd / thin MgO (100) using Fortran software.

1.1 Transmission electron microscopy experiments

To understand the first quantitative study of nucleation and growth of Pd on thin layer of MgO(100),we exploited the experimental work of Henry *et al* [1],who used transmission electron microscopy and electron diffraction at high energy to measure the Pd island density as a function of time a given temperature and a constant flux. Firstly, the MgO (100) / LiF (100) / NaCl (100) composite layer is achieved which serves as support. Palladium is then deposited with a flux of 1×10^{13} atoms cm$^{-2}\times$ s^{-1} and exposure time of 10 to 240 s on a substrate heated at temperatures between 573 and 673K. After deposition, the Pd islands are in situ characterized with a transmission electron microscopy (TEM) to determine the island density. The results are interpreted according to the theory of random nucleation. The energy of adsorption and diffusion of palladium on MgO (100) are derived from the latter theory. It was possible to vary the average size of particles in the range 0.8 - 3.5 nm. The obtained cluster density varies from 0.6 to 3×10^{12} cm^{-2} however the covered area of the substrate surface is of 0.4 to 15 percent.

1.2 Over view of nucleation and growth theories

Nucleation on a surface has been discussed in both classical thermodynamic and in atomistic terms, and both have a long history. Classical nucleation theory was developed by Volmer [33]. From this theory, the critical nucleus is only one atom, which means that the dimer is already stable. In that case, the classical nucleation theory is no longer applicable. The growth process occurs by accretion of adatoms. It is described by the atomistic nucleation theory, which has been developed by Zinsmeister [32]. In this case, the critical nucleus composites of two atoms and the supercritical nuclei do not dissociate. The probability of adsorption is equal to one and that only single atom can return in the phase steam. The frequency of nucleation is then determined by the frequency of meeting of adsorbed atoms.

1.2.1 Nucleation kinetics

The rate equations given by Zinsmeister express the variation with time of the number of clusters of size i:

$$\frac{dn_i}{dt} = \omega_{i-1}\, n_{i-1} - \omega_i\, n_i \text{ for i} = 2,3\ldots\infty \qquad (1)$$

ω_i is the attachment frequency of an adatom to a cluster containing i atoms which is expressed by:

$$\omega_i = \sigma_i\, D\, n_i \tag{2}$$

where σ_i is the capture number for a cluster of size i. We have to integrate the system of differential equations in order to calculate the number of nuclei present on the substrate. For sake of simplicity Zinsmeister assumes that it is a constant between 1 and 4. From this scheme the nucleation frequency is:

$$J = 2\,\omega_1\, n_1 \tag{3}$$

Supposing that the growth is negligible, the density of adatoms is equal to the stationary value:

$$n_1 = F\,\tau \tag{4}$$

where F is the flux of atoms impinging on the substrate and τ the mean life time of an adatom before desorption. Then, combining equations (2) and (4) the nucleation rate becomes:

$$J = 2\sigma_1\, D\, F^2 \tau^2 \tag{5}$$

The nucleation rate is proportional to the square of the impinging flux for a homogeneous substrate without defects.

1.2.2 Growth kinetics.

Zinsmeister has solved the system of differential equation assuming a constant value for the attachment frequency (ω_i) [18]. However by this treatment several characteristics of the growth of clusters are not taken into explanation. Several researches have tried to treat more precisely the calculation of the attachment frequencies [34–39]. In the typical growth, the diffusion of adatoms is limited by desorption and the diffusion length X_s of an adatom is:

$$X_s = (D\tau)^{1/2} \tag{6}$$

where D_s is the surface diffusion coefficient. It is expressed by:

$$D_s = (a_0^2\, v_d)\exp\left(-\frac{E_d}{KT_s}\right) \tag{7}$$

Then the mean life time of a physisorbed molecule can be explained by:

$$\tau = (1/v_a)\exp\left(\frac{E_a}{KT_s}\right) \tag{8}$$

where E_a and E_d is the adsorption and the diffusion energy, and a_0 the jump distance, of the order of the surface repeat distance, say 0.2-0.5 nm[40], v_d and v_a the frequency factors for the diffusion and the adsorption process, K the Boltzmann constant and T_s the substrate temperature. In a general case, the growth rate of a cluster can be expressed by a power law of the deposition time.

$$R(t) = R_0\, t^p \tag{9}$$

The exponent for any experimental has been calculated in the case of the lattice approximation for 3D clusters.

1.2.3 Coalescence

The transformation of two touching nuclei into one nucleus can be described by a time constant shown by Nichols and Mullins [41]:

$$\tau_c = 0.2\left(\frac{R^4}{B}\right) \quad with \quad B = \frac{\gamma\,\Omega^{4/3}D_s}{K\,T_s} \tag{10}$$

where R is the radius of the coalescing spheres, γ the surface free energy and Ω the atomic volume of Pd.

1.2.4 Algorithm

We have been developed many programs exploiting Fortran software. The following list details this mapping.
1. Pd deposition flux rate on MgO (100) is 1.13×10^{13} atoms cm$^{-2}\times$ s^{-1}.
2. Pd atoms are deposited randomly onto the surface with activation energy of about 0.22 eV.
3. Pd nanoparticles deposited on thin MgO are tested in the temperature range 573–1073 K and deposition time of 1000 s.
4. Pd islands are approximated to be three-dimensional clusters.
5. The diffusion of adatoms is limited by desorption. Hence, the values of the surface diffusion are calculated by combination of Equations (6) and (7).
6. The entry parameters are: the velocity of nucleation, velocity of growth, the average mean life time, the surface repeat distance, the diffusion length, the surface free energy, the atomic volume of Pd, the activation and the diffusion energies.

2. Results

Fig. 1 shows the variation of cluster density as a function of exposure time at different substrate temperatures ranging from 573K to 1073K and a constant palladium flux 1×10^{13} atoms cm$^{-2}\times$ s^{-1}. For Ts = 573K and 673K, we can see that the density of clusters is increasing rapidly after 10 to 70 s (see table 1) due to the large adsorption energy for the Pd adatom confirming the nucleation stage, up to a plateau (saturation density) corresponding to n_s = 3×10^{12} cm^{-2} and 1.6×10^{12} cm^{-2} respectively. A similar behavior is observed for the remaining substrate temperatures till the coalescence occurrence, were the cluster density decreases. It is worth to note that the cluster density decreases when the temperature increases.
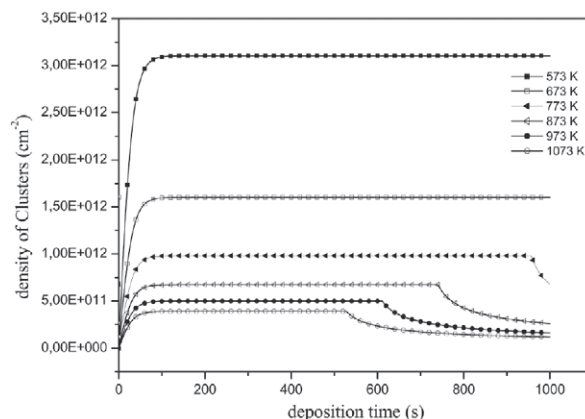

Fig. 1. Nucleation kinetics of Pd on MgO (100) at different substrate temperatures for a palladium flux 1×10^{13} atoms cm$^{-2}\times$ s^{-1}.
1. ábra A Pd nukleáció kinetikája MgO (100) vékony rétegen különböző szubsztrátum hőmérsékleten, ha a palládium fluxus nagysága 1×10^{13} atom/cm^{2}s.

t (s)	573 K	673 K	773 K	873 K	973 K	1073 K
10	9.39E11	4.85E11	2.97E11	2.03E11	1.50E11	1.18E11
70	3.02E12	1.56E12	9.58E11	6.56E11	4.86E11	3.81E11
τ_c	No	No	9.80E11	6.71E11	4.98E11	3.90E11
1000	3.02E12	1.60E12	6.77E11	2.59E11	1.64E11	1.19E11

Table 1. Calculated of the cluster density (cm⁻²) at different substrate temperatures (K) and deposition times (s).

1. táblázat A különböző K hőmérsékletekre és „lerakódási" időkre (sec) számított klaszter-sűrűségek (cm²).

In *Fig. 2*, the saturation density is plotted in an Arrhenius diagram. It is represented by the equation: $n_s = B_0 \times \exp(E / K \times T_s)$. When the activation energy E is equal to 0.22 ± 0.05 eV, B_0 (pre exponential factor) is 3.63×10^{10} cm⁻². We show that it increases when the substrate temperature decreases. This behavior is in agreement with a recent AFM study for Ag/MgO [42], Au/MgO (100) [43] and our previous studies by TEM [1] on the same system.
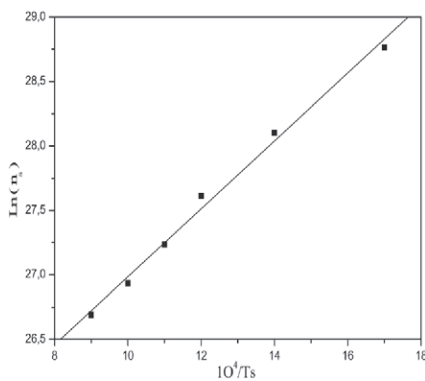

Fig. 2. Arrhenius plot of the saturation density of palladium clusters on MgO (100).

2. ábra A palládium klaszerek Arrhenius féle telítettségi sűrűsége az MgO (100) vékony rétegen.

Fig. 3 and *4* show the variations of the covered area (A) and the coalescence parameter (B) as a function of substrate temperatures obtained under the same conditions. We see that the fraction of covered area decreases when deposition temperature rises. An opposite behavior is observed for the coalescence parameter.
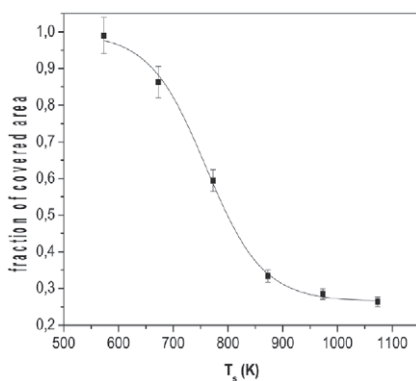
Fig. 3. Variation of the covered area (A) as a function of substrate temperatures with deposition times 1000s.

3. ábra Az 1000 másodperc idő alatt lerakódott felület (A) nagyságának változása a szubsztrátum hőmérséklet függvényében
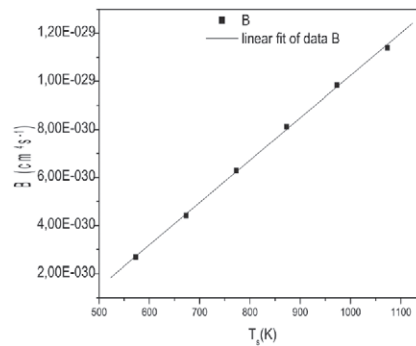
Fig. 4. Variation of the coalescence parameter (B) as a function of substrate temperatures with deposition times 1000s.

4. ábra Az 1000 sec. idő alatt létrejött egyesülések száma (B) a szubsztrátum hőmérséklet függvényében.

3. Discussion

From our previous empirical result for Pd/MgO thin film, the initial nucleation curves suggest the occurrence of a random nucleation mechanism. The theory of this nucleation process is expressed by the kinetic equations of Zinsmeister [32]. Robinson and Robins [30] have given analytical solutions in two limit cases, namely at low and high temperature. In this work, we focus on the high substrate temperatures(regime of incomplete condensation), where the particle number density is given by:

$$n = n_s \tanh\left(t/\tau\right) \tag{11}$$

when the random nucleation model is used ,the calculated curves in the first stage agree well with the experimentally measured [1] time dependencies of island density (see nucleation regime in *Fig. 1*). Hence, the curves show a plateau as a maximum particle density reached at the end of the nucleation regime characterizing the Volmer Weber growth. The value of saturation of the island density is an important parameter which determine the mode of thin film growth. The latter has an evident influence on the physicochemical properties of the obtained thin films [28]. The linear behavior of the Arrhenius plot observed for the temperature dependence of the saturation density of clusters has been also found in the case of Ag / Ar-cleaved MgO(1 0 0) [42], Au /MgO(1 0 0) [43] and Pd/ UHV-cleaved MgO(1 0 0) [44,45].

$$n = n_s \left(1 + t/\tau\right)^{-3/m}, \text{ with } m = 7 \tag{12}$$

The coalescence curves were better fitted with a Cluster diffusion model [31] rather than Ostwald ripening model.

The most crucial parameter in our results is the coalescence time. It is defined as the mean time for two clusters that come into contact to coalesce. From Eq. (10), we can note that two parameters are important to determine the duration of the coalescence stage, which are R and B. One can also notice the influence of the deposition temperature, that modifies the clusters coalescence time. It is clearly seen that clusters coalesce more rapidly at high temperature [46]. This phenomenon is explained by the process of island migration.

The process of island migration in this calculation is essentially described by the parameter B. The derived B values from *Fig. 4* are not high enough meaning that the process of island density coalescence is not ignored even at the initial stages of deposition [47]. The mechanism of coalescence which can be expected at

such a low value of surface coverage is the migration of islands on the surface, prior to the mechanism of immobile islands in which the coalescence occurs at high values of surface coverage when the islands touch each other [48].

The surface coverage does not depend on B parameter, but it strongly depends on the cluster density and the shape of the particles. The fraction of the substrate covered by the clusters, which is considered as the contact surface of the half sphere is a circle can be written as:

$$A = \frac{\pi}{4} n D^2 \qquad (13)$$

In this range of temperatures, the diameter (D) of the clusters follows a power law: $D_o \, t^p$ with $0.33 < P < 0.55$. At 573K and 673K, our previous experimental work yielded values of D_o; P equals 0.024 nm, 0.8 and 0.372 nm, 0.39 respectively [1]. The obtained values are used for the calculated curves of the covered area of the substrate surface.

As indicated in the last section the cluster density decreases when the substrate temperature increases due to the increased ad-atom mobility [34]. In addition, we assumed that D is relatively constant with a low error ($\Delta D / D = 11\%$). Accordingly, the fraction of the substrate covered by the particles decreases and the decrease is more pronounced when the coalescence occurs. This behavior is in good agreement with growth rate of the particles in the case of the random nucleation theory [49].

4. Conclusions

In the present study, we have simulated the microscopic mechanisms, which can calculate various parameters related to the formation of Pd / thin MgO (100) using FORTRAN software. The formation kinetics follows a general scheme consisting of three stages: nucleation, growth and coalescence. It is determined that saturation density obeys an Arrhenius law with activation energy of 0.22 eV as a fit parameter. It is observed that the variation of island density upon time reaches the saturation. In some cases the cluster density decreases slowly after a saturation regime. The latter decrease is interpreted via the processes of islands migration .It is shown that the coalescence time and the fraction of the substrate covered by the clusters decrease when the temperature increases. Furthermore, the clusters coalesce more rapidly when the temperature increases.

5. Acknowledgment

References

[1] Chapon, C. – Henry, C. R. – Chemam, A.: (1985) Formation and characterization of small Pd particles deposited on MgO as a model catalyst, Surface Science, Vol. 162, No. 1–3, 1985, pp. 747–754 http://dx.doi.org/10.1016/0039-6028(85)90975-6

[2] Stiehler, Christian – Pan, Yi – Schneider, Wolf-Dieter – Koskinen, Pekka – Häkkinen, Hannu – Nilius, Niklas – Freund, Hans-Joachim: (2013) Electron quantization in arbitrarily shaped gold islands on MgO thin films, Physical Review B, Vol. 88, 2013, 115415 http://dx.doi.org/10.1103/PhysRevB.88.115415

[3] Shao, Xiang – Cui, Yi – Schneider, Wolf-Dieter – Nilius, Niklas – Freund, Hans-Joachim: (2012) Growth of Two-Dimensional Lithium Islands on CaO(001) Thin Films, The Journal of Physical Chemistry C, Vol. 116, No. 33, 2012, pp. 17980–17984 http://dx.doi.org/10.1021/jp306328c

[4] Wang, Hui-Feng – Ariga, Hiroko – Dowler, Rhys – Sterrer, Martin – Freund, Hans-Joachim: (2012) Surface science approach to catalyst preparation – Pd deposition onto thin Fe_3O_4(1 1 1) films from $PdCl_2$ precursor, Journal of Catalysis, Vol. 286, 2012, pp. 1–5 http://dx.doi.org/10.1016/j.jcat.2011.09.026

[5] Freund, Hans-Joachim – Heyde, Markus – Nilius, Niklas – Schauermann, Swetlana – Shaikhutdinov, Shamil – Sterrer, Martin: (2013) Model studies on heterogeneous catalysts at the atomic scale: From supported metal particles to two-dimensional zeolites, Journal of Catalysis, Vol. 308, 2013, pp. 154-167 http://dx.doi.org/10.1016/j.jcat.2013.06.007

[6] Hansen, K. H. – Worren, T. – Stempel, S. – Lægsgaard, E. – Bäumer, M. – Freund, H. J. – Besenbacher, F. – Stensgaard, I.: (1999) Palladium Nanocrystals on Al_2O_3: Structure and Adhesion Energy, Physical Review Letters, Vol. 83, No. 20, 1999, pp. 4120–4123 http://dx.doi.org/10.1103/PhysRevLett.83.4120

[7] Yang, B. – Emmez, E. – Kaden, W. E. – Yu, X. – Boscoboinik, J. A. – Sterrer, M. – Shaikhutdinov, S. – Freund C.,H.-J. : (2013) Hydroxylation of Metal-Supported Sheet-Like Silica Films, The Journal of Physical Chemistry C, Vol. 117, No. 16, 2012, pp. 8336–8344 http://dx.doi.org/10.1021/jp401935u

[8] Ringleb, Franziska – Sterrer, Martin – Freund, Hans-Joachim: (2013) Preparation of Pd–MgO model catalysts by deposition of Pd from aqueous precursor solutions onto Ag(0 0 1)-supported MgO(0 0 1) thin films, Applied Catalysis,Vol. 474, 2014, pp. 186-193 http://dx.doi.org/10.1016/j.apcata.2013.05.031

[9] Meyer, R. – Baumer, M. – Shaikhutdinov, Sh. K. – Freund, H.-J. : (2003) Two-dimensional growth of Pd on a thin FeO(1 1 1) film: a physical manifestation of strong metal–support interaction, Surface Science, Vol. 546, No. 2-3, 2003, pp. L813–L819 http://dx.doi.org/10.1016/j.susc.2003.09.025

[10] Giorgi, J.B. – Schroeder, T. – Baumer, M. – Freund, H.-J.: (2002) Study of CO adsorption on crystalline-silica-supported palladium particles, Surface Science, Vol. 498, No. 1-2, 2002, pp. L71–L77 http://dx.doi.org/10.1016/S0039-6028(01)01756-3

[11] K. Wolter, – H. Kuhlenbeck, – H.-J. Freund,: (2002) Hydrodynamic Voltammetry at the Liquid/Liquid Interface: The Rotating Diffusion Cell, The Journal of Physical Chemistry C, Vol. 106, No. 26, 2002, pp. 6723–6739 http://dx.doi.org/10.1021/jp025683e

[12] P. Nolte, – A. Stierle, – N. Kasper, – N.Y. Jin-Phillipp, – N. Jeutter, – H. Dosch,: (2011) Reversible Shape Changes of Pd Nanoparticles on MgO(100), Nano Letters, Vol. 11, No. 11, pp. 4697–4700 http://dx.doi.org/10.1021/nl2023564

[13] Nolte, P. – Stierle, A. – Kasper, N. – Jin-Phillipp, N. Y. – Reichert, H. – Rühm, A. – Okasinski, J. – Dosch, H. – Schöder, S.: (2008) Combinatorial high-energy x-ray microbeam study of the size-dependent oxidation of Pd nanoparticles on MgO(100), Physical Review B, Vol. 77, 2008, 115444 http://dx.doi.org/10.1103/PhysRevB.77.115444

[14] Jak, M. J. J. – Konstapel, C. – Van Kreuningen, A. – Verho-even, J. – Frenken, J. W. M.: (2000) Scanning tunnelling microscopy study of the growth of small palladium particles on TiO2(110), Surface Science, Vol. 457, No. 3, 2003, pp. 295-310 http://dx.doi.org/10.1016/S0039-6028(00)00431-3

[15] Pang, C. L. – Raza, H. – Haycock, S. A. – Thornton, G. : (2000) Growth of copper and palladium on α-Al_2O_3(0001), Surface Science, Vol. 460, No. 1-3, 2000, pp. L510-514. http://dx.doi.org/10.1016/S0039-6028(00)00594-X

[16] Stone, P. – Bennett, R. A. – Poulston, S. – Bowker, M. : (1999) Scanning tunnelling microscopy and Auger electron spectroscopy study of Pd on TiO2(110), Surface Science, Vol. 433-435, 1999, pp. 501-505 http://dx.doi.org/10.1016/S0039-6028(99)00485-9

[17] Xu, C. – Lai, X. – Zajac, G. W. – Goodman, D. W. : (1997) Scanning tunneling microscopy studies of the TiO2(110) surface: Structure and the nucleation growth of Pd, Physical Review B, Vol. 56, 1997, 13464 http://dx.doi.org/10.1103/PhysRevB.56.13464

[18] Henry, C. R. – Poppa, H.: (1988) Effect of substrate preparation on the structure and chemisorption properties of Pd/MgO model catalyst, Journal of Vacuum Science & Technology A, Vol. 6, No. 3, 1988, pp. 1113-1117 http://dx.doi.org/10.1116/1.575655

[19] Xu, C. – Oh, W. S. – Liu, G. – Kim, D. Y. – Goodman, D. W. : (1997) Characterization of metal clusters (Pd and Au) supported on various metal oxide surfaces (MgO and TiO₂), *Journal of Vacuum Science & Technology A*, Vol. 15, No. 3, 1997, pp. 1261-1268 http://dx.doi.org/10.1116/1.580604

[20] Henry, C. R. – Chapon, C. – Duriez, C. – Giorgio, S. : (1991) Growth and morphology of palladium particles epitaxially deposited on a MgO(100) surface, *Surface Science,* Vol. 253, No. 1-3, 1991, pp. 177-189 http://dx.doi.org/10.1016/0039-6028(91)90591-F

[21] Fornander, H. – Hultman, L. – Birch, J. – Sundgren, J.-E. : (1998) Initial growth of Pd on MgO(0 0 1), *Journal of Crystal Growth,* Vol. 186, No. 1-2, pp. 189-202 http://dx.doi.org/10.1016/S0022-0248(97)00443-0

[22] Goyhenex, C. – Meunier, M. – Henry, C. R.: (1996) Limitation of Auger electron spectroscopy in the determination of the metal-on-oxide growth mode: Pd on MgO(100), *Surface Science,* Vol. 350, No. 1-3, 1996, pp. 103-112. http://dx.doi.org/10.1016/0039-6028(95)01255-9

[23] Xu, Lijun – Campbell, Charles T. – Jónsson, Hannes – Henkelmana, Graeme: (2007) Kinetic Monte Carlo simulations of Pd deposition and island growth on MgO(1 0 0), *Surface Science* Vol. 601, No. 14, pp. 3133–3142 http://dx.doi.org/10.1016/j.susc.2007.05.027

[24] Venables, J. A. – Harding, J. H. : (2000) Nucleation and growth of supported metal clusters at defect sites on oxide and halide (0 0 1) surfaces, *Journal of Crystal Growth,* Vol. 211, No. 1-4, 2000, pp. 27- 33 http://dx.doi.org/10.1016/S0022-0248(99)00837-4

[25] Henry, C. R. – Meunier, M.: (1998) Power laws in the growth kinetics of metal clusters on oxide surfaces, *Vacuum,* Vol. 50, No. 1-2, pp. 157-163 http://dx.doi.org/10.1016/S0042-207X(98)00034-7

[26] Giordano, Livia – Di Valentin, Cristiana – Pacchioni, Gianfranco – Goniakowski, Jacek: (2005) Formation of Pd dimers at regular and defect sites of the MgO(1 0 0) surface: cluster model calculations, *Chemical Physics,* Vol. 309, No. 1, 2005, pp. 41–47 http://dx.doi.org/10.1016/j.chemphys.2004.02.022

[27] Sicolo, Sabrina – Pacchioni, Gianfranco: (2008) Charging and stabilization of Pd atoms and clusters on an electron-rich MgO surface, *Surface Science* Vol. 602, No. 16, pp. 2801–2807 http://dx.doi.org/10.1016/j.susc.2008.07.005

[28] Giordano, Livia – Pacchioni, Gianfranco: (2005) Pd nanoclusters at the MgO(1 0 0) surface, *Surface Science* Vol. 575, No. 1-2, pp. 197–209 http://dx.doi.org/10.1016/j.susc.2004.11.024

[29] Renaud, Gilles: (2005) Real-Time Monitoring of Growing Nanoparticles by in situ Small Angle Grazing Incidence X-Ray Scattering, *AIP Conference Proceedings,* Vol. 748. No. 63, 2005 http://dx.doi.org/10.1063/1.1896476

[30] Robinson, V. N. E. – Robins, J. I.: (1974) Nucleation kinetics of gold deposited onto UHV cleaved surfaces of NaCl and KBr, *Thin Solid Films,* Vol. 20, No. 1, pp. 155-175 http://dx.doi.org/10.1016/0040-6090(74)90043-1

[31] Kashchiev, D.: (1976) Kinetics of thin film coalescence due to crystallite surface migration, *Surface Science* Vol. 55, No. 2, pp. 477–493 http://dx.doi.org/10.1016/0039-6028(76)90253-3

[32] Zinsmeister, G.: (1966) A contribution to Frenkel's theory of condensation, *Vacuum,* Vol. 16, No. 10, pp. 529-535 http://dx.doi.org/10.1016/0042-207X(66)90349-6

[33] Volmer, M.: Kinetic der Phasenbildung. *T. Steinkopff Verlag,* Leipzig (1939)

[34] Halpern, V.: (1969) Cluster Growth and Saturation Island Densities in Thin-Film Growth, *Journal of Applied Physics,* Vol. 40, No. 11, 1969, pp. 4627-4636 http://dx.doi.org/10.1063/1.1657243

[35] Sigsbee, R.: (1971) Adatom Capture and Growth Rates of Nuclei, *Journal of Applied Physics,* Vol. 42, No. 10, 1971, pp. 3904-3915 http://dx.doi.org/10.1063/1.1659705

[36] Stowell, M. J.: (1972) Capture numbers in thin film nucleation theories, *Philosophical Magazine,* Vol. 26, No. 2, 1972, pp. 349-360 http://dx.doi.org/10.1080/14786437208227433

[37] Lewis, B.: (1970) Migration and capture processes in heterogeneous nucleation and growth: I. Theory, *Surface Science,* Vol. 21, No. 2, pp. 273–288 http://dx.doi.org/10.1016/0039-6028(70)90234-7

[38] Venables, J. A.: (1973) Rate equation approaches to thin film nucleation kinetics, *Philosophical Magazine,* Vol. 27, No. 3, 1973, pp. 697-738 http://dx.doi.org/10.1080/14786437308219242

[39] Lewis, B. – Rees, G. J.: (1974) Adatom migration, capture and decay among competing nuclei on a substrate, *Philosophical Magazine,* Vol. 29, No. 6, 1974, pp. 1253-1280 http://dx.doi.org/10.1080/14786437408226184

[40] Venables, J. A.: (1994) Atomic processes in crystal growth, *Surface Science,* Vol. 299-300, No. 2, 1994, pp. 798-817 http://dx.doi.org/10.1016/0039-6028(94)90698-X

[41] Nichols, F. A. – Mullins, W. W.: (1965) Morphological Changes of a Surface of Revolution due to Capillarity-Induced Surface Diffusion, *Journal of Applied Physics,* Vol. 36, No. 6, 1965, pp. 1826-1835 http://dx.doi.org/10.1063/1.1714360

[42] Menck, A.: Ph.D. thesis, Lausanne, 1998

[43] Højrup-Hansen, K. – Ferrero, S. – Henry, C. R.: (2004) Nucleation and growth kinetics of gold nanoparticles on MgO(1 0 0) studied by UHV-AFM, *Applied Surface Science,* Vol. 226, No. 1-3, pp. 167–172 http://dx.doi.org/10.1016/j.apsusc.2003.11.017

[44] Meunier, M.: Ph.D. thesis, Marseille, 1995

[45] C.R. Henry (1998) Surface studies of supported model catalysts, *Surface Science Reports,* Vol. 31, No. 7-8, pp. 231-325 http://dx.doi.org/10.1016/S0167-5729(98)00002-8

[46] Carrey, J. – Maurice, J.-L. – Petro, F. – Vaurès, A. : (2002) Growth of Au clusters on amorphous Al₂O₃: are small clusters more mobile than atoms?, *Surface Science,* Vol. 504, 2002, pp. 75–82 http://dx.doi.org/10.1016/S0039-6028(01)01796-4

[47] Carrey, J. – Maurice, J.-L.: (2002) Scaling laws near percolation during three-dimensional cluster growth: A Monte Carlo study, Physical Review B, Vol. 65, No. 20, 2002, 205401 http://dx.doi.org/10.1103/PhysRevB.65.205401

[48] Bartelt, M. C. – Evans, J. W.: (1994) Dendritic islands in metal-on-metal epitaxy I. Shape transitions and diffusion at island edges, Surface Science, Vol. 314, No. 1, 1994, pp. L829–L834 http://dx.doi.org/10.1016/S0039-6028(01)01796-4

[49] Harsdorff, M.: (1982) Heterogeneous nucleation and growth of thin films, Thin Solid Films, Vol. 90, No. 1, pp. 1-14 http://dx.doi.org/10.1016/0040-6090(82)90061-X

Pd diszperz katalizátor modell képződése a vékony MgO (100) rétegen

A szerzők a Fortran szofter felhasználásával egy szimulációs katalizátor modellt dolgoztak ki a diszpergált Pd palládium nanoszemcsék alkalmazásával vékony MgO magnézium-oxid rétegen. Ez a szimulációs modell a transzmissziós elektronmikroszkóppal (TEM) in-situ végzett csiraképződési és növekedési vizsgálati adatokon alapszik Az első kvantitatív vizsgálat a nucleation és a növekedést. A palládium nanorészecskék beépülését a vékony MgO rétegbe az 573-1073 K-fok hőmérséklet-tartományban tesztelték 1000 sec hőkezelési időtartam alatt. Azt tapasztalták, hogy a folyamat az alábbi három szakaszra osztható: a véletlenszerűen (random) csiraképződés; a növekedés; és végül az egyesülés. Az Arrhenius törvénynek megfelelően a létrejött klaszterek telítettségi sűrűsége csökken a szubsztrátum hőmérsékletének növekedésével – hasonlóan mint ahogyan ezt megfigyelték az Ag/MgO illetve Au/MgO AFM (atomic force Microscopy) tanulmányozásakor. Az egyesülési jelenség az úgynevezett sziget-migrációs folyamattal magyarázható; mely folyamat annál gyorsabb, minél magasabb a hőmérséklet.

Kulcsszavak: katalizátorok, kristályok, magnézium-oxid, csiraképződés, palládium

Performance of novel type three dimensionally deformed steel fibres for concrete

Péter KEREKES ▪ BSc (CE) student, BME Faculty of Civil Engineering ▪ wubxwub@gmail.com
Adorján BOROSNYÓI ▪ Assoc. Prof., BME, Dept. of Construction Materials and Engineering Geology
▪ borosnyoi.adorjan@epito.bme.hu

Péter Kerekes
Civil engineer (BSc) student at Budapest University of Technology and Economics (BME), Faculty of Civil Engineering. Main fields of interest: development and performance of steel fibres for concrete.

Adorján Borosnyói
Civil engineer (MSc), PhD, Associate Professor at BME Dept. of Construction Materials and Engineering Geology. Main fields of interest: cracking and deflection of reinforced concrete, application of non-metallic (FRP) reinforcements for concrete structures, bond in concrete, nondestructive testing of concrete, supplementary cementing materials for high performance concretes, concrete technology. Member of the fib Task Group 4.1 „Serviceability Models", corresponding member of RILEM Technical Committee 249-ISC „Non destructive in situ strength assessment of concrete" and Chairman of the SZTE Concrete Division.

Abstract

Preliminary results of a two years long research and development project is introduced in this paper. One novel type of 2D deformed steel fibre (with the product name of PetiX) and four different types of 3D deformed steel fibres (PetiX V45; PetiX V90; PetiX S45; PetiX S60) were designed, manufactured and tested under laboratory conditions. The laboratory tests showed promising results. Superior performance of certain types of 3D deformed steel fibres was observed. Considerable improvement of the bond performance of steel fibres was realized in concrete and increased flexural toughness of SFRC prismatic specimens tested in flexure was demonstrated.
Keywords: concrete, steel fibre, 3D geometry, bond, flexural strength, toughness

1. Introduction

The use of Steel Fibre Reinforced Concrete (SFRC) has been greatly increased in the past few decades in civil engineering [1-6]. SFRC is mostly used for industrial floors but it can provide a good solution for shear walls and prefabricated elements as well. Advantages of SFRC are the less labour work, the reduction of brittleness and the increase of toughness and shear resistance of concrete.

Most important performance parameter of steel fibres made of cold drawn steel wires is the surface geometry, therefore, several different types of steel fibres have been developed during the last decades. Hooked-end, undulated, crimped, twisted, end-anchoring, flat-end and several combined geometries are commercially available for concrete construction. Certain types of steel fibres show considerably improved bond and anchorage in concrete compared to plain fibres, however, the different types of steel fibres are usually deformed only in two dimensions. Physical and chemical surface treatments may also be applied to enhance bond performance. Diameters and lengths of steel fibres vary from 0.1 to 1 mm and 10 to 60 mm, respectively. There is, however, a gap in experience connected to the performance of steel fibres deformed in 3D.

Three types of bond are available in SFRC: 1) elastic force transfer; that is the adhesion of the fibres to the concrete, 2) frictional force transfer; that is provided by friction between the fibres and the concrete giving resistance against pull-out and 3) mechanical force transfer; that is provided by mechanical interlock of the fibres that are intentionally deformed along their lengths. Development of steel fibres which are deformed in 3D may provide better bond performance by enhancing frictional force transfer component and mechanical force transfer component of the bond action.

2. Steel fibres with novel 3D geometry

In the present research and development project (started in October, 2013), four different types of 3D deformed steel fibres and one type of 2D deformed steel fibre were designed, manufactured and studied under laboratory conditions [7]. The 2 dimensionally deformed fibre was the basic fibre that was used for the further 3 dimensional deformation process during manufacturing. A special device was constructed to produce the special fibres. The device was designed directly for the present research and development project and the prototype fibres were manufactured manually with the use of the device.

The basic 2 dimensionally deformed steel fibre received the product name of PetiX (*Fig. 1*). The basic 2 dimensionally deformed steel fibre has a waved shape with three waves. The magnitude of the waves is intentionally selected to be larger than that of the commercially available for the waved geometry steel fibres. The larger waves were chosen due to an expected better performance of the fibres when they are deformed in 3 dimensions. With smaller waves of the basic fibre the effect of the 3 dimensional deformations was expected to be less remarkable.

The first 3D fibre is the PetiX V45 type steel fibre (*Fig. 2*). This is the shape of 3D geometry that was developed first during the research and development project, and this is the type of fibre that was actually the initiation that started the research, back in October 2013. The identifying feature of the 3 dimensionally deformed PetiX V45 type steel fibre is the middle wave that is bent out from the basic fibre's 2D plane with 45 degrees.

The second type of the 3D fibres is the PetiX V90 type steel fibre (*Fig. 3*). This extremely deformed type of fibre was created since it was unknown how the extent of the deformation could influence the behaviour of the fibres in concrete. The concept is the same for the PetiX V90 type steel fibre as it was for the PetiX V45 type steel fibre, but the deformation rate was selected to be 90 degrees, rather than 45 degrees.
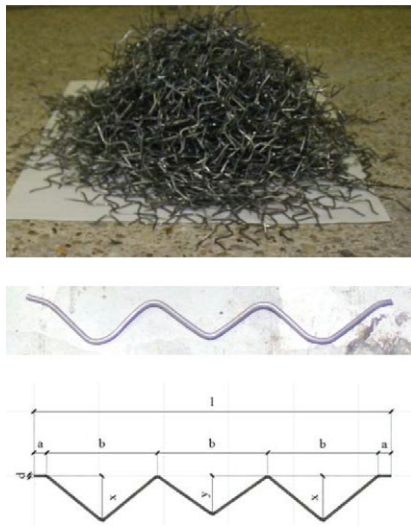
Fig. 1. 2D deformed basic steel fibre, PetiX
1. ábra Két dimenzióban megmunkált PetiX alapszál
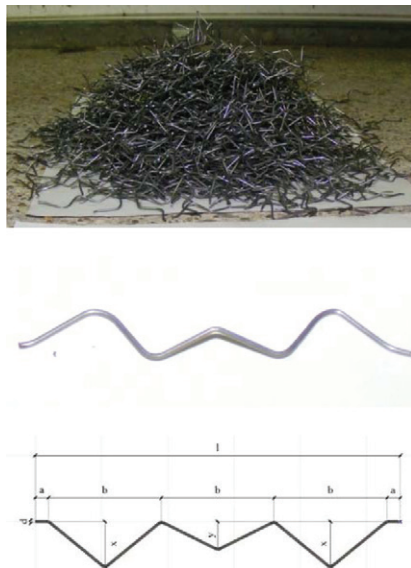
Fig. 2. 3D deformed steel fibre, PetiX V45
2. ábra Három dimenzióban megmunkált PetiX V45 acélszál
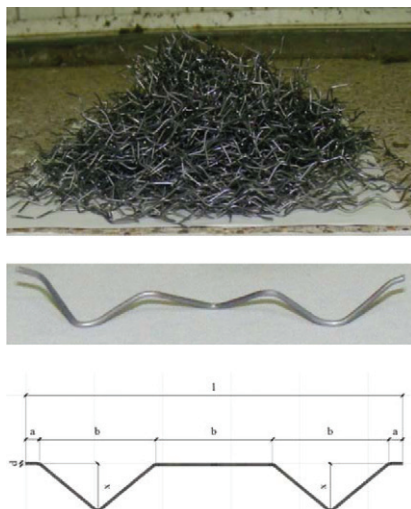
Fig. 3. 3D deformed steel fibre, PetiX V90
3. ábra Három dimenzióban megmunkált PetiX V90 acélszál
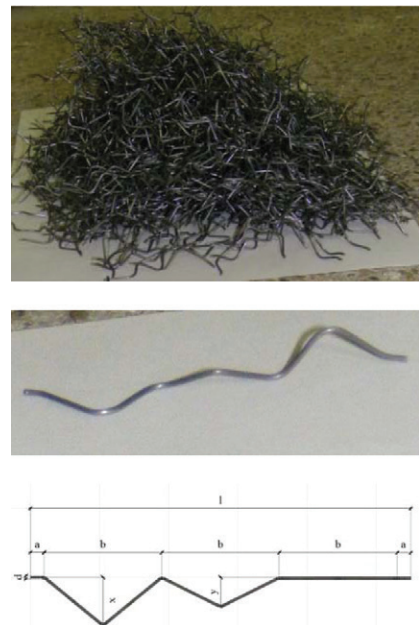
Fig. 4. 3D deformed, twisted steel fibre, PetiX S45
4. ábra Három dimenzióban megmunkált PetiX S45 acélszál
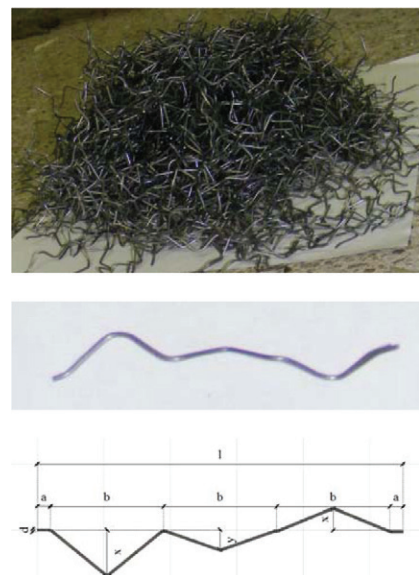
Fig. 5. 3D deformed, twisted steel fibre, PetiX S60
5. ábra Három dimenzióban megmunkált PetiX S60 acélszál

The third type of the 3D fibres is the PetiX S45 type steel fibre (*Fig. 4*). It provides a spiral-like appearance since the shape of geometry of the 2D basic PetiX fibre made it possible to create a spiral-like, twisted steel fibre as well during the 3D deformation process. Its attribution is that every wave is bent 45 degrees further out from plane than the previous wave.

The fourth type of the 3D fibres is the PetiX S60 type steel fibre (*Fig. 5*). The shape of geometry is very similar to that of the PetiX S45 type steel fibre, but at this type the extent of the deformation is 60 degrees, rather than 45 degrees.

Cold drawn steel wire raw materials were used for the present experimental program with a nominal tensile strength of 1400 N/mm², provided by D&D Drótáru Zrt., Hungary.

3. Experiments

Two different experimental test series were conducted with the novel type 3D geometry steel fibres. A series of three-point bending tests were carried out on prismatic SFRC specimens and a series of hinged beam pull-out tests were carried out on special design prismatic mortar specimens with cast-in hinges.

For the three-point bending tests 70×70×250 mm prismatic SFRC specimens with 30 kg/m³ steel fibre dosage were used. Twelve individual specimens were prepared for each type of the novel type 3D geometry steel fibres to get reliable results. Specimens were tested at a span of 200 mm under one concentrated load at mid-span. Specimens were monotonically loaded with static loading up to complete flexural failure – that resulted the separation of the prismatic SFRC specimens to two blocks. Corresponding load and deflection values were continuously recorded and the load-deflection responses were prepared. Load-deflection responses were used for the comparative performance analysis.

For the hinged beam pull-out tests 40×40×160 mm mortar prisms were prepared. During specimen preparation, three individual fibres were placed at the middle sections of the prisms running through a polystyrene plate of 7 mm thickness. A steel hinge was placed over the middle section in each specimen as a load distributing element. Specimens were tested at a span of 100 mm under one concentrated load at mid-span, located on the steel hinge. Specimens were monotonically loaded with static loading up to complete bond failure – that resulted either the pull-out of the fibres from the to two blocks or the splitting of the cover over the steel fibres. Corresponding load and deflection values were continuously recorded and the load-deflection responses were prepared. The bond performance can be studied by the load-deflection responses since fibres can be considered to be loaded in pure tension due to the special loading conditions provided by the hinged beam pull-out tests.

4. Results

Present paper summarizes the experimental results of exclusively the 70×70×250 mm prismatic SFRC specimens tested in three-point bending. Load-deflection curves are indicated in *Fig. 6*. The curves indicated represent the average curves of the individual 12 load-deflection responses recorded for each type of steel fibres. As a reference, hooked-end steel fibres (product of D&D, Hungary) were also tested. For the better visualization of the performance differences, *Fig 6.b* provides these averaged results with a vertical axis of relative load that gives the load values of the specimens prepared with the novel type steel fibres as ratios of load recorded for the reference specimens prepared with hooked-end fibres at the same deflection level. It can be clearly realized that the novel type steel fibres provide superior performance with increased flexural toughness. Due to the large waves of the 2 dimensionally deformed basic PetiX steel fibre, higher flexural resistance is available than that of the reference SFRC specimens prepared with hooked-end steel fibres. At 7.5 mm

mid-span deflection the difference exceeds 30%. Steel fibres that are deformed in 3D provide better performance than that of the 2 dimensionally deformed basic PetiX steel fibre. Certain fibre geometries (e.g. PetiX V45 and PetiX S60) can give 1.4-times higher flexural resistance than the reference SFRC specimens prepared with hooked-end steel fibres. It can be also realized that the performance of PetiX V90 is inferior with decreased flexural toughness. The behaviour is attributed to the middle wave of the fibre that is bent out from the basic fibre's 2D plane with 90 degrees. Such large deviation in geometry without gradual change results a more pronounced tendency of forming tangles of fibres during mixing and may result an uneven distribution of fibres within the concrete matrix, additionally to the fact that the fibres themselves are more sensitive to rupturing within concrete cracks due to the large local deformations by their extreme shape.
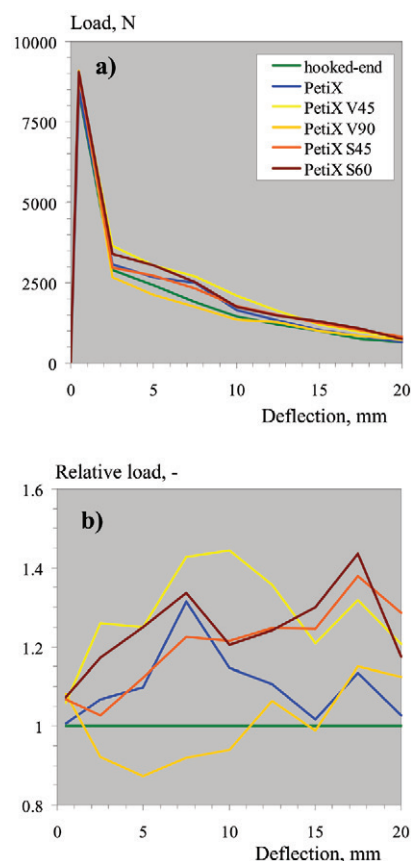
Fig. 6. Load-deflection responses of SFRC specimens
6. ábra SFRC hasábok terhelőerő-lehajlás diagramjai

If one defines flexural toughness as the area under the load-deflection response then the performance of the fibres can be compared by this integral type of material parameter as a general indicator, being independent of the values of deflection. Relative flexural toughness values are indicated in *Fig. 7* (taking 100% for the flexural toughness of reference SFRC specimens prepared with hooked-end steel fibres). The superior performance of both 2D and 3D PetiX steel fibres is clearly visible together with the inferior performance of PetiX V90. Highest flexural toughness was reached by PetiX V45 and PetiX S60 type 3D deformed steel fibres.

Relative toughness index, -
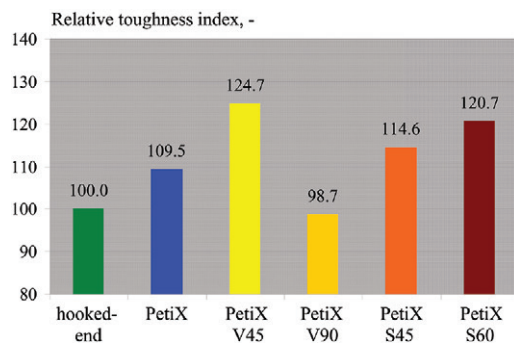
Fig. 7.   *Relative toughness indices of SFRC specimens*
7. ábra   *SFRC hasábok relatív szívóssági indexei*

Another suitable indicator for the enhanced bond and corresponding increased toughness of the 3D deformed steel fibres can be the ratio of the number of the ruptured and pulled-out fibres within the cross sections of cracks resulting flexural failure of the prismatic specimens. After the failure of the specimens, the resulting two blocks of the prisms were separated from each other and the failure mode of each individual steel fibre in the crack sections was carefully observed and recorded. *Fig. 8* summarizes the results. The bar chart indicates the ratio of the number of the ruptured fibres to the total number of fibres within the cross sections of cracks (summarized for all the 12 individual prismatic specimens), given in percents. For the reference SFRC specimens prepared with hooked-end steel fibres no fibre rupture was observed. All fibres were pulled-out from the concrete matrix at the cross sections of cracks. Best performance was observed for PetiX V45 and PetiX S45 type 3D deformed steel fibres. It should be highlighted here as well that the results for PetiX V90 type 3D deformed steel fibres is misleading in this representation. One should observe that the smallest number of fibres was found in the failure cross sections for V90 type 3D deformed steel fibres due to the uneven distribution of fibres and the extreme deformation of this type of fibre geometry resulted the high ratio of ruptured fibres observed and the reason is not the enhanced bond capacity of the fibres.

Ratio of ruptured fibres, %

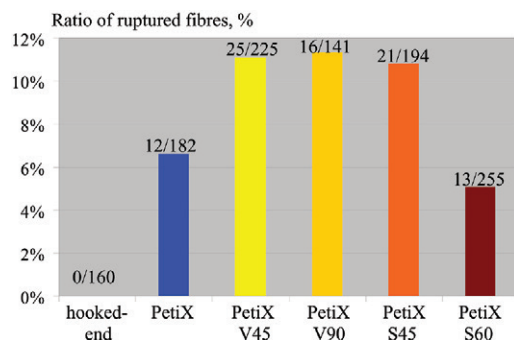*Fig. 8.*   *Ratio of ruptured fibres in SFRC specimens*
8. ábra   *Elszakadt acélszálak aránya SFRC hasábokban*

5. Conclusions

The present research and development project designed, manufactured and tested one novel type of 2D deformed steel fibre (receiving the product name of PetiX) and four different types of 3D deformed steel fibres (PetiX V45; PetiX V90; PetiX S45; PetiX S60) under laboratory conditions. It was demonstrated that certain types of 3D deformed steel fibres can hold considerably improved the bond performance in concrete that results increased flexural toughness of SFRC prismatic specimens tested in flexure.

6. Acknowledgements

References

[1] Balaguru, P. N. – Shah, S.P. (1992): Fiber-reinforced cement composites. *McGraw-Hill*, New York, 1992, 530 p.

[2] Bentur, A. – Mindess, S. (2007): Fibre-reinforced cementitious composites. 2nd ed. *Taylor & Francis*, New York, 2007, 660 p.

[3] Brandt, A.M. (2008): Fibre-Reinforced Cement-based (FRC) composites after over 40 years of development in building and civil engineering. *Composite Structures*, Vol. 86, No. 1-3, pp. 3–9. http://dx.doi.org/10.1016/j.compstruct.2008.03.006

[4] Banthia, N. – Bindiganavile, V. – Jones, J. – Novak, J. (2012): Fibre-reinforced concrete in precast concrete applications: research leads to innovative products. *PCI Journal*, Vol. 57, No. 3, pp. 33–46.

[5] Walraven, J.(2009): High performance fiber reinforced concrete: progress in knowledge and design codes. *Materials and Structures*, Vol. 42, pp.1247–1260. http://dx.doi.org/10.1617/s11527-009-9538-3

[6] di Prisco, M. – Plizzari, G. – Vandewalle, L. (2009): Fibre reinforced concrete: new design perspectives. *Materials and Structures*, Vol. 42, No. 9, pp. 1261–1281. http://dx.doi.org/10.1617/s11527-009-9529-4

[7] Kerekes, P. (2014): 2 and 3 dimensional steel fibers with novel geometry: design, development and comparison of effectiveness in concrete (supervisor: Borosnyói, A.), *Budapest University of Technology and Economics* (BME), Faculty of Civil Engineering, Thesis submitted for the Students' Scientific Workshop 2014, 50 p. (in Hungarian)

Új típusú, három dimenzióban megmunkált acélszálak tulajdonságai
Egy két éves kutatás-fejlesztési projekt első eredményeit mutatja be a cikk. A kutatás során egy fajta, 2 dimenzióban megmunkált acélszál (PetiX), és négy fajta, 3 dimenzióban megmunkált acélszál (PetiX V45; PetiX V90; PetiX S45; PetiX S60) lett kifejlesztve. A laboratóriumi vizsgálatok eredményei kedvezőek. Bizonyításra került, hogy egyes 3 dimenziós geometriai kialakításokkal jelentős mértékben növelhető az acélszálak tapadása betonban, és ezzel fokozható a szélerősítésű betonok hajlítási szívóssága, amelyet a laboratóriumi vizsgálatok eredményei igazolnak.
Kulcsszavak: beton, acélszál, 3 dimenziós geometria, tapadás, hajlítószilárdság, szívósság

Utilization of repair mortar for the loss compensation of Hungarian porous limestone

Balázs SZEMEREY-KISS ▪ BME, Faculty of Civil Engineering, Department of Construction Materials and Engineering Geology ▪ szemerey@gmail.com

Ákos TÖRÖK ▪ BME, Faculty of Civil Engineering, Department of Construction Materials and Engineering Geology ▪ torokakos@mail.bme.hu

Balázs Szemerey-Kiss
(1978) stone sculptor restorer (MA, 2002), Preservation of Monuments Specialist Engineer (2007), PhD (2013). Graduated at the Academy of Fine Arts, Department of Restoration and Conservation, Budapest (2002). Postgraduate Degree in the Section of Preservation of Monuments (2004-2007) at the Budapest University of Technology and Economics, Faculty of Architecture. PhD at the Budapest University of Technology and Economics, Department of Construction Materials and Engineering Geology (2013). Main fields of interest: protection of heritage sculptures, material testing, loss compensation of porous stones.

Ákos Török
(1963) geologist (MSc, 1986), MSc in Environmental Engineering and Science (1993), PhD (1995), DSc (2013), full professor at the Budapest University of Technology, Faculty of Civil Engineering. Member of the International Association of Engineering Geologists IAEG, (President of Hungarian National Group), International Society of Rock Mechanics ISRM, (President of Hungarian National Group), Hungarian Geological Society (President of the Engineering Geology and Environmental Geology Division). Main fields of interest: engineering geology, applied geology, sediment geology, carbonate sedimentology, material testing and protection of heritage buildings.

Abstract

Different ready-made, commercially available (in Hungary) stone repair mortars and laboratory mixed, newly designed mortars were tested under different conditions in the laboratory. The mortars had different aggregate and binder content. The aim of the research was to understand the influence of the different binders and various amounts of limestone aggregate on the properties of mortar. During the laboratory tests more than 550 specimens were analyzed according to the EN standards. Pure repair mortars have higher strength and lower capillary activity than the Hungarian porous limestones. Added aggregate can increase the compatibility of the commercially available mortars, but at some mortars it may result a drastic decrease in strength. Newly designed mortars have similar mechanical and hydrotechnical properties to the tested porous limestones.
Keywords: repair mortar, limestone, binder/aggregate ratio, compressive strength, compatibility

1. Introduction

Repair mortars or artificial stones are often used for repair of stone monuments and artistic stone elements of facades, sculptures or statues. There is not a uniform terminology for the loss compensation of stones: the expressions of repair mortars or artificial stones are used by different authors [1-4].

Previous research in this field focused on loss compensation methods for stones [1,2]. Additional studies were made on the amount of filler added to cementitious materials and the performance of these materials was tested [5,6]. Mortars with specially selected fillers were also tested. Both natural and artificial inorganic materials were added to mortars to improve the physico-chemical and mechanical properties; workability or water retention was also analyzed [7-9]. In recent years, mechanical properties and fabric analyses were also made [3,10-13]. Chemical composition of the mortars were also analyzed [14-16]. Compatibility of the limestone and mortar was studied considering strength and durability characteristics such as mechanical resistance, water transfer properties, and physico-chemical properties [17-20].

Fig. 1.   Loss compensation with incompatible repair mortar.
1. ábra   Kőkiegészítés nem kompatibilis habarccsal.

Case studies have shown, that many of the commercially available (ready-mix) repair mortars can not be adequately used under certain conditions and are not compatible with porous limestone [17-18] (*Fig. 1*). Only limited data are available from the product properties in catalogues, safety data sheets, product specifications. There is not enough information about the porosity, fluid transport properties, pore-size distribution, long-term behaviour of the mortars and compatibility with porous limestones. Therefore, further information is needed to find the best performance and compatible mortar for the given stone. Repair mortars have been tested according to the European (EN) and American (ASTM) standards and performance in terms of strength, porosity, hydro-technical properties were measured [12-13].

2. Materials and methods

Commercially available repair mortars are commonly used for the restoration of stone structures made of Hungarian oolitic limestone. Practitioners use these ready-mix mortars since it is easy to work with them that allow a relatively fast repair. Furthermore, there are individual mortar recipes in the restoration practice. These two categories of mortars (pre-mixed and site-made) were tested under laboratory conditions. Their properties were compared with that of Hungarian porous limestone. Two lithologies were analyzed. The limestone was collected from Sóskút quarry, which is located app. 30 km from the capital of Hungary. The two tested lithologies are:

DMF: limestone with fine-grained micro-fabric (*Fig. 2a*),
DMD: limestone with coarse-grained micro-fabric (*Fig. 2b*).

Two groups of mortars were also tested. The first group is composed of different types of mortars that are commercially available repair mortars (M). The compounds of the mortars were made in Germany and test specimens from ready-mix mortars

were prepared under laboratory conditions. 30 to 50 m% of limestone sand aggregate was added to the tested mortars to make the repair mortar more compatible with the coarse limestone. This mixing of mortar with limestone sand is a common method in the restoration practice in Hungary.

The abbreviations of the tested mortars are as follows:

M: pure repair mortars (pre-mixed mortar + water),

M30: pure mortar with 30 m% added limestone sand aggregate and

M50: pure mortar with 50 m% added limestone sand aggregate.

Second group of tested mortars contained newly mixed repair mortars with two different compositions. Two types of cementitious binders were added to the mortars:

PLM: mortar with Portland cement and hydrated lime binder,

TLM: mortar with trass cement and hydrated lime binder.

The above mentioned limestone chippings (Sóskút quarry) were used for the aggregate sand. The maximum particles size of the aggregate was 2 mm in diameter. Fabric analysis of the tested materials was performed according to EN 12407:2000 European Standard by the analysis of thin-sections.
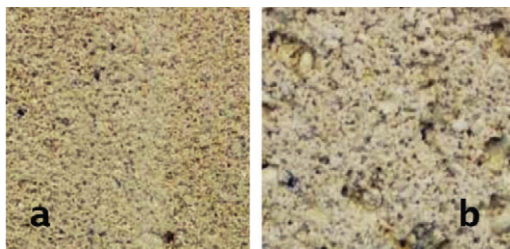
Fig. 2. Hugarian (Sóskút), Miocene, porous limestone: (a) fine-grained, (b) coarse-grained fabric.

2. ábra Sóskúti miocén korú durva mészkő: (a) finomszemű, (b) durvaszemű változata.

The sample preparation was made under laboratory conditions (temperature 20±2°C, relative humidity of 50–55%). The initial curing environment was the same in all cases. More than 550 mortar specimens (30×30×30mm in size) were prepared for uniaxial compressive test (EN 1015-11:2000). For the microscopic analysis thin-sections were made (thickness of 30 μm). Prismatic samples of 40×40×80 mm in size were used for the capillary water uptake measurements, following the EN 1925:2000 standard. Cylindrical specimens of 10 mm in diameter were made for the pore size distribution analyses. The measurements were made with a Carlo Erba 2000 (GFZ Potsdam) porosimeter and the data evaluation was made by a Pascal software (version of 1.03). Samples were dried in oven to constant mass at 105°C.
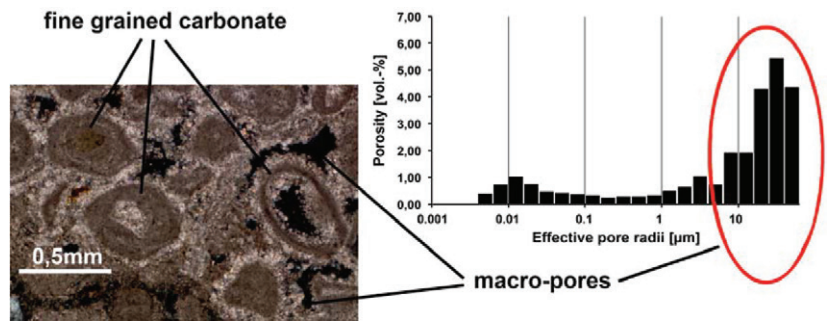
Fig. 3. Thin-section of the coarse-grained limestone (DMD) with the histogram of the pore size distribution of the limestone.

3. ábra Durvaszemű ooidos durva mészkő vékonycsiszolata és póruseloszlásának hisztogramja.
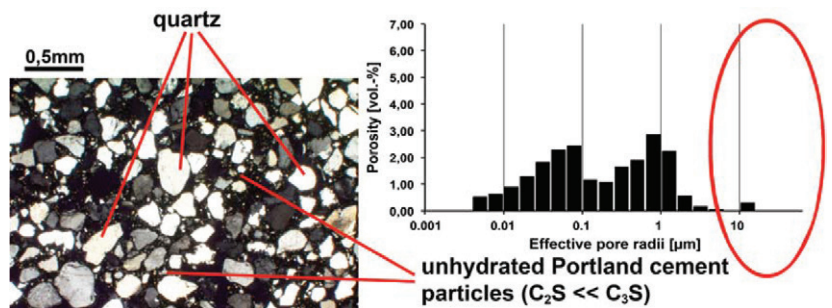
Fig. 4. Thin-section of the pure, commercial available repair mortar (M) with the histogram of the pore size distribution.

4. ábra Hazai kereskedelmi forgalomban kapható kőkiegészítő habarcs vékonycsiszolata és póruseloszlásának hisztogramja.
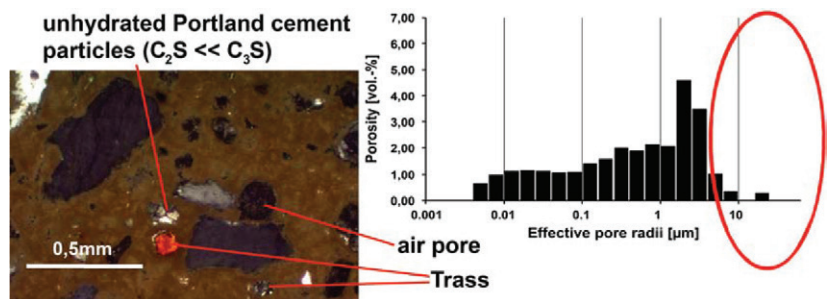
Fig. 5. Thin-section of the commercial available repair mortar (TLM) with the histogram of the pore size distribution.

5. ábra Kőkiegészítő habarcsban megjelenő trasz cement és légpórusok a vékonycsiszolatban, valamint a traszcement tartalmű habarcsok póruseloszlásának hisztogramja.
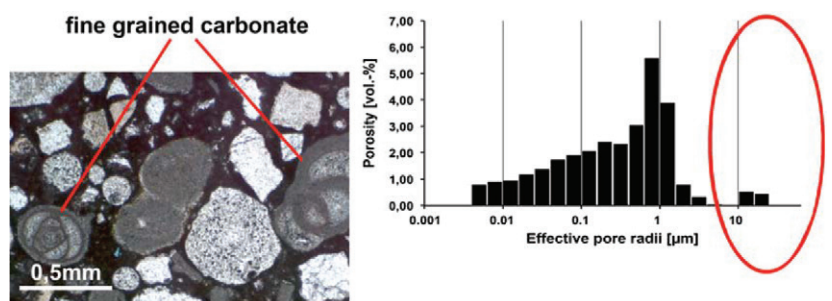
Fig. 6. Thin section of the commercial available repair mortar with 50m% added limestone sand aggregate (M50) with the histogram of the pore size distribution.

6. ábra Hazai kereskedelmi forgalomban kapható kőkiegészítő habarcsba kevert mészkő zúzalék (50m%) vékonycsiszolata és póruseloszlásának hisztogramja.

3. Results

3.1 Fabric

Limestone: The micro-fabric is characterized by the presence of ooids, and the microfacies of the stone is an ooid-grainstone to packstone. Large and visible macro pores of different size were visualized in both selected limestones (DMD and DMF). The porosity is characterized by the presence of intra- and inter-granular pores. According to the pore size distribution, the main pores were detected in the range of macro-pore size (10-100 μm) (*Fig. 3*).

Mortars (M): The binder is mostly calcitic, and the aggregate is mostly given by small rounded quartz grains of 10–500 μm. The hydraulic binder content of the samples (white portland cement) is clearly demonstrated by the unhydrated cement particles. Hydrated alite (C_3S - mostly), and small amounts of belite (C_2S) was also observed, furthermore a mixture of slaked lime was present in all of the four commercially available repair mortars (*Figs. 4* to *6*).

Mortars (M, PLM, TLM): Only very small visible pores were detected under the microscope. When 30 or 50 m% of limestone sand is added to the repair mortars, the proportion of the binder-to-aggregate ratio is shifted towards the grain dominance.
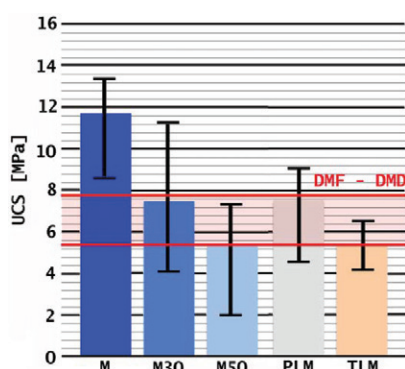

Fig. 7. *Average value with the standard deviation of the compressive strength of the tested mortars. All the values measured for the limestones are shown in the zone indicated in red colour.*

7. ábra *Habarcsok átlagos egyirányú nyomószilárdsága és szórása. A piros sávban vltak mérhetők a kétféle mészkövön a nyomószilárdsági értékek.*

Abbre-viation	UCS [MPa]					Water absorp-tion [%]	av. real density (g/cm³)
	day 3	day 7	day 14	day 28	day 90		
M	6.89	8.86	9.76	10.39	11.66	9.1	2.72
M30	4.28	5.54	6.42	7.21	7.54	11.7	2.67
M50	2.41	4.06	4.9	5.48	5.31	13.4	2.61
PLM	3.64	5.88	6.94	7.43	6.32	5,56	2.7
TLM	3.28	4.35	5.56	5.08	5.02	13.4	2.66
DMF	7.60 (dev 2.5)					20.5	2.69
DMD	5.56 (dev 2.2)					14.6	2.73

Table 1. *Uniaxial compressive strength (UCS), water absorption and density of the tested materials (for abbreviations see the text).*

1. táblázat *A vizsgált anyagok egyirányú nyomószilárdága, vízfelvétele és anyagsűrűsége (anyagok rövidítése a szövegben).*

3.2 Strength

Pure repair mortars (without limestone sand aggregate) have more than double of the strength than that of the tested porous limestones. Added limestone sand aggregate can reduce the strength of the mortars and it becomes closer to the strength of limestone (*Fig. 7* and *Table 1*).

The tests have demonstrated that newly designed repair mortars 28 days after curing (mostly TLM) have similar strength to that of porous limestone, but on a longer-term the strength of mortar specimens has been gradually decreased.

3.3 Water absorption

The capillary water uptake of the tested limestones is much faster than that of the tested repair mortars (*Fig. 8*). The slow water uptake of the pure repair mortars are proportionally increased, when limestone aggregate was added. The biggest increase in capillary water uptake was measured at mortars made with trass cement binder. Smaller increase was detected in water uptake at commercial available mortars with limestone aggregate (M30, M50).
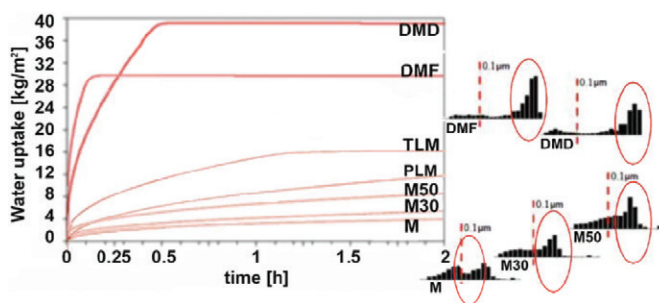
Fig. 8. *Capillary water uptake in the tested materials with the pore size distribution (DMD-coarse limestone, DMF- fine limestone, M, PLM, TLM tested mortars).*

8. ábra *Kapilláris vízfelvétel a vizsgált anyagokban a pórusméret-eloszlással (DMD-durvaszemű durva mészkő, DMF- finomszemű durva mészkő, M, PLM, TLM habarcsok).*

4. Conclusions

A close relationship between the pore structure, mechanical properties and water absorption of repair mortars were found. Previous experience has shown that increasing the aggregate content decreased the strength of the mortars and at the same time the porosity, water absorption and capillary suction are slightly increased [19, 21]. The lower water absorption of the repair mortars compared to natural stones is related to the very different pore size distribution. The oolitic limestone has exceptionally interconnected pore system with a wide range of pore radii, and high peaks in the pore size distribution histograms at macro-pores with diameter of around 10-100 μm. These macro-pores are missing from the pure mortars and from the mortars to which limestone aggregate is added. Among the tested repair mortars, only the mortars with trass cement binder have higher compatibility with the oolitic limestone, but the higher amount of aggregate decreased the strength and the workability of the mortar. It is important to highlight that the use of trass cement increased the capillary activity of the mortar and at the same time decreased the strength from the 28th day. Repair mortars with higher strength

and different porosity than that of the limestone can cause damage (cracking and spalling in the original stone surface). Usually weak limestones have lower modulus of elasticity than mortars made by Portland cement.

To conclude, the test results have shown that the use of significant amount of porous limestone sand as aggregate for pre-mixed repair mortars does not guarantee the compatibility of the repair mortar with the porous limestone, however, it has an evidential positive effect in compatibility. Without long term laboratory experiments, newly designed repair mortars might have serious compatibility problems with limestone.

5. Acknowledgments

References

[1] Griswold, J. – Uricheck, S.: (1998) Loss compensation methods for stone. Journal of the American Institute of Conservation 37:89–110

[2] Kriston L. (2000) A kő és vakolatrestaurálás alapismeretei. MKE, Budapest, 113–119 pp

[3] Pecchioni, E. – Malesani, P. – Bellucci, B. – Fratini, F: (2005) Artificial stones utilised in Florence historical palaces between the XIX and XX centuries Journal of Cultural Heritage 6:227–233
http://dx.doi.org/10.1016/j.culher.2005.06.001

[4] Isebaert, A. – Van Parys, L. – Cnudde, V: (2014) Composition and compatibility requirements of mineral repair mortars for stone – A review. Construction and Building Materials 59:39–50
http://dx.doi.org/10.1016/j.conbuildmat.2014.02.020

[5] Benachour, Y. – Davy, C. A. – Skoczylas, F. – Houari, H: (2008) Effect of a high calcite filler addition upon microstructural, mechanical, shrinkage and transport properties of a mortar. Cement and Concrete Research 38:727–736
http://dx.doi.org/10.1016/j.cemconres.2008.02.007

[6] Gosselin, C. – Verges-Belmin, V. – Royer, A. – Martinet, G.: (2009) Natural cement and monumental restoration. Materials and Structures 42:749–763
http://dx.doi.org/10.1617/s11527-008-9421-7

[7] Heikal, M. – El-Didamony, MH. – Morsy, MS: (2000) Limestone-filled pozzolanic cement. Cement and Concrete Research 30:1827–1834.
http://dx.doi.org/10.1016/S0008-8846(00)00402-6

[8] Bülent. Y. – Asim, O.: (2007) Studies on cement and mortar containing low-calcium fly ash, limestone, and dolomitic limestone. Cement & Concrete Composites 30:194–201
http://dx.doi.org/10.1016/j.cemconcomp.2007.07.002

[9] Ghrici, M. – Kenai, S. – Said-Mansour, M.: (2007) Mechanical properties and durability of mortar and concrete containing natural pozzolana and limestone blended cements. Cement & Concrete Composites 29:542–549
http://dx.doi.org/10.1016/j.cemconcomp.2007.04.009

[10] Barsottelli, M. – Cellai, G. F. – Fratini, F. – Manganelli, F.: (2001) The Hygrometric behaviour of some artificial stone materials used as elements of masonry walls. Materials and Structures 34:211-216
http://dx.doi.org/10.1007/BF02480590

[11] Sinan, C.: (2003) Aggregate/mortar interface: influence of silica fume at the micro- and macro-level. Cement & Concrete Composites 25:557–564
http://dx.doi.org/10.1016/S0958-9465(02)00095-1

[12] Pavia, S. – Fitzgerald, B. – Treacy, E.: (2006) An assessment of lime mortars for masonry repair. Concrete Research in Ireland Colloquium, University College Dublin, 101–108.

[13] Pavia, S. – Toomey, B.: (2008) Influence of the aggregate quality on the physical properties of natural feebly-hydraulic lime mortars. Materials and Structures 41: 559–569 http://dx.doi.org/10.1617/s11527-007-9267-4

[14] Bultrini, G. – Fragala, I. – Ingo, GM. – Lanza, G.: (2006) Minero-petrographic, thermal and microchemical investigation of historical mortars used in Catania (Sicily) during the XVII century A.D. Applied Physics. 83:529–536
http://dx.doi.org/10.1007/s00339-006-3551-y

[15] Tunçoku, SS. – Caner-Saltık, EN.: (2006) Opal-A rich additives used in ancient lime mortars. Cement and Concrete Research 36:1886–1893
http://dx.doi.org/10.1016/j.cemconres.2006.06.012

[16] Budak, M. – Maravelaki-Kalaitzaki, P. – Kallithrakas-Kontos, N.: (2008) Chemical characterization of Cretan clays for the design of restoration mortars. Microchim Acta 162:325–331
http://dx.doi.org/10.1007/s00604-007-0927-4

[17] Szemerey-Kiss, B. – Török, Á.: (2011) Time-dependent changes in the strength of repair mortar used in loss compensation of stone. Environmental Earth Sciences, 63:1613-1621
http://dx.doi.org/10.1007/s12665-011-0917-z

[18] Szemerey-Kiss, B. – Török, Á.: (2012) Porosity and compatibility of repair mortars and Hungarian porous limestones. Central European Geology, 52:123-133.
http://dx.doi.org/10.1556/CEuGeol.55.2012.2.1

[19] Szemerey-Kiss, B.: (2012) The application of adhesion strength test in the assesment of compatibility of repair mortars and porous limestones. Conference of Junior Researchers in Civil Engineering, 2012.06.19-2012.06.20. Budapest, BME, ISBN 978-963-313-061-2

[20] Szemerey-Kiss, B. – Török, Á. – Siegesmund, S.: (2013) The influence of binder/aggregate ratio on the properties and strength of repair mortars. Environmental Earth Sciences, 69:1439-1449
http://dx.doi.org/10.1007/s12665-013-2413-0

[21] Lanas, J. – Sirera, R. – Alvarez, JI.: (2006) Study of the mechanical behavior of masonry repair lime-based mortars cured and exposed under different conditions. Cement and Concrete Research 36:961–970
http://dx.doi.org/10.1016/j.cemconres.2005.12.003

Magyarországi porózus mészkövekhez alkalmazható kőkiegészítő anyagok
A kutatás során olyan kőkiegészítő habarcsok tulajdonságát elemeztük és hasonlítottuk össze a miocén korú durva mészkő két típusának azonos tulajdonságaival (durvaszemű – DMD, és finomszemű – DMF), amelyeket hazai kereskedelmi forgalomban lehet beszerezni. A vizsgálatokat kiterjesztettük továbbá olyan általunk összeállított habarcsokra, amelyek kötőanyagának és töltőanyagának minőségét és mennyiségét mi határoztuk meg. Az így készített habarcsok közül a portlandcement és mészhidrát kötőanyaggal készített habarcsok szilárdsága jelentősen nagyobb volt, mint a vizsgált mészköveké, de porozitásuk, ezáltal hidrotechnikai tulajdonságaik is nagymértékben eltértek a mészkövekétől. Összetételük változtatásával (+30 m%, de elsősorban a +50 m% mészkő zúzalékkal) a kőzetekhez nagyobb hasonlóságot érünk el, de egyes típusoknál ez a beavatkozás nem alkalmazható egyes anyagjellemzők drasztikus változása miatt. A traszcement tartalmú habarcsok vizsgálata során megállapítottuk, hogy a portlandcement kötőanyagú habarcsokhoz képest nagyobb hasonlóságot mutatnak a kiválasztott mészkövek több tulajdonságával is – szilárdság, vízfelvétel, porozitás.
Kulcsszavak: javítóhabarcs, mészkő, kötőanyag/adalékanyag arány, nyomószilárdság, kompatibilitás

Discrete Element Modelling of uniaxial compression test of hardened concrete

Zoltán **GYURKÓ** ▪ MSc candidate, BME , Faculty of Civil Engineering ▪ zoligyurko@gmail.com
Katalin **BAGI** ▪ Prof., BME , Dept. of Structural Mechanics ▪ kbagi@mail.bme.hu
Adorján **BOROSNYÓI** ▪ Assoc. Prof., BME, Dept. of Construction Materials and Engineering Geology
▪ borosnyoi.adorjan@epito.bme.hu

Zoltán Gyurkó
Civil engineer (BSc), MSc student at Budapest University of Technology and Economics, Faculty of Civil Engineering. Main fields of interest: hardness of porous solid building materials, numerical modelling of concrete structures.

Katalin Bagi
Civil engineer (MSc), PhD, DSc, Full Professor at BME Dept. of Structural Mechanics. Main fields of interest: masonry vaults and arches, discrete element modelling, micromechanics of granular materials.

Adorján Borosnyói
Civil engineer (MSc), PhD, Associate Professor at BME Dept. of Construction Materials and Engineering Geology. Main fields of interest: cracking and deflection of reinforced concrete, application of non-metallic (FRP) reinforcements for concrete structures, bond in concrete, nondestructive testing of concrete, supplementary cementing materials for high performance concretes, concrete technology. Member of the fib Task Group 4.1 „Serviceability Models", corresponding member of RILEM Technical Committee 249-ISC „Non destructive in situ strength assessment of concrete" and Chairman of the SZTE Concrete Division.

Abstract

This paper is about the modelling of the compressive strength of hardened concrete by using Discrete Element Method. A short description of the Discrete Element Method is given and the process of the model development as well as the modelling of a uniaxial compression test of a hardened concrete cube is introduced. The aim of the study is to simulate the material behaviour and see how exactly the parameters in the Discrete Element Method can be set up.
Keywords: Discrete Element Method, concrete, stress-strain, compressive strength

1. Introduction of the Discrete Element Method

The Discrete Element Method (DEM) is a family of numerical methods for computing the mechanical behaviour of materials or structures consisting of a large number of particles. In engineering tasks structures often have to be modelled which are composed of granulated material or bricks, and whose components are not connected to each other in a material level. DEM is, therefore, mostly used to model grains, soil, fractured rock, masonry structures like domes and arches. DEM is used extensively to study granular media of no cohesion (Cundall, Strack, 1979), soils with cohesion (Liu *et al*, 2003; Yao, Anandarajah, 2003), rock (Moon *et al*, 2007; Potyondy, Cundall, 2004), asphalt (You, Buttlar, 2004; You *et al*, 2008; Liu, You, 2009), geotechnical and geological studies (Campbell *et al*, 1995; Hardy, Finch, 2006; Hazzard, Young, 2004), for the interaction of granular media (soil and rock) (Kanou *et al*, 2003). In the last two decades the DEM has been successfully applied in various areas of mining, powder metallurgy, civil engineering and in the oil industry. Recently, DEM is also used for the modelling of the behaviour of fresh concrete (Shyshko, Mechtcherine, 2013; Hoornahad, Koenders, 2014; Remond, Pizette, 2014) and hardened concrete (Tran *et al*, 2011; Iturrioz *et al*, 2013; Zivaljic *et al*, 2014; Riera *et al*, 2014).

A numerical technique is said to be a discrete element model if:

- it consists of separate, finite-sized bodies (*discrete elements*) and each of those elements are able to displace independently of each other,
- the displacements of the elements can be large,
- the elements can automatically come into and loose contact (Cundall, Hart, 1992).

With advances in computing power and numerical algorithms for nearest neighbour searching, it has become possible to numerically simulate millions of particles on a single processor (Zhu, 2007). Today DEM is becoming widely accepted as an effective method of engineering problems in granular and discontinuous materials, especially in granular flows, powder mechanics, and rock mechanics. Recently, the method was extended to incorporate Computational Fluid Dynamics (CFD) and Finite Element Method (FEM) and take thermodynamic effects into account. Discrete element methods are relatively computationally intensive, which limits either the length of a simulation or the number of particles. Due to that reason, the method only became practical for engineers in the 1990s, when the computer technology reached the appropriate level where engineers were able to model realistic problems.

If the technical background is given, DEM can be used to examine a wide variety of granular flow and rock mechanics problems. DEM allows a more detailed study of the micro-dynamics of powder flows than is often possible using physical experiments. For example, the force networks formed in a granular media can be visualized using DEM. Such measurements are almost impossible in real experiments with many small particles.

Any type of discrete element model is made up of two basic components: the *elements* and the *contacts* between them. The elements may either directly correspond to the physical units of the analyzed system (e.g. stone voussoirs, sand grains, bricks), or the collection of elements as a whole represents a collection of a much larger number of real particles. The element can have different shapes, even a concave shape, but from a computational point of view circular (2D) or spherical (3D) elements are the easiest to handle, thus they are the most widely used in the current software packages (Bagi, 2012). The elements can be either perfectly rigid or deformable, depending on the application. The contacts are formed when two (or more) elements get in contact. If the distance between the points of two elements decreases to zero then the elements are considered being in contact. This distance can be even less than zero: in this case then the elements intersect with each other, and the magnitude of the overlap defines a compression force

magnitude acting between the two elements. Other contact force components like frictional force, bending moment, tension or torsion are also possible to incorporate. The relationship between the motion of the particles and the forces can be described with Newton's second law. The force system may be in static equilibrium (in which case, there is either no motion at all, or motion occurs only with constant velocities), or it may be such as to cause the particles to accelerate.

The *distinct element method* is a version of DEM proposed by Peter A. *Cundall* in 1971 (Kanou *et al*, 2003). In this method every particle is regarded as a perfectly rigid element and the behaviour of this element is expressed by the equations of motion of extended bodies. A spring is provided between rigid elements which make contact with each other so as to express the interaction of force between them. Then, the equations of motion of each rigid element are solved by numerical integration along the time axis, whereby the behaviour of the element is analyzed. The time integration method works with the central difference method, an explicit solver.

2. Modelling with DEM

During the present research a commercially available DEM software package, the Particle Flow Code (*PFC3D*) of Itasca was used, which is based on the following theoretical assumptions:

1. The particles are treated as rigid bodies.

2. The contacts occur over a vanishingly small area (i.e. at a material point).

3. Behaviour at the contacts is described by a soft-contact approach where the rigid particles are allowed to overlap one another at contact points, and the relative displacements of the two material points forming the contact are considered to reflect the contact deformations which are related to the contact forces.

4. The magnitude of the overlap is related to the compression component of contact force via the corresponding force displacement law, and all overlaps are small in relation to particle sizes.

5. Bonds (i.e. tension-resisting contacts) can also exist between particles.

6. All particles are spherical. However, super-particles of arbitrary shape ("clumps") can be created: overlapping spheres may be glued together to form an irregular particle. Hence, a clump consists of a set of overlapping spherical particles, and behaves as a single rigid body with deformable contacts with its neighbours.

In addition to traditional particle-flow applications, *PFC3D* can also be applied to the analysis of solids. In such models the continuum behaviour is approximated by treating the solid as a compacted assembly of many small particles. In *PFC3D* the particles are linked with contacts which arise when the distance between two particles vanishes. To the analysis of solids so called *cemented contacts* can be applied which can simulate the binder between the particles. Measures of stress and strain rate can be defined as average quantities over a representative measurement volume for such systems. This allows one to estimate interior stresses for granular materials (e.g. soils) or solid materials (e.g. natural stones, metals or plastics).

The *PFC3D* particle-flow model includes two types of elements: *balls* (spherical particles) and *walls*. Walls allow the user to apply velocity boundary conditions to assemblies of balls for purposes of compaction and confinement. The balls and walls interact with each another via forces that arise at the contacts. The equations of motion are satisfied for each ball. However, the equations of motion are not considered for walls (i.e. forces acting on a wall do not influence its motion). Instead, wall motions are specified by the user.

The calculations are performed in *PFC3D* by using two types of rules:

- Newton's second law is applied to determine the motion of each particle arising from the contact and body forces (not applied to walls, since the wall motion is specified by the user).

- Force-displacement law is used to update the contact forces arising from the relative motions at the contacts.

The first step of the discrete element modelling is the preparation of the geometrical model. In this step the position and the shape of the elements are specified. The definition of the geometrical model is relatively simple if the discrete elements exactly correspond to the units of the real structure. However, in several cases (e.g. sand, corn grains stored in a silo, concrete) thousands of densely packed elements (representing a huge number of real particles) have to be defined randomly. In this case a random dense initial arrangement of contacting elements is needed to be prepared. The existing several techniques can be categorized into three main groups:

1. *Dynamic techniques:* In this case the preparation of the initial arrangement is made by the DEM code itself (Bagi, 2012). The elements, initially located far from each other (placed either randomly, or according to a regular arrangement), are pushed into a sufficiently dense arrangement by different ways (e.g. gravitational deposition, isotropic compression, etc), while the motion of each element is followed by the DEM code itself. This method is computationally expensive because each movement of a particle requires the solution of the relevant differential equation.

2. *Constructive algorithms:* In these algorithms the assemblies are prepared with the help of purely geometrical calculations. The user is able to avoid the simulation of the dynamics of particle motions. Therefore, these algorithms are more efficient by orders of magnitude, but the chosen method must be programmed. From these methods the *SSI* (Simple Sequential Inhibition) method is used in the *PFC3D* codes. In this case the spheres of given diameters are placed at random positions in the domain of interest. If a newly placed particle intersects a previous one then the new particle is rejected and the algorithm places another particle into another part of the domain. This process runs after a pre-defined high number of unsuccessful tries to place a new particle in the domain.

3. *Collective rearrangement techniques:* In these methods the number of particles is defined by the user and this number is fixed during the sample preparation process. Initially the particles are placed randomly in the domain of interest. Overlaps are allowed and their sizes are reduced during the process by moving the balls. In every step the displacements of each particle are calculated from the overlaps, similarly to the dynamic techniques. These techniques, like the dynamic methods, are rather time-consuming.

Several contact models can be applied in *PFC3D* to simulate the material behaviour (*PFC3D* User's Guide, 2008). The contact model shows how to derive the contact forces from the deformations (here the deformations mean the relative displacements of the two material points being in contact). *PFC3D* provides two standard contact models for the compression force component (linear and Hertz), which do not consist tensile resistance; and two types of tension-resisting contacts (contact bond and parallel bond). In addition, alternative contact models can be developed by the user. The linear and Hertz models describe the force-displacement behaviour for particle contact occurring at a point. The parallel-bond component, on the other hand, describes the force-displacement and moment-rotation relations for cementitious material existing between the two balls. These two behaviours can occur simultaneously, in the way that one can have a cementitious material (parallel bond), but in the material the particles can also come in contact with each other (linear or Hertz model).

A time stepping algorithm is applied to calculate the movement of the particles, which requires the repeated application of the law of motion to each particle. In the calculation cycle the force-displacement law is used to each contact, and in every cycle the wall positions are also updated. Contacts, which may exist between two balls, or between a ball and a wall, are formed and broken automatically during the course of a simulation. At the start of each time step the set of contacts is updated from the known positions of particles and walls. The force-displacement law is then applied to each contact to update the contact forces based on the existing relative displacement between the two entities at the contact. Next, the law of motion is applied to each particle to update the velocity and position, based on the resultant force and moment arising from the contact forces and any body forces (gravity etc.) acting on the particle. Also, the wall positions are updated based on the specified wall velocities (*Fig. 1*).
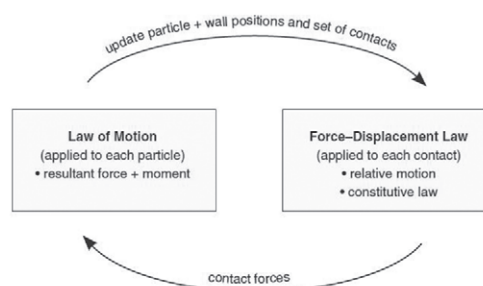

Fig. 1. Calculation cycle in PFC3D (PFC3D User's Guide, 2008)
1. ábra Számítási ciklus a PFC3D szoftverben (PFC3D User's Guide, 2008)

3. Material genesis

In the present study the compression stress-strain performance of a standard concrete cube (150 mm) was modelled with DEM and was verified with laboratory experiments. The concrete was modelled with a large number of discrete elements (*Fig. 2*), each of them being spherical. The element diameters in the model of the concrete cube were based on the aggregate sizes used in the real material. In the model the actual particle size distribution of the aggregate used for the reference concrete was intended to approximate. The particle size distribution was compiled from the applicable grading limit curves for 16 mm maximum particle size flint aggregate, taking into account the minimum demand of cement paste (void volume) of the fully compacted aggregate bulk. The minimum and maximum diameter of the elements was 1 mm and 16 mm respectively. The particle size distribution of the original material is given in *Table 1*.
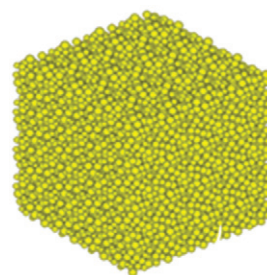

Fig. 2. Discrete element model of a concrete cube
2. ábra Egy beton kocka diszkrét elemes modellje

Particle size	Proportion
0-4 mm	40 %
4-8 mm	22 %
8-16 mm	38 %

Table 1. Particle size distribution of the aggregate in the concrete sample studied
1. táblázat A vizsgált beton adalékanyagának szemcseméret eloszlása

The three particle size fractions (0-4 mm, 4-8 mm and 8-16 mm) were created and the volume of fractions was set regarding the particle size distribution of the original aggregate material. During this phase of the modelling one has to specify five parameters to every fraction:

1. The minimum radius of the material in the fraction.
2. The radius ratio; that is the ratio of the maximum to the minimum radius.
3. The ratio of the volume of the particles in the given fraction, related to the total volume.
4. The distribution type of the given fraction. In the present study the fractions are uniformly distributed.
5. The name of the fractions to identify them.

To improve the speed of the computation, the built-in functions offered by the software can be used. These built-in functions use constructive algorithms, which are more effective in certain cases where the difference in size among the balls is large. An extensive set of supporting algorithms are required if one would like to model a solid material correctly.

These algorithms are:

- to create the synthetic solid by using constructive algorithms,
- to determine the required macroscopic properties of the material, by subjecting it to simulated laboratory testing,
- to either apply stress boundary conditions or install a specified stress field within the solid,
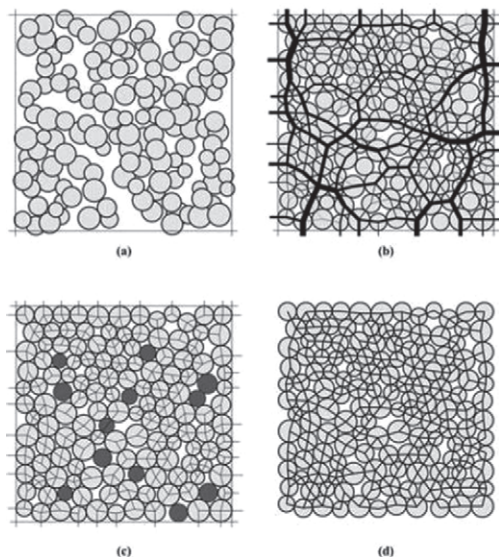- to monitor and visualize damage formation within the solid.

Fig. 3. *Material genesis procedure: (a) particle assembly after initial generation but before rearrangement; (b) contact force distribution after the second step; (c) floating particles and contacts after the second step; (d) parallel-bond network (PFC3D User's Guide, 2008)*

3. ábra *Anyag generáló eljárás: (a) szemcsék kezdeti elrendeződése az újrarendezést megelőzően; (b) az érintkezési erők folyama a második lépésben; (c) lebegő szemcsék és érintkezési pontok a második lépésben; (d) a párhuzamos kötések hálózata (PFC3D User's Guide, 2008)*

These algorithms are built in the software into a given storage of supporting algorithms, called *Fishtank*, which name refers to the FISH programming language that used in *PFC3D*. To model concrete the so called Material-Genesis Procedure was used, which produces a material consisting of grains and cement (*PFC3D* User's Guide, 2008). During this procedure (*Fig. 3*) first an initial assembly is created, in which the particles are placed randomly (with a 35% porosity) with a much smaller radius than the required, and without particle overlapping. Then, the particle radii are gradually increased to their final values and the system is allowed to reach static equilibrium under zero friction. Then the radii of the particles are changed uniformly to achieve a specified isotropic stress (mean value of the three principal stresses). This is a typically low value relative to the material strength (less than 0.01% of the uniaxial compressive strength). After the first two steps an assembly of randomly placed particles with non-uniform radii is produced. These assemblies can contain a large number of *floating* particles (those which have fewer than three contacts). It is desirable to reduce the number of this type of elements, in order to obtain a denser network of bonds. After all of the contact bonds and parallel bonds are installed, the specified friction coefficient is assigned to the contacts. The material vessel can be removed

and the specimen can be used for a boundary-value simulation or it can be subjected to material testing. This widely applied procedure was followed in the investigations introduced in the present paper.

4. Parameter settings

The built-in functions introduced earlier can make the preparation of the initial geometry faster, but to achieve an acceptable result, one should also set the correct contact material parameters. The most important parameters which influence the behaviour of the model are the density of the balls, the friction coefficient in the unbonded contacts, as well as the shear and normal stiffness and strength of the bonds. To set up the parameters correctly a uniaxial compression test in *PFC3D* was completed and compared to the experimental results. The initial values of the different parameters were obtained from the literature on concrete modelling (Szilágyi, 2009). The bulk modulus of the balls is considered as a constant (it is equal to 1), corresponding to the infinite rigidity of the elements.

Parameters of the elements:

- Bulk modulus = 1 (infinitely rigid discrete elements)
- Ball or bulk density = 2300 kg/m^3 (density of concrete)
- Friction coefficient = 0.40

Parameters of the parallel bonds (Szilágyi, 2009):

- The mean value of the normal strength = $5×10^7$ N/m^2
- The standard deviation of the normal strength = $5×10^6$ N/m^2
- The mean value of the shear strength = $3×10^6$ N/m^2
- The standard deviation of the shear strength = $3×10^5$ N/m^2
- The stiffness of the parallel bonds = $3×10^{10}$ N/m^2

The standard deviation of the normal strength was set to tenth of the mean value of the normal strength during the modelling, based on literature recommendations. To find the final parameters of the model, which represent the real behaviour of the material, an iteration method was applied. This is the usual solution in case of DEM models during the verification phase. The verification was made with the help of the uniaxial compression test.

The iteration process had the following steps:

1. Set the parameters (mean strength and standard deviation of the strength of the parallel bonds) of the model to a given value. These two parameters have the largest effect on the normal stiffness of the model, therefore, they were adjusted first during the iterations. The other parameters had only minor effects, so those parameters were modified after the iteration phase during the fine-tuning of the model.
2. Generating the model with a dense packing.
3. Run a uniaxial compression test.
4. Compare the value of the test with the results of the laboratory tests. If the value of the normal strength is higher in the model, then the mean strength of the parallel bonds can be reduced, if the value of the normal strength is lower in the model, then the mean strength of the parallel bonds can be increased until the same result as in the experimental test was reached.

After the appropriate properties of the model were selected, four additional models were generated with the same average properties but differing from each other by the random nature of the particle-level geometry generated. Testing and analyses were carried out on the five models. The aim was to study the statistical nature of the behaviour, and to be able to avoid extreme numerical results in the analyses.

5. Compression test

The compression test can be simulated by the built-in functions of the *PFC3D* software pre-programmed in the *Fishtank*, and the user can calibrate the test to the actual specimens of interest. The process is the following. First the sidewalls of the sample are deactivated. It can be given, which walls are the sidewalls of the sample and the test can be done along all three axes. The friction of the remaining walls is set to a high value, because in case of the real test, the friction between the loading plate and the sample is high. The bottom wall remains fixed and the top wall pushes the sample with a given force or velocity until it destroys the sample (i.e. the sample is not able to bear any more stress). The software tracks the bond break events during the investigation which represent cracks. The cracks are defined with the Crack-Initiation Stress, which is controlled by the ratio of standard deviation to mean material strength (*PFC3D* User's Guide, 2008). If the ratio increases, it reduces the stress at which the first crack initiates. It is usually observed that the Crack-Initiation Stress in a *PFC3D* specimen underestimates the Crack-Initiation Stress measured during laboratory experiments. The Crack-Initiation Stress is defined as the axial stress at which a specified fraction of the total number of cracks exists in the model at the point when the peak stress is obtained. When the test is finished, the software saves the results into a text file and one can analyze it without running the program. The results are given in three different ways since the software is able to measure stresses in a different ways. The three types are:

- wall-based results,
- by using gauge particles,
- by using measurement spheres.

All the three measurement methods can be used for measuring both stresses and Young modulus. The result of the compression test can be considered successful if the Young modulus has almost exactly the same value as it was given in the parameter settings. If the Young modulus is different then the model is not numerically stable (by proceeding the compression test, very different results can be received) and the parameters are not well defined.

The result of the compression test was used to calibrate the model by the comparison with the laboratory test results. The laboratory test was carried out in laboratory of the Budapest University of Technology and Economics (BME), Department of Construction Materials and Engineering Geology. To determine the real compressive strength of the reference concrete an Alpha 3-3000 S type (Form-Test) universal hydraulic testing machine was used (*Fig. 4*). Standard cube (150 mm) specimens were prepared, which were stored under water for 7 days and under laboratory condition for 21 days. Before the tests the specimens

were dried in oven at 40°C temperature. Compressive strength testing was carried out according to EN 12390-3. Average value of the compressive strength for the reference concrete was found to be f_{cm} = 54.2 N/mm².

Fig. 4. Compressive strength testing
4. ábra Nyomószilárdság vizsgálata

6. Results

The final values of the parameters of the DEM model were reached after several iteration steps. The most important results are indicated in *Table 2*. It can be realized that the proper set of the parameters resulted exact coincidence of the normal strength with the compressive strength recorded during the laboratory tests.

Mean value of the normal strength [N/m²]	Standard deviation of the strength of the parallel bonds [N/m²]	Mean value of the shear strength [N/m²]	Normal strength of the material [N/m²]
4.251*10⁷	4.251*10⁶	3*10⁶	54.24*10⁶

Table 2. Calculated internal forces
2. táblázat Számított belső erők

As it was mentioned above, four additional models were also generated. In the numerical compression tests, the generated models behaved very similarly to each other and gave almost the same normal strength value than that of the compression test of the first model. All values were in a 0.5 % range compared to the result generated by the first model (*Table 3*).

No. of the model	1	2	3	4	5
Normal strength (N/mm²)	54.24	54.19	54.26	54.03	54.20

Table 3. Normal strengths corresponding to the five models
3. táblázat Az öt eltérő modellből számított normálfeszültségek

From the values given in Table 3 the Young's modulus of the concrete can be recalculated by Eq. (1):

$$E_c = 10.000 \times f_c^{\frac{1}{3}} \qquad (1)$$

where, f_c is the normal strength of the model. By using an average value of the model data, the value of the recalculated Young modulus is 37840 N/mm² that gives considerably good agreement with the Young's modulus of 34578 N/mm² recorded during the laboratory tests.

The process of the compression test can be plotted by using the *PFC3D* software, which monitors the deviatoric stress in the function of axial strain during the test procedure. *Fig. 5* shows the plot of deviatoric stresses over axial strain. The curve from the model behaves quite similarly to the typical concrete stress-strain curves. As a difference it can be seen, that at the initial stage of the curve waving of the response can be observed. In case of the real laboratory tests this stage is linear. The behaviour was observable in case of all the five models tested numerically. During the phenomenon, first the stress increases fast without large strains, later it turns to the opposite and one can observe strain increments without significant stress changes. The behaviour can be explained by the structure of the DEM model, which contains bonds and particles. After the material genesis procedure the model is stable and until a given point (depending on the stiffness of the parallel bonds) no bonds are breaking and the model has no significant deformations. However, after some parallel bonds become broken and some particles (mostly in the vicinity of the loading planes; it is a local behaviour of the model) are able to make movements, a deformation occurs in the model. When a new stable configuration is formed, the process can be started again. After some cycles this behaviour vanishes since the pressure influences the complete volume of the specimen and the local behaviour becomes global. It can be seen in *Fig. 5* that the axial strain resulted from the model gives reasonable value of 3 to 5‰ typical for concretes in the range of compressive strength of the reference concrete used in the laboratory tests.

It can be concluded that the presented numerical simulations and experimental verification has been clearly demonstrated the possible use of DEM for a suitable approximation of the behaviour of concrete material under uniaxial compression test.
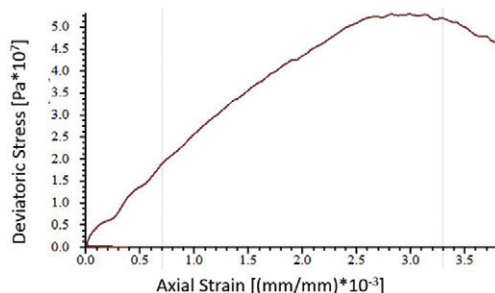

Fig. 5.   The deviatoric stress vs. the axial strain during the compression test procedure
5. ábra   A deviátoros feszültség és a tengelyirányú fajlagos összenyomódás kapcsolata

7. Future work

It has been demonstrated by the presented laboratory and numerical simulation results that DEM can be a robust tool for the modelling of stress-strain behaviour of hardened concrete in compression as well as for the accurate estimation of Young's modulus and (cube) compressive strength of hardened concrete. The developed model is planned to be submitted to different refinements in which the effect of aggregate particle size distributions, aggregate shapes, different cement types and specimen geometries can be studied; that are addressed to future work.

8. Conclusions

It was shown in this paper – based on the evaluation of a numerical simulation and experimental verification – that Discrete Element Method (DEM) is capable of modelling the uniaxial compression testing method of hardened concrete cube specimens, and after a sufficient parameter set up the model can led to results that are strongly correlated to real laboratory test observations. Compressive strength, Young's modulus and stress-strain response can be reproduced with high accuracy. With the help of DEM modelling, the laboratory test procedures can be easily simulated and the numerical tests can be repeated multiple times to follow random material behaviour. Statistically reasonable results can be created without the need of a large companion of laboratory tests that may add to the better understanding of material behaviour and failure process of hardened concrete.

References
[1] Bagi, K. (2012): Fundamentals of the discrete element method, *Lecture notes,* BME Faculty of Civil Engineering, Budapest, 2012
[2] Cundall, P. A. – Hart, D. H. (1992): Numerical modeling of discontinua, *Engineering Computations*, Vol. 9, No. 2, pp. 101-113.
http://dx.doi.org/10.1108/eb023851
[3] Cundall, P. A. – Strack, O. D. L. (1979): A discrete numerical model for granular assemblies. *Geotechnique*, Vol. 29, No. 1, pp. 47–65.
http://dx.doi.org/10.1680/geot.1979.29.1.47
[4] Campbell, C. S. – Cleary, P. W. – Hopkins, M. A. (1995): Large-scale landslide simulations: Global deformations, velocities, and basal friction. *Journal of Geophysical Research*, Vol. 100, No. B5, pp. 8267–8283.
http://dx.doi.org/10.1029/94JB00937
[5] Hardy, S. – Finch, E. (2006): Discrete element modelling of the influence of cover strength on basement-involved fault-propagation folding. *Tectonophysics*, Vol. 415, No. 1–4, pp. 225–238.
http://dx.doi.org/10.1016/j.tecto.2006.01.002
[6] Hazzard, J. F. – Young, R. P. (2004): Dynamic modelling of induced seismicity. *International Journal of Rock Mechanics and Mining Sciences,* Vol. 41, No. 8, pp. 1365–1376.
http://dx.doi.org/10.1016/j.ijrmms.2004.09.005
[7] Hoornahad, H. – Koenders E. A. B. (2014): Simulating macroscopic behavior of self-compacting mixtures with DEM. *Cement & Concrete Composites*, Vol. 54, pp. 80-88.
http://dx.doi.org/10.1016/j.cemconcomp.2014.04.006
[8] Itasca Consulting Group, Inc. PFC3D User's Guide, 2008
[9] Iturrioz, I. – Lacidogna, G. – Carpinteri, A. (2013): Experimental analysis and truss-like discrete element model simulation of concrete specimens under uniaxial compression. *Engineering Fracture Mechanics*, Vol. 110, pp. 81-98.
http://dx.doi.org/10.1016/j.engfracmech.2013.07.011
[10] Kanou, S. – Amano, M. – Terasaka, Y. – Matsumoto, N. – Wada, T. (2003): Terra-mechanical simulation using distinct element method. *Komatsu Technical Report*, Vol. 49, No. 151, pp. 13–19.
http://www.komatsu.com/CompanyInfo/profile/report/pdf/151-04_E.pdf
[11] Liu, S. H. – Sun, D. A. – Wang, Y. (2003): Numerical study of soil collapse behavior by discrete element modelling. *Computers and Geotechnics*, Vol. 30, No. 5, pp. 399–408.
http://dx.doi.org/10.1016/S0266-352X(03)00016-8
[12] Liu, Y. – You, Z. (2009): Visualization and simulation of asphalt concrete with randomly generated three-dimensional models. *ASCE Journal of Computing in Civil Engineering*, Vol. 23, No. 6, pp. 340–347.
http://dx.doi.org/10.1061/(ASCE)0887-3801(2009)23:6(340)
[13] Moon, T. H. – Nakagawa, M. – Berger, J. R. (2007): Measurement of fracture toughness using the distinct element method. *International Journal of Rock Mechanics and Mining Sciences,* Vol. 44, No. 3, pp. 449–456.
http://dx.doi.org/10.1016/j.ijrmms.2006.07.015

[14] Potyondy, D. O. – Cundall, P. A. (2004): A bonded-particle model for rock. *International Journal of Rock Mechanics and Mining Sciences*, Vol. 41, No. 8, pp. 1329–1364. http://dx.doi.org/10.1016/j.ijrmms.2004.09.011

[15] Remond, S. – Pizette, P. (2014): A DEM hard-core soft-shell model for the simulation of concrete flow. *Cement and Concrete Research*, Vol. 58, pp. 169-178. http://dx.doi.org/10.1016/j.cemconres.2014.01.022

[16] Riera, J. D. – Miguel, L. F. F. – Iturrioz, I. (2014): Assessment of Brazilian tensile test by means of the truss-like Discrete Element Method (DEM) with imperfect mesh. *Engineering Structures*, Vol. 81, pp. 10-21. http://dx.doi.org/10.1016/j.engstruct.2014.09.036

[17] Shyshko, S. – Mechtcherine, V. (2013): Developing a Discrete Element Model for simulating fresh concrete: Experimental investigation and modelling of interactions between discrete aggregate particles with fine mortar between them. *Construction and Building Materials,* Vol. 47, pp. 601-615. http://dx.doi.org/10.1016/j.conbuildmat.2013.05.071

[18] Szilágyi, K. (2009): DEM modelling of the Brinell-testing of concrete, *Micromechanics of granular media – Manuscript*, BME Faculty of Civil Engineering, Budapest, 2009

[19] Tran, V. T. – Donzé, F.-V. – Marin, P. (2011): A discrete element model of concrete under high triaxial loading. *Cement & Concrete Composites,* Vol. 33, No. 9, pp. 936–948.

http://dx.doi.org/10.1016/j.cemconcomp.2011.01.003

[20] Yao, M. – Anandarajah, A. (2003): Three-dimensional discrete element method of analysis of clays. *Journal of Engineering Mechanics,* Vol. 129, No. 6, pp. 585–596.

http://dx.doi.org/10.1061/(ASCE)0733-9399(2003)129:6(585)

[21] You, Z. – Adhikari, S. – Dai, Q. (2008): Three-dimensional discrete element models for asphalt mixtures. *Journal of Engineering Mechanics,* Vol. 134, No. 12, pp. 1053–1063.

http://dx.doi.org/10.1061/(ASCE)0733-9399(2008)134:12(1053)

[22] You, Z. – Buttlar, W. G. (2004): Discrete element modeling to predict the modulus of asphalt concrete mixtures. *ASCE Journal of Materials in Civil Engineering,* Vol. 16, No. 2, pp. 140–146.

http://dx.doi.org/10.1061/(ASCE)0899-1561(2004)16:2(140)

[23] Zhu, H. P. – Zhou, Z. Y. – Yang, R. Y. – Yu, A. B. (2007): Discrete particle simulation of particulate systems: Theoretical developments. *Chemical Engineering Science,* Vol. 62, No. 13, pp. 3378–3396. http://dx.doi.org/10.1016/j.ces.2006.12.089

[24] Zivaljic, N. – Nikolic, Z. – Smoljanovic, H. (2014): Computational aspects of the combined finite–discrete element method in modelling of plane reinforced concrete structures. *Engineering Fracture Mechanics,* Vol. 131, pp. 669-686. http://dx.doi.org/10.1016/j.engfracmech.2014.10.017

Megszilárdult beton nyomószilárdság vizsgálatának modellezése diszkrét elemes módszerrel

A cikk megszilárdult beton nyomószilárdságának numerikus modellezését ismerteti a diszkrét elemes módszer (DEM) felhasználásával. A diszkrét elemes módszer rövid bemutatását követően a numerikus modell felépítését és a nyomószilárdság vizsgálat numerikus szimulációjának eredményeit ismertetjük. A numerikus kísérlet eredményeit tényleges nyomószilárdság vizsgálat eredményeivel hasonlítjuk össze. Bemutatjuk, hogy a diszkrét elemes módszerrel konstruálható olyan szemcseösszetétel, amely pontosan követi a vizsgált beton adalékanyagának szemeloszlását, numerikusan stabil, és paraméterei beállíthatók oly módon, hogy a tényleges nyomószilárdság és rugalmassági modulus csaknem teljes pontossággal előállíthatóvá válik.

Kulcsszavak: diszkrét elemes módszer, beton, feszültségalakváltozás, nyomószilárdság

Image digitalization as a tool for processing experimental data of crack width of concrete

Réka Anna Nagy
Civil engineer (MSc, Budapest University of Technology and Economics), PhD candidate at Department of Construction Materials and Engineering Geology. Main fields of interest: cracking of concrete, durability of structural materials, use of FRP reinforcements for concrete structures.

Réka NAGY ▪ MSc (CE), PhD candidate, BME Dept. of Construction Materials and Engineering Geology
▪ nagy.reka@epito.bme.hu

Abstract

The present paper introduces a new approach for the continuous measurement of the width of structural cracks within the concrete cover by image digitalizing and digital image processing methods. It is demonstrated that crack width measurement may hold reading error if an operator reads the crack widths by hand microscope or by digital microscope at locations chosen by subjective means. It is highlighted that the tortuosity of structural cracks in concrete can be mapped and described only by detailed image processing methods.
Keywords: concrete, crack width, digital image processing, tortuosity

1. Introduction

Mechanical and durability performance of reinforced concrete structures is considerably influenced by structural cracks formed during flexural or direct tensile loading. Structural cracks have an effect both to serviceability and load bearing capacity. The increase of deformations due to the decreased stiffness at a cracked section may result unacceptable appearance or changing the static system. The increased permeability of cracked concrete may result advanced ingress of CO_2 and aqueous solutions towards the steel reinforcing bars, increasing the risk of corrosion. Water leakage can result unacceptable functional or aesthetical condition. Results of structural cracking can reduce the service life of structures, therefore, several literature studies are available in the field. No general conclusion, however, is available on the role of structural cracking and durability; the only observations are that the corrosion of reinforcement is independent from the surface crack widths and the corrosion of reinforcement is accelerated in the presence of chloride ions [1-7].

The width of a structural crack at the surface of the reinforcement depends primarily on the diameter of the reinforcing bar, the surface configuration of the reinforcing bar, the Young's modulus of the reinforcing bar, the strength of concrete, the magnitude of the effective concrete area in tension and the stress in the reinforcing bar. This latter one can be considered to be the most important influencing parameter. The width of a structural crack within the concrete cover is, however, different from that of measured at the surface of the structural element [8-11]. Comprehensive analysis of this behaviour is a gap in the technical literature.

2. Significance

Deformations of concrete in the vicinity of cracks are developed as a result of a very complex phenomenon of the composite material. It is the reason why no model is available in the technical literature that would allow conversion of crack widths *at the surface of the reinforcing bars* into the crack widths that appear on the *outer surface of the concrete elements*.

Only limited number of publications is available in the technical literature that tried to analyse the crack width along the concrete cover and tried to determine what type of relationship could be supposed between the crack widths at the surface of the reinforcing bars and that of on the outer surface of concrete structures [8-12]. Based on the available literature data it can be concluded that some kind of proportionality is possible to be found between the crack width at the surface of the reinforcing bars and that of on the outer surface on the concrete structure (emphasizing that the validity of the published results are restricted to the testing conditions). The published range is:

$$w_{outer\ surface} / w_{reinforcement\ surface} = 1.1\ to\ 7.7$$

It should be emphasized that the ratio depends on the magnitude of concrete cover, the load level (steel stress), the strength of concrete, the Young's modulus of concrete, the surface configuration of the reinforcing bar.

3. Previous studies

Borosnyói and *Snóbli* (2010) have studied reinforced concrete tie elements of 120×120 mm cross section and 900 mm length reinforced with one single Ø20 mm deformed steel reinforcing bar placed either concentrically or eccentrically [13]. Concrete covers were 20, 40, 60, 80 mm for the eccentric specimens and 50 mm for the concentric specimens.

Injection of structural cracks was carried out from the surface of the members and the detailed mapping of the internal crack width variation within the concrete cover was studied. Epoxy resin was used for the injection. The cracks were maintained in their original, loaded position and the axial load was released only after the resin was allowed to set. Surface crack pattern and surface crack widths were recorded and then the specimens were cut open by a high speed diamond saw. Crack widths were recorded by a hand microscope (scale of 0.01 mm) at every 2 mm along each crack. Present paper gives a comprehensive analysis of the same test specimens that were used in [13].
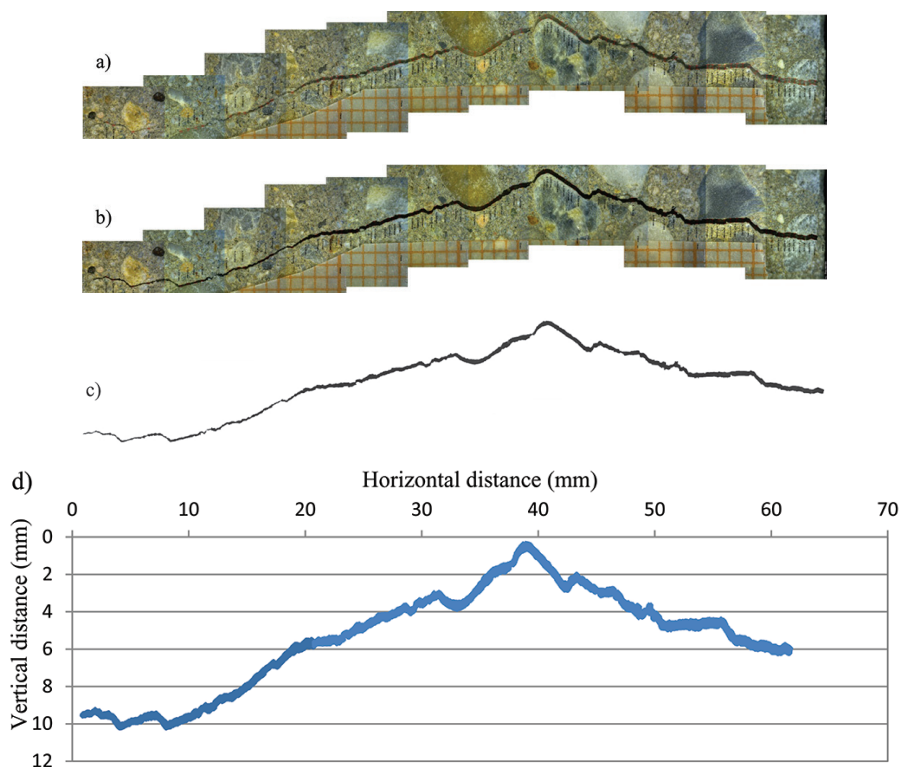
Fig. 1.   Steps of digitalization a) original image b) crack after contrast adjustment c) separated crack d) crack drawn by pixel coordinates
1. ábra   Digitális képfeldolgozás lépései a) az eredeti felvétel b) a repedés a kontraszt kiemelése után c) az elkülönített repedés d) a pixel koordináták alapján megrajzolt repedés

4. Refining possibilities

The drawback of the classic optical crack width measurement method is that the read values depend on the person's sensory sensitivity who carries out the measurement and all specimens are needed to be stored if more data would like to be gathered for further analysis.

The images of the cracks formed during the laboratory tests detailed in [13] were scanned by the author with a digital microscope. Crack widths were chosen to be read at every 0.5 mm along their length with the data analyzing software provided with the microscope. Details of the digital readings and analysis are given elsewhere [14]. The images of the cracks, therefore, became available as digital images to be processed later and more data can be obtained compared to the hand microscope recordings. It can be emphasized, however, that the accuracy of the scanned data analysis with the use of commercial software still depends on the person's subjective decisions during the readings when the location of points for measurements are chosen. If one could provide a more comprehensive analysis that is free of bias then a full length digital processing of the digital images of the crack width recordings should be developed.

5. Digitalizing

Describing the variation of crack width within the concrete cover can help to explain the possible correlation between surface crack width and corrosion, if any. Therefore, it is needed to find a method to process experimental data that is objective and repeatable in the survey of crack width variation along cracks.

Digital image processing provides the possibility of pixel-depth analysis of digital images. The first task during digital processing of the scanned images is the contrast adjustment so that the points within the crack can be represented in high contrast and can be differentiated from the surroundings. *Fig. 1.a* indicates the original scanned images and *Fig. 1.b* shows the picture of the crack after contrast adjustment. Then the crack is separated from the surroundings (*Fig. 1.c*) and the image is subjected to numerical analysis to find coordinates of the points along the crack. As a result, the crack can be described by pixel coordinates (*Fig. 1.d*) and numerical calculations can be carried out.
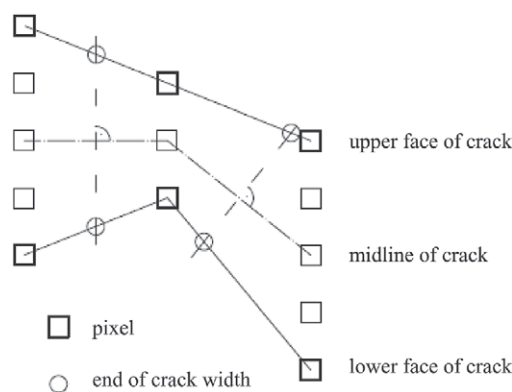

Fig. 2.   Defining crack width – schematic diagram
2. ábra   A repedéstágasság leolvasás elvi sémája

The crack width is defined as the distance between the crack faces along a line perpendicular to the midline of the crack, as represented in *Fig. 2*. In order to calculate crack width, the

coordinates of the pixels of the crack faces are needed to be determined first. Then the position of the pixels corresponding to the midline can be defined and the perpendicular lines can be taken at arbitrary frequency. Coordinates define splines, along which the position of the perpendiculars (on the midline) and the intersection points (on the crack faces) can be determined outside the original pixels as well.
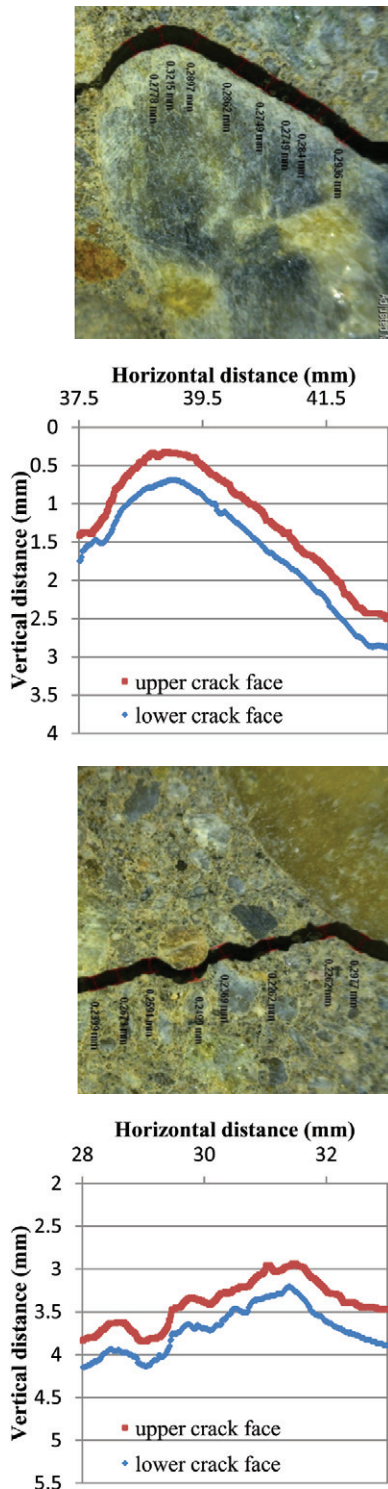

Fig. 3. Scanned images of cracks together with the corresponding crack face coordinates
3. ábra Repedések szkennelt képe és a repedésszélek koordinátapontjai

Fig. 3 indicates scanned images for two sections of cracks together with arbitrary crack width readings that are compared to the digitalized pixel coordinates of upper and lower crack faces. It can be realized that the coordinates of upper and lower crack faces are well defined and indicate the possibility of crack width measurement with a suitable numerical approach.

6. Results and analysis

The crack width measurement results obtained by numerical analysis of the digitalized crack width pixel data for an arbitrary crack are presented in *Fig. 4* together with the recordings of the same crack with the methods described in Chapter 3 and 4. The values are in good accordance for all the three measuring methods. It can be realized that the crack width values obtained by the introduced numerical analysis of the digitalized crack width pixel data show more scattered behaviour. It is attributed to the fact that the number of readings was different for the three different methods.

During recording of crack widths by hand microscope or by the commercial analysis software of the digital microscope one makes readings at fewer points and human eye chooses measurement points that are easy to read while the results of the numerical analysis of the digitalized crack width pixel data show the real values of crack width with all its unevenness.

It can be also seen that the sensitivity of human eye reading is very much limited at the range of 0.01 mm that was the scale of the hand microscope used in [13] – human eye notoriously reads lower crack width values than the real magnitude.
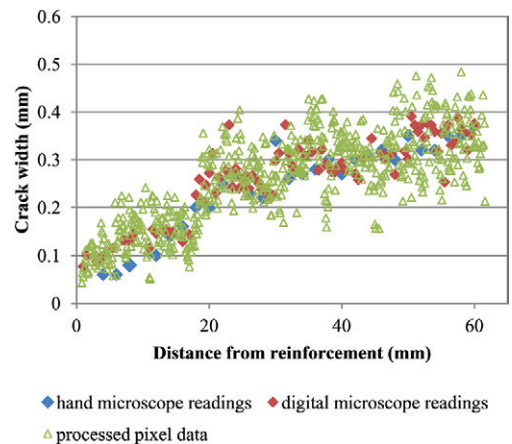

Fig. 4. Comparison of crack widths measured with hand microscope, digital microscope readings and image processing
4. ábra Repedéstágasság összehasonlítása kézi mikroszkóppal, digitalis mikroszkóppal történő leolvasás és pixeles feldolgozás esetében

Based on the findings of *Fig. 4*, it is also possible to estimate the relative error and precision of the crack width measurements by the three different methods. *Fig. 5* indicates the differences between the crack width readings for hand microscope vs. processed pixel data, digital microscope readings vs. processed pixel data and hand vs. digital microscope methods, respectively. Relative error can be represented as the average of the differences in the measurements while relative precision can be represented as the standard deviation of the differences in the measurements (*Table 1*).
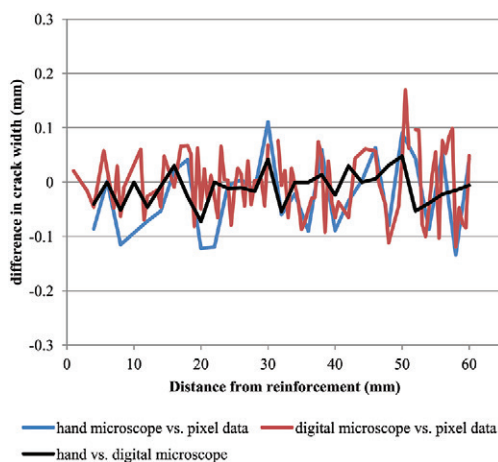
Fig. 5. Comparing the difference of the three methods
5. ábra A három tárgyalt módszer különbségeinek összehasonlítása

Crack width difference (mm):	average	standard deviation
hand microscope - pixel data	-0.023	0.0702
digital microscope - pixel data	-0.002	0.0598
hand - digital microscope	-0.009	0.0293

Table 1. Difference of crack widths by the three methods
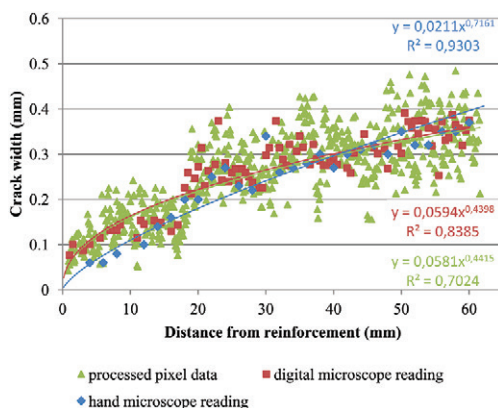*1. táblázat* Repedéstágasság különbség a három módszerrel

Fig. 6. Comparison of crack widths measured with hand microscope, digital microscope readings and image processing (trend analysis)
6. ábra Repedéstágasság összehasonlítása kézi mikroszkóppal, digitalis mikroszkóppal történő leolvasás és pixeles feldolgozás esetében (trendvonalak bemutatásával)

Digital microscope readings and the values obtained by image processing show low relative error compared to each other while hand microscope readings and the processed data show higher relative error compared to each other. The difference between the calculated relative errors is in the order of about ten (*Table 1*). Expectedly, the magnitude of the relative error when comparing hand microscope readings and digital microscope readings is found between the other two values. One reason of the findings may be the instinctive distortion of the reading location selection of human observer when using either hand microscope or digital microscope for the crack width measurements. During such readings the observer has free choice to select the exact reading locations even if a ruler is followed for spacing of readings and may select locations which are considered to provide kind of representative values for the crack width. The less is the number of the readings, the

higher value of the error may be resulted. Another possible reason can be the lack of calibration of the hand microscope device that results bias of the measured values. The third reason is the intrinsic driving force of the observations that is the real tortuosity of the crack. The more sophisticated is the survey of the crack geometry, the more detailed information becomes available on tortuosity. It can be realized from the present study that changing the number of observations has a considerable influence on the visibility of tortuosity of the crack (*Fig. 6*). Future numerical analysis of digitalized crack width pixel data is needed to see the possibilities of modelling crack tortuosity in concrete since tortuosity is an important parameter of permeability of cracked concrete.

7. Conclusions

The width of structural cracks within the concrete cover is different from that of measured at the surface of the structural elements. Only limited number of publications is available in the technical literature that tried to analyse the crack width along the concrete cover. Experimental results of previous study by *Borosnyói* and *Snóbli* [13] is analysed further in this paper after digital scanning of the surface of the same specimens and digital image processing of the obtained data. The proposed method is demonstrated to be useful for detailed survey and analysis of crack widths within the concrete cover. It is highlighted that human eye sensory sensitivity and subjective readings of human observer hold reading error. It is shown that changing the number of observations has a considerable influence on the visibility of tortuosity of structural cracks of concrete.

References

[1] Beeby, A. (1983): Cracking, cover and corrosion of reinforcement, *Concrete International*, Vol. 5, No. 2, 1983, pp. 35–40.

[2] Darwin, D. (1985): Debate - Crack Width, Cover, and Corrosion. *Concrete International*, Vol. 7, No. 5, 1985, p. 20-35.

[3] Berke, N. S. – Dellaire, M. P. – Hicks, M. C. – Hoopes, R. J. (1993): Corrosion of Steel in Cracked Concrete. *Corrosion*, Vol. 49, No. 11, 1993, p. 934-943.
http://dx.doi.org/10.5006/1.3316020

[4] Jacobsen, S. – Marchand, J. – Boisvert, L. (1996): Effect of cracking and healing on chloride Transport in OPC concrete. *Cement and Concrete Research*, Vol. 26, No. 6, 1996, pp. 869–881.
http://dx.doi.org/10.1016/0008-8846(96)00072-5

[5] Schiessl, P. – Raupach, M. (1997): Laboratory studies and calculations on the influence of crack width on chloride-induced corrosion in concrete, *ACI Materials Journal*, Vol. 94, No. 1, 1997, pp. 56-61.
http://dx.doi.org/10.14359/285

[6] Otsuki, N. – Miyazato, S. – Diola, N. – Suzuki, H. (2000): Influences of bending crack and water–cement ratio on chloride-induced corrosion of main reinforcing bars and stirrups, *ACI Materials Journal*, Vol. 97, No. 4, 2000, pp. 454–464.
http://dx.doi.org/10.14359/7410

[7] Vidal, T. – Castel, A. – Francois, R. (2004): Analyzing crack width to predict corrosion in reinforced concrete. *Cement and Concrete Research*, Vol. 34, 2004, pp. 165-174.
http://dx.doi.org/10.1016/S0008-8846(03)00246-1

[8] Broms, B. (1965): Crack width and crack spacing in reinforced concrete members, *ACI Journal*, Vol. 62, No. 10, 1965, pp. 1237-1256.
http://dx.doi.org/10.14359/7742

[9] Husain, S. I. – Ferguson, P. M. (1968): Flexural Crack Widths at the Bars in Reinforced Concrete Beams. *Center for Highway Research*, The University of Texas at Austin, Research Report No. 102,1F, 1968.

[10] Tammo, K. – Thelandersson, S. (2006): Crack opening near reinforcement bars in concrete structures. *Structural Concrete*, Vol.7, No. 4, 2006, pp. 137–143. http://dx.doi.org/10.1680/stco.2006.7.4.137

[11] Yannopoulos, P. J. (1989): Variation of concrete crack widths through the concrete cover to reinforcement. *Magazine of Concrete Research*, Vol. 41, No. 147, 1989, pp. 63–68. http://dx.doi.org/10.1680/macr.1989.41.147.63

[12] Borosnyói, A. (2010): Bond of carbon fibre reinforced polymer (CFRP) prestressing tendons in concrete. Multi-parameter laboratory studies, *Építés – Építészettudomány*, Vol. 38. No. 1-2. 2010, pp. 95-120. (in Hungarian) http://dx.doi.org/10.1556/EpTud.38.2010.1-2.5

[13] Borosnyói A. – Snóbli I. (2010): Crack width variation within the concrete cover of reinforced concrete members, *Építőanyag-JSBCM*, Vol. 62, No. 3., pp. 70-74. http://dx.doi.org/10.14382/epitoanyag-jsbcm.2010.14

[14] Nagy, R. (2013): Structural cracking of reinforced concrete members, *Second Conference of Junior Researchers in Civil Engineering*, 17-18 June 2013, Budapest, Hungary, pp. 136-141. https://www.me.bme.hu/doktisk/konf2013/papers/136-141.pdf

Beton repedéstágasság-mérési eredmények feldolgozása képdigitalizálási eljárással

A cikk bemutat egy új eljárást a beton próbatestek szerkezeti repedéseinek betonfedésen belüli folytonos repedéstágasság mérésére vonatkozóan, amely képdigitalizálási és digitális képfeldolgozási elveket alkalmaz. Bizonyítást nyer, hogy a szabad szemmel, skálázott repedéstágasság-mérő kézi nagyítóval, illetve a digitálisan rögzített képfelvételen az operátor által önkényes helyeken felvett repedéstágasság mérési eredmények mérési hibát hordozhatnak. A cikk rávilágít, hogy a beton szerkezeti repedéseinek tekervényessége csak a bemutatott eljáráshoz hasonlóan részletes képi elemzés útján határozható meg kellő pontossággal.
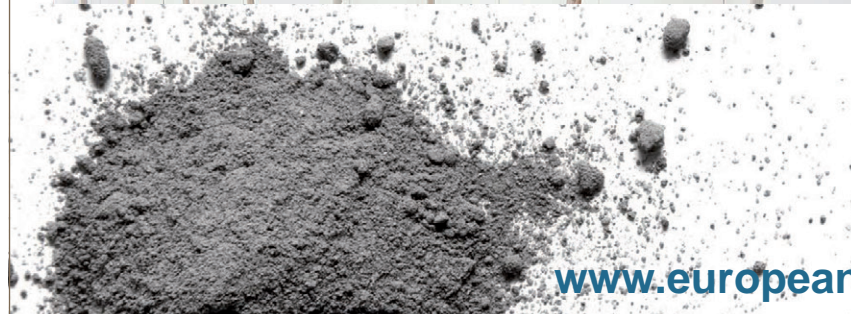Kulcsszavak: beton, repedéstágasság, digitalis képfeldolgozás, tekervényesség

Investigation and optimization of homogeneity of ceramic injection molding raw material to improve crack toughness of end product

Ádám EGÉSZ ▪ GE Hungary Ltd., Budapest, (Hungary) ▪ adam.egesz@ge.com,
László A. GÖMZE ▪ Department of Ceramics and Silicate Engineering,
University of Miskolc, Miskolc, (Hungary) ▪ femgomze@uni-miskolc.hu

Ádám EGÉSZ
Graduated in the University of Miskolc, Department of Ceramics and Silicate Engineering as a material engineer, where he actually continues his study as PhD student. In addition, currently he works for the GE Lighting as a project engineer, where he optimizes the manufacturing process of ceramic production for high intensity discharge lamps, especially the injection molding and its raw material. During his studies, he prepared several award-winning TDK papers.

Prof. László A. GÖMZE
Establisher (in July 1st, 1999) and head of Department of Ceramics and Silicate Engineering in the University of Miskolc, Hungary. Since then 7 students from the department have successfully completed their PhD theses and 4 of them were managed by Prof. Gömze. He is author or co-author of 2 patents, 5 books and more than 250 scientific papers. Recently, he is the chair of the International Organization Board of **ic-cmtp4** the 4th International Conference on Competitive Materials and Technological Processes (2016) and **ic-rmm2** the 2nd International Conference on Rheology and Modeling of Materials (2015).

Abstract

This study used capillary rheometer, gas densimeter and injection molding pressure measurement to quantitatively analyze the homogeneity of alumina based injection molding feedstock, and presents the report of the relationship between material homogeneity and kneading parameters, and the ration of different raw components. The researchers found as main result that the flux material has the highest effect on the homogeneity, since increasing the amount of this material can help in the equable mixing of alumina powder and paraffin wax. Furthermore, increasing the mixing time has positive effect on the homogeneity of the material, but much less than the amount of flux.

Keywords: alumina powder, paraffin wax, ceramic injection molding, densimeter, capillary rheometer, feedstock

1. Introduction

The procedures of ceramic injection molding (CIM) include four steps: kneading process, injection molding, debinding, and sintering. The CIM technology offers the opportunity to make complex and near-net-shape of ceramic parts. The kneading process is an important step in ceramic injection molding. The kneading stress offered by a sigma-blade kneader is quite enough, but in special cases with other kneaders it may be not enough to break down the powder agglomerates in the ceramic feedstock, especially, if the agglomerates are consisted of ultra-fine powder. The agglomerates are retained until sintering and become the fracture origin if the effective size of the defects is too large to withstand fracture stress [1, 2, 3]. Evans [4] reported a result of zirconia, which was fractured in a defect size greater than 10 μm. The fracture strength is not affected, if the agglomerates are smaller than 10 μm [4]. Recently, the fundamental and application issues of nanotechnology and micro-electromechanical system (MEMS) have evoked the interest toward ceramists. The precision microinjection molding makes the manufacturing of small parts possible for many advanced applications. The powder size must be reduced to produce thin and complex parts. The nanopowder tends to agglomerate due to van der Waal force. However, little attention for the kneading behavior of ceramic feedstock have been given in literature by using ultra-fine or nanopowder [5].

For producing ceramic arc tube parts (plugs), there are three different major components used for producing injection molding raw material (hereinafter *feedstock*): high purity alumina powder as the main component, an organic paraffin wax as a binder material, and flux material as surfactant.

After selecting a suitable powder and a binder system, the first processing step in CIM is to mix them to prepare an appropriate feedstock for molding and subsequent processing.

A homogeneous feedstock having high powder content is required to achieve a low shrinkage during binder removal and sintering. The feedstock should have the particles separated with a very thin layer of binder. To achieve this, powder agglomerates have to be dispersed in the binder [1, 2, 6].

With a homogeneous feedstock, in this experiment the main goals were to improve the quality of end product and to avoid the cracks and material discontinuities in the sintered ceramic parts (*Fig. 1*).
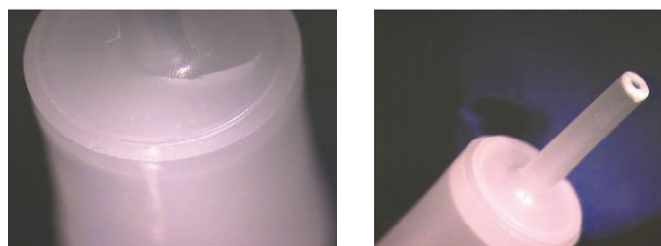

Fig. 1. Cracked (left) and intact (right) sintered alumina ceramic
1. ábra Repedt kerámia (balra) és ép kerámia (jobbra)

1.1. Possible options to determine the homogeneity of ceramic feedstock

In the case of the present experiments, the following measurement methods were chosen as output parameters of the grade of homogeneity: capillary rheometry, densiometry and pressure during injection molding. Literature mentions viscosity as a tool to determine the grade of homogeneity [7, 8, 9], but regarding the other two measurements it was not found to be advantageous for the determination of homogeneity during the present studies.

In the case of all three methods (described below) the same evaluation principle was followed: several samples were taken from the prepared material cell, and the standard deviation of

the measured values were investigated as an output parameter that can show the picture about the grade of material homogeneity and internal diversity [10].

1.1.1 Capillary rheometry

The shape of material is changing by the effect of external forces. Two ideal cases of deformation are known: elastic and viscous, which states can be mathematically well described by rheological state equations (constitutive equations) [11,12]. The Ostwald de Waele power law can follow the behaviour of injection molding feedstock, where the raising tension (τ) and the deformation speed (γ) are proportional to a power of n>0 natural number; see Eq. (1). Generally, in most of the cases n<1, so the viscosity of molten material decreases with the increasing deformation speed, at constant temperature (*Fig. 2*). This kind of material behaviour is pseudo-plastic: in this case the material is thinning by the shear stress.

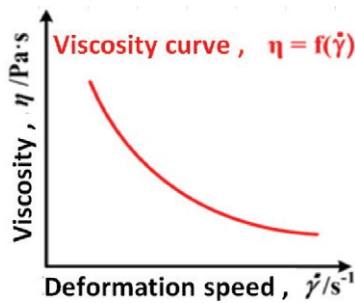$$\tau = K \cdot \dot{\gamma}^n \quad (n<1) \tag{1}$$

Fig. 2. Typical viscosity curve of pseudo-plastic materials
2. ábra A pszeudo-plasztikus anyagok tipikus viszkozitás ábrája[13]

The principle of capillary rheometry is the following: the measured material flows through a small diameter tube with relative small flowing velocity. Knowing the amount of material flow over given time, the pressure difference, and the geometry of the capillary (radius, length) the viscosity can be defined according to the Hagen - Poiseuille law; see Eq. (2) [13,14].

$$v = \frac{\pi(p_1 - p_2)}{8\eta l} r^4 t \tag{2}$$

where:
v: velocity of flow
p_1 and p_2: the pressure on the two ends of the capillary
η: viscosity
l: length of capillary
r: capillary radius
t: time

Considering the theory of determining homogeneity using viscosimetry, if the homogeneity of the material is increasing then the standard deviation of the viscosity values of samples is decreasing under constant temperature.

1.1.2 Densiometry

To determine the real density of ceramic feedstock a Quantachrome Ultrapyc 1200e densitometer (*Fig. 3*) was used with He gas system. The He gas for density measurements is used due to its small atomic size and high diffusion ability since it is able to penetrate into the smallest pores, even up to 0.2 nm. The densiometry is based on pycnometer volume determination, which is equal to the volume of displaced gas by the feedstock material (Archimedes law) and to the gas expansion technique (Boyle law). The volume of open pores can be defined with this method, but the closed or impenetrable pores can not be measured [15,16].

Fig. 3. Quantachrome 1200e type densiometer (left) and measuring cells (right)
3. ábra Quantachrome 1200e típusú sűrűségmérő berendezés (balra) és a hozzá tartozó mérőcellák (jobbra)

The standard deviation of measured density values can refer to the grade of homogeneity of feedstock since the mixed injection molding raw material consists of several components of different density. Namely, if some component did not mixed properly in the feedstock, then there can be a local enrichment from it, and so the measured density can be comparable with other samples, where there is no component enrichment; that may be considered a properly mixed raw material [16].

1.1.3 Injection molding pressure

The injection molding pressure is a parameter, which arises when the injection switches to holding pressure. In other words, this parameter is the maximum injection molding pressure during the injection process, which is needed for the filling of molding tool with a given quantity of material. The maximum speed of the material is defined by the gate between the injection unit and the injection tool, as a minimum cross-section (bottle-neck) [17,18].

Since the temperature, the minimum cross-section and the amount of material are constant, only the properties of material has influence on the flow of molten material, the change of the resistant force and so the injection molding pressure depends only on the flow behaviour of the material. In this way, one can get a similar capillary viscosimeter, in which the viscosity from the pressure against to the material flow can be estimated. And thus, from the standard deviation of pressure values, the homogeneity of feedstock can be determined as well.

The relationship between the two parameters is linear (*Fig. 4*).

The describing equation of the relationship with 92% probability is given by Eq. (3):
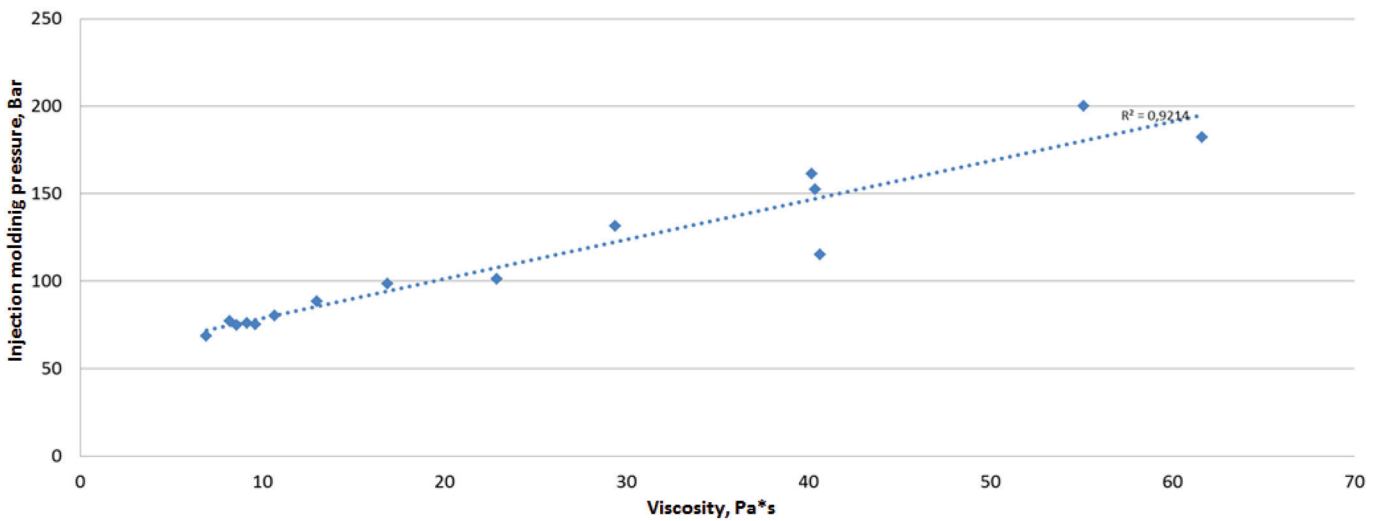y=2.2488x+56.287 (3)

Fig. 4. *The determined relationship between the capillary viscosity and injection molding pressure*
4. ábra *A meghatározott lineáris kapcsolat a kapilláris viszkozitásmérés és a fröccsnyomás értékei között*

This linear relationship between the two outputs shows, that one can get data about the homogeneity with the standard deviation of injection molding pressure of the feedstock produced with the given mixing parameters.

2. Experimental

The primary standpoint of the experiment is to discover the connection between the homogeneity of feedstock and the quality of end product, and to determine the homogeneity at all. To reach this goal, different mixtures were made with different processes and amounts of components.

To research the properties of homogenous feedstock, a design of experiment was made, using the MINITAB statistical software.

To analyse the main effects, the Plackett-Burman III resolution fractional factorial design of experiment was used [19,20,21]. Considering this, 4 factors were investigated at two levels: amount of flux material, mixing time, mixing temperature and the dosage of alumina powder during mixing.

In favor of control of reproducibility, repeatability and linearity, the centre point was repeated three times according to the design of experiment, and the full test was consisted of 15 different runs.

There were constant mixing volumes and weights run by run. The determination of the factor values was made by the operating levels and literature research. After the mixings, 5 samplings were carried out for each run.

3. Results and discussion

3.1 Determination of homogeneity

3.1.1 Results of capillary viscosimetry

The most important properties of an injection molding feedstock are the viscosity and homogeneity. According to the literature review, the high quality feedstock has low viscosity, and the viscosity does not change within manufacturing batch, that means the viscosity has low fluctuation, it was homogenously mixed [22,23].

The capillary viscosimetry measurements were carried aout by a laboratory Dynisco LMI 4000 type capillary rheometer, the measuring temperature was set to 68 °C, and the melting time was 360 seconds (*Fig. 5*). The measuring temperature was chosen to that of the temperature of injection molding of the test materials, to help the comparison of different test results. For the measurements, 3700 g pressing weight and 1.042 mm capillary diameter were chosen.

Fig. 5. *Dynisco capillary rheometer (left) and*
the viscosity measurement of feedstock (right)
5. ábra *Dynisco kapilláris viszkoziméter (balra) és*
a feedstock viszkozitás mérése (jobbra)

After the measurement, the equipment automatically displays the viscosity value based on the MFR (Melt Flow Rate). The measurements were repeated on five samples per batch, in this way the standard deviation values were possible to be determined. *Fig. 6* shows the influences of input parameters on the standard deviation of viscosity – so the dependence of homogeneity on the input parameters of mixing.

It can be seen, that the flux material has the strongest effect on the homogeneity, so if more flux is added into the feedstock, the standard deviation of viscosity becomes lower. The flux is

a surfactant in the system, so if the amount of alumina powder and paraffin wax is increased, then the components can be mixed with each other more effectively. Consequently, the wax can be able to coat the alumina more, and this can decrease the powder-powder friction, and the focus is placed to the wax-wax friction [24].

In addition, it can be observed, that the homogeneity is decreased with the increasing mixing time, but not so strong effect can be observed with the narrow variation intervals chosen, however, it is visible that with the increase of mixing time the components can mixed better with each other.

The dosage of alumina shows weak negative effect, however, it would be logical that the homogeneity is increasing if the dosage of powder is increasing. It can be noticed that the results are probably distorted by the noise of applied dosage method, namely, if there were more steps of dosage then more stops appeared in the mixing process and it would have a negative effect on the homogeneity and the efficiency of mixing. Nevertheless, it can be concluded that the continuous mixing is more important than the dosage in more steps. The dosage in more portions with continuous mixing together can improve quality.

3.1.2 Results of density measurements

The method of density measurement was the following. Sample was placed into the sample holder with constant weight, measurement was performed with 20 psi constant He gas pressure. Before the test 90 cleaning rinse were applied to eliminate the stuck air particles in the pores and on the surface of feedstock.

The equipment records 3 density values, and calculates the average of those. Five samples were taken and measured from the different feedstock runs, to be able to study the homogeneity of the composition of material from the standard deviation of the measurements. *Fig. 7* shows the dependence of the standard deviation of density on the input parameters of mixing.

It can be seen in case of this measurement method as well that the increase of flux material amount and mixing time results the standard deviation of density values to decrease, so the homogeneity of the feedstock increases. However, it can be seen here as well, that more steps of dosage does not result positive effect in the homogeneity, due to the same reasons mentioned above.

3.1.3 Evaluation of injection molding pressure measurements

The value of pressure during injection molding would be theoretically equal to the other two measurements before, since this measurement is an alternative capillary viscosimetry on account of constant and fixed cross-section, temperature, material velocity and material properties. In this case, the resistance of material was also measured during forcing trough the capillary. As it was expected, the pressure results are comparable to the results of the other two measurements (*Fig. 8*).
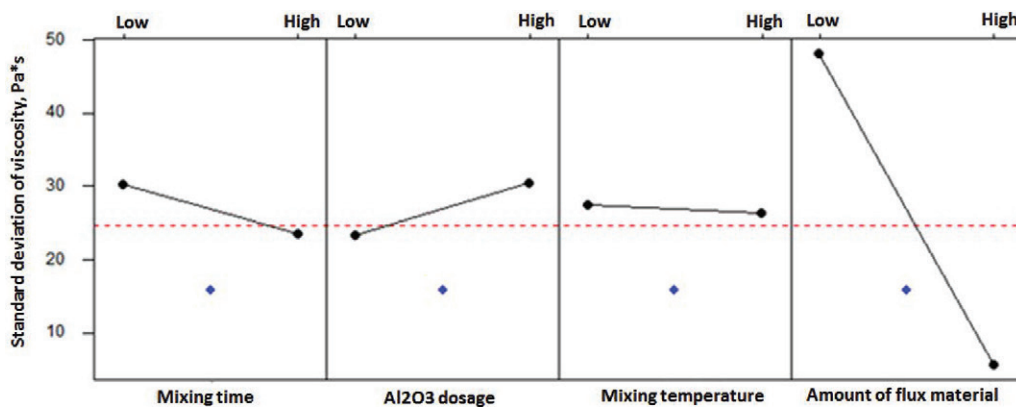

Fig. 6.   *Influences of input parameters on the standard deviation of viscosity*
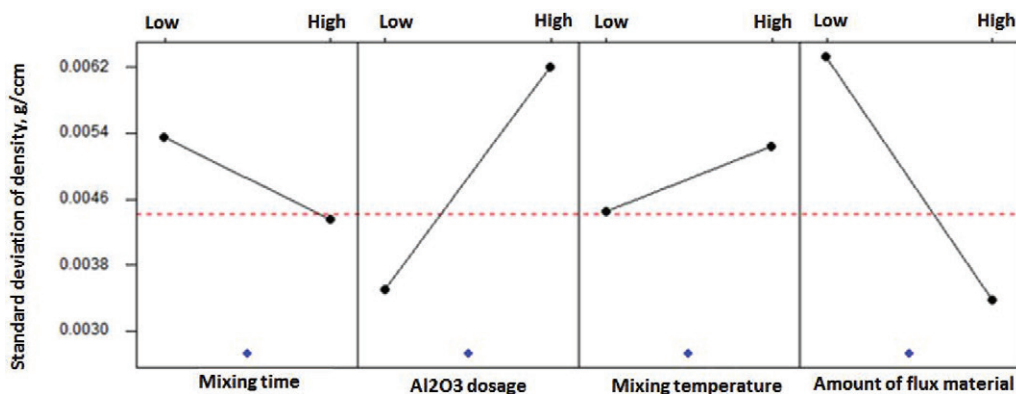6. ábra   *A feedstock viszkozitás szórásának függése az egyes bemenő paraméterektől*

Fig. 7.   *Influences of input parameters on the standard deviation of density*
7. ábra   *A mért sűrűség értékek szórása az egyes bemenő paraméterek függvényében*
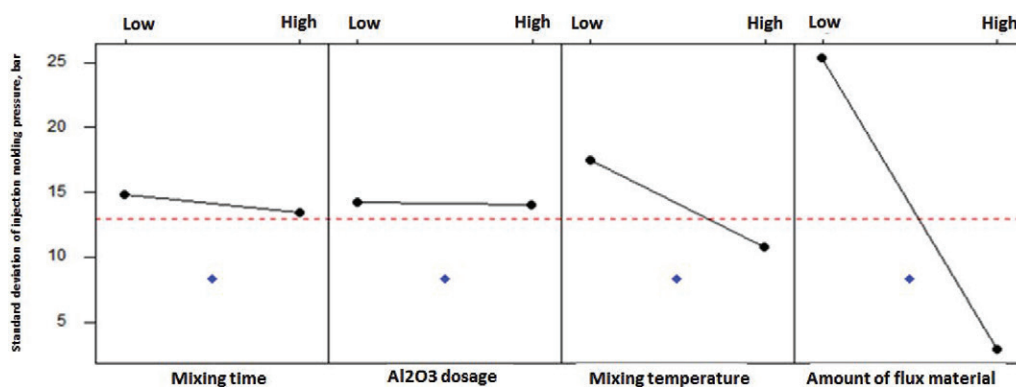
Fig. 8.   Influences of input parameters on the standard deviation of injection molding pressure
8. ábra   A fröccsöntési nyomás az egyes bemenő paraméterek függvényében
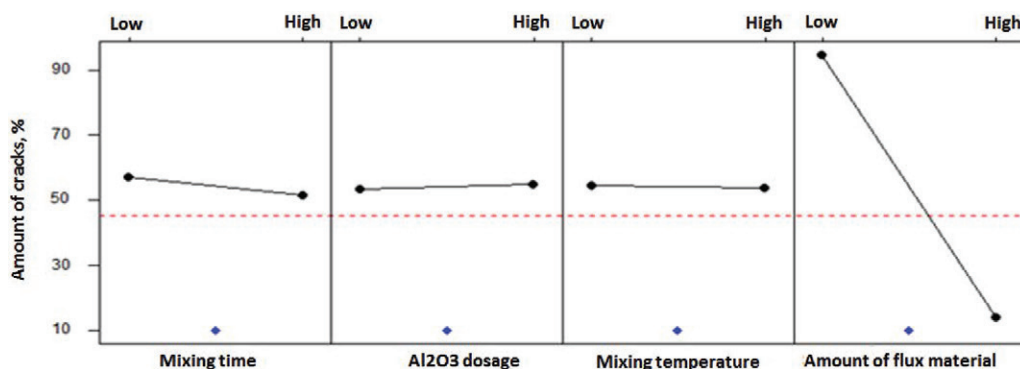

Fig. 9.   Susceptibility to cracking, depending on the input mixing parameters
9. ábra   Repedésre való hajlamosság az egyes bemenő paraméterek függvényében

In this case as well, the amount of flux dominates, although in this case one could observe the highest positive effect of the mixing temperature on homogeneity. However, this effect is not significant enough to enunciate that the mixing temperature has an influential role on the homogeneity within the interval variation studied.

3.2 Results of injection molding experiments

As a second step, after the determination of the homogeneity of different feedstocks, the injection molding was carried out. In this case the main question was the effect of homogeneity on the quality of the sintered end product, especially on the occurrence of cracks in the ceramic.

The samples of different runs were classified after the presintering and sintering processes, which results can be seen in *Fig. 9*.

In this case as well, the positive effect of the amount of flux is noticeable. The explanation is the same as before: the homogeneity of feedstock was improved, hereby less separated component remained in the mixture (whether powder or paraffin wax), which can cause cracks, voids or any heterogeneity in the sintered end product [25,13,14]. The other three factors did not have any significant effect on the amount of cracked products within the variation interval studied, except for the weak positive effect of mixing time.

4. Conclusions

The introduced test methods can be suitable to determine the grade of homogeneity of the ceramic injection molding raw materials.

With the defined mixing settings the homogeneity of raw material can be improved.

The flux material has the strongest effect on the homogeneity, since increasing the amount of this component can help homogeneous mixing of alumina powder and paraffin wax.

Increasing the mixing time has positive effect on the homogeneity of the material, but in a much less pronounced fashion than the amount of flux.

In the decrease of the amount of cracked ceramics, the mixing time and the amount of flux material were found to be the most effective input parameters.

References
[1] German, R. M. – Bose, A.: Injection Molding of Metals and Ceramics, *Powder Industries Federation*, 1997.
[2] Lin, S. T. P. – German, R. M.: The influence of powder loading and binder additive on the properties of alumina injection-molding blends. *J. Mater. Sci.*,Vol. 29, pp. 5367–5373,1994, http://dx.doi.org/10.1007/BF01171549
[3] Zhang, T. – Evans, J. R. G.: Predicting the viscosity of ceramic injection molding suspension. *J. Eur. Ceram. Soc.*,Vol. 5, pp. 165–172, 1989 http://dx.doi.org/10.1016/0955-2219(89)90032-0
[4] Evans, A. G. – Hhasselman, D. P. – Lange, F. F.: Fracture mechanics of ceramics. *Proceedings of the 3rd International Symposium on the Fracture Mechanics of Ceramics*, Vol 5, , pp. 789–792, 1983
[5] Song, J. H. – Evans, J. R. G.: The injection moulding of fine and ultra-fine zirconia powders. *Ceram. Int.*,Vol. 21, pp. 325–333, 1995 http://dx.doi.org/10.1016/0272-8842(95)96204-3

[6] Trunec, M. – Dobsak, P. – Cihlar, J.: Effect of powder treatment on injection moulded zirconia ceramics. *J. Eur. Ceram. Soc.*,Vol. 20, pp. 859–866, 2000, http://dx.doi.org/10.1016/S0955-2219(99)00222-8

[7] Onogi, S. – Mikami, Y. – Mtsumoto, T.: The rheology of suspension of titanate fiber in polymer solution. *Polymer Eng. Sci.*, Vol.17, pp. 1–8, 1977 http://dx.doi.org/10.1002/pen.760170102

[8] Kamiwano, M. – Kaminoyama, M. – Nishi, K. – Suziki, Y.: Power consumption diagram for wet particle kneader mixers in the case that rheological properties for wet particles cannot be measured. *J. Chem. Eng. Jpn.*, Vol. 33 (3), pp. 489–498, 2000, http://dx.doi.org/10.1252/jcej.33.489

[9] Kamiwano, M. – Kamiyonama, M. – Kawaguchy, Y.: Measurement of uniformity of mixture of wet particulate system by electrochemical method. *Sekiyu Gakkaishi*, Vol. 38, pp. 311–317, 1995 http://dx.doi.org/10.1627/jpi1958.38.311

[10] Okada, K. – Akasaka, S. – Akagi, Y. – Yoshioka, N.: In Proceedings of the XIth International Congress on Rheology. *Brussel, Beigium*, Vol 1, pp. 425–529, 1992

[11] Mohamad, N. H. – Muhamad, N. – Ismail, M. H. – Jamaludin, K. R. – Ahmad, S. – Ibrahim, M. H. I. : Flow behavior to determine the defects of green part in metal injection molding, *International Journal of Mechanical and Materials Engineering (IJMME)*, Vol. 4/1, pp. 70 -75, 2009

[12] Loebbecke, B. – Knitter, R. – Hausselt, J.: Rheological properties of alumina feedstocks for the low-pressure injection moulding process. Journal of the European Ceramic Society, Vol. 29, pp. 1595–1602, 2009 http://dx.doi.org/10.1016/j.jeurceramsoc.2008.11.001

[13] Zauner, R. – Binet, C. – Heaney, D. F. – Piemme, J. : Variability of feedstock viscosity and its correlation with dimensional variability of green powder injection moulded components. *Powder Metallurgy*, Vol. 47/1, pp. 1-6, 2004, http://dx.doi.org/10.1179/003258904225015473

[14] Zhang, T. – Evans, J. R. G.: Predicting the Viscosity of Ceramic Injection Moulding Suspensions. *Journal of the European Ceramic Society*, Vol. 5, pp. 165-172,1989, http://dx.doi.org/10.1016/0955-2219(89)90032-0

[15] Operation manual for Micro-Ultrapyc 1200e

[16] Soykan, H S. – Karakas, Y.: Preparation of Homogeneous Feedstocks for Injection Moulding of Zirconia-Based Ceramics. *Turk. J. Engin. Environ. Sci.*, Vol. 25, pp. 315-319, 2009

[17] Wei, Wen-Cheng J. – Wu, Rong-Yuan – Ho, Sah-Jai: Effects of pressure parameters on alumina made by powder injection moulding. *Journal of the European Ceramic Society*, Vol. 20, pp. 1301-1310, 2000 http://dx.doi.org/10.1016/S0955-2219(99)00295-2

[18] Sommer, F. – Walcher, H. – Kern, F. – Maetzig, M. – Gadow, R.: Influence of feedstock preparation on ceramic injection molding and.microstructural features of zirconia toughened alumina. *Journal of the European Ceramic Society*, Vol. 34, pp. 745–751, 2014 http://dx.doi.org/10.1016/j.jeurceramsoc.2013.09.020

[19] Barker, Thomas B.: Quality by Experimental Design. *Marcel Dekker Inc.*, 1985

[20] Cornell, John A.: Experiments with mixtures, 2nd Edition, *John Wiley and Sons*, Inc., New York, 1990

[21] Montgomery, Douglas, C.: Design and Analysis of Experiments, 3rd Edition, *John Wiley and Sons*, Inc., 1991

[22] Zauner, R. – Binet, C. – Heaney, D. F. – Piemme, J. : Variability of feedstock viscosity and its correlation with dimensional variability of green powder injection moulded components. *Powder Metallurgy*, Vol. 47/1, pp. 1-6, 2004, http://dx.doi.org/10.1179/003258904225015473

[23] Zhang, T. – Evans, J. R. G.: Predicting the Viscosity of Ceramic Injection Moulding Suspensions. *Journal of the European Ceramic Society*, Vol. 5, pp. 165-172, 1989, http://dx.doi.org/10.1016/0955-2219(89)90032-0

[24] Tseng, W. J. – Liu, D. – Hsu, C.: Influence of stearic acid on suspension structure and green microstructure of injection-molded zirconia ceramics. *Ceramics International,* Vol. 25, pp. 191-195, 1999 http://dx.doi.org/10.1016/S0272-8842(98)00024-8

[25] Szűcs, A. – Belina, K.: Rheological and thermal analysis of the filling stage of injection moulding. *EXPRESS Polymer Letters*, Vol. 6/8, pp. 672–679, 2012, http://dx.doi.org/10.3144/expresspolymlett.2012.71

Kerámia fröccsöntési alapanyag homogenitásának vizsgálata és optimalizálása a végtermék repedési szívósságának fokozása érdekében

Jelen kutatásban a szerzők ahhoz, hogy meghatározzák az adott keverési feltételekkel és különböző bemenő komponens mennyiségekkel előállított kerámia fröccsöntési alapanyag homogenitásának fokát, kapilláris viszkozimetriát, sűrűségmérést, valamint fröccsöntési nyomásmérést alkalmaztak. Legfőbb megállapításképpen elmondható, hogy a folyósító anyag mennyiségének változtatása volt a legnagyobb hatással a homogenitás növelésére, mivel ez az adalék tudja elősegíteni az alumínium-oxid por és a paraffin viasz minél egyenletesebb elkeveredését. Továbbá, a keverési idő növelésének pozitív hatása van az anyag homogenitására, de sokkal kisebb mértékben, mint a folyósító szernek.

Kulcsszavak: alumínium-oxid por, paraffin wax, kerámia fröccsöntés, kapilláris viszkozitás, sűrűségmérés, feedstock

Beszámoló a 2014. évi düsseldorfi Glasstec kiállításról

JAKAB András ▪ Ph.D. hallgató,
BME Építőanyagok és Mérnökgeológia Tanszék ▪ jakab.andras@epito.bme.hu
NEHME Kinga ▪ egyetemi docens,
DE MK, Építőmérnöki Tanszék; főmérnök Struktúra Kft. ▪ kpankhardt@yahoo.com
MOLNÁR Péter ▪ okl. építőmérnök, Struktúra Kft. ▪ molnar.peter.bme@gmail.com
Salem Georges NEHME ▪ egyetemi docens, laborvezető,
BME Építőanyagok és Mérnökgeológia Tanszék ▪ sgnehme@yahoo.com

### Review of the Glasstec 2014 exhibition in Düsseldorf

Traditionally, the Glasstec is organized in every second year in Düsseldorf and is the largest Glass exhibition in Europe. Connected to this trade fare, numerous international conferences organized as well: Solar Meets Glass, International Architecture Congress and Engineered Transparency International Conference at Glasstec, which are located in the Messe Düsseldorf exhibition and congress centre. The last conference has been organized for the third time which was the destination of the authors besides of the Glasstec. Present report focuses on the novelties of the Glasstec exhibition in year 2014 and the international scientific conferences from the aspect of civil engineering.

JAKAB András
PhD student at the BME, MSc Civil Engineer. Fields of interests: glass construction, glass columns, non-destructive testing methods, point-fixed glasses construction technology and management.

NEHME Kinga
MSc Civil Engineer, PhD, Associate Professor at the Department of Civil Engineering, University of Debrecen. Owner of Struktúra Ltd. engineering office (design, quality control). Member of the Technical committee of Glass Working Group (MSZT/MB 112) of Hungarian Standardization Institute; Hungarian Group of fib; Hungarian engineer chamber (MMK: 01-9160). Fields of interests: load bearing glasses, testing of construction materials, design, recycling of building materials.

MOLNÁR Péter
MSc Civil Engineer, designer at Struktúra Ltd. Fields of interests: fibre reinforced concrete, diagnostic of construction, glass construction.

Salem Georges NEHME
MSc Civil Engineer, PhD, Associate Professor at the Department of Construction Materials and Engineering Geology, Budapest University of Technology and Economics (BME). Member of the Technical committee of Glass Working Group (MSZT/MB 112) of Hungarian Standardization Institute; Hungarian Group of fib; Hungarian engineer chamber (MMK: 01-9159). Fields of interests: concrete technology, mass concrete, self-compacting concrete, fibre reinforced concrete, quality control of building materials, non-destructive testing, reinforced concrete structures, recycling of building materials.

1. Bevezetés

Düsseldorf Észak-Rajna-Vesztfália szövetségi tartomány fővárosa Németországban és az ország egyik jelentős pénzügyi és közlekedési központja. Ez is lehet az egyik oka, hogy hagyományosan minden második (páros) évben itt rendezik meg Európa legnagyobb üveges szakmai kiállítását a *Glasstec*-et, mely az idén 2014.10.21-24. között került megrendezésre. A város határához érve már óriás plakátokon (*1.ábra*) hirdetik a kiállítást és a pontos megközelíthetőségét.

1. ábra Glasstec kiállítást hirdető óriás plakátok, Glasstec északi bejáró épülete.
*Fig. 1.* Glasstec exhibition advertising billboards, the north entrance of the Glasstec Trade Fair.
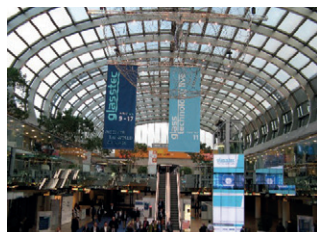
A *Glasstec* kiállításnak és konferenciáknak helyt adó rendezvény is egyben, amelynek helyszíne a *Messe Düsseldorf* kiállítási és konferencia központ, a Rajna partján a város északi felén. A szakmai kiállításon felül a látogatók számára számos élményt kínál a város önmaga is pl. a sokszínű, dinamikusan fejlődő *Medienhafen* városrész bebarangolásával, az üvegek iránt rajongók részére a *Stadttor* (*2.ábra*) lenyűgözően transzparens és monumentális épületének megtekintését javasoljuk, amely szabadon látogatható. A düsseldorfi *Stadttor* (Városkapu) érdekes szimbiózisa az üvegnek, az acélnak, a fának és a kőnek. A tervezők (Petzinka, Pink und Partner) ügyeltek arra, hogy a tartószerkezeti elemek is láthatóak maradjanak, növelve az átláthatóságot [1]. További érdekessége az épületnek a kettős homlokzat, a belső homlokzaton bükkfa és üveg, a külsőn pedig acél és üveg anyagok alkalmazása dominál.

2. ábra Stadttor, Düsseldorf (jobb oldalon a 240.5 m magas Rheinturm tévétorony).
Fig. 2. City gate of Düsseldorf (right-hand side is the Rheinturm TV tower with height of 240.5 m).

Düsseldorf-Hafen magyarul a düsseldorfi régi kikötő egykori épületeinek helyébe, ill. azok modernizálásával, látványos posztmodern épületeket építettek (3.ábra). A kikötő nyugati részén még ipari területek találhatóak, ahová a jövőben *high-end* lakóparkot terveznek építeni.
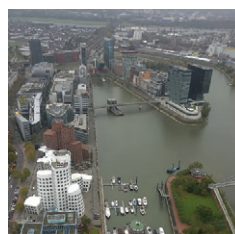
3. ábra Bal oldali kép: Düsseldorf Medienhafen városrész látképe a Rheinturm tévétorony 170 m magasan lévő kilátó szintjéről (látható a híres épületegyüttes, melyet Frank O. Gehry építész tervezett); Jobb oldali kép: Rheinknie híd, (tervezője: F. Leonhardt).
Fig. 3. Left-hand side: View of Medienhafen in Düsseldorf from the Rheinturm at the level of 170 m (famous buildings designed by Frank O. Gehry); Right-hand side: Rheinknie bridge (designer: F. Leonhardt).

Düsseldorf környékének híres bronzszínű alkoholos sör itala az *altbier*, amely a helyi sörfőzők receptje szerint felső erjesztéssel készül: meleg erjesztést követően, hosszabb ideig hideg helyen tárolják, mert alacsony hőmérsékleten jobban tisztul.

## 2. Nemzetközi konferenciák a Glasstec rendezvényen

A *Glasstec* üvegipari kiállításhoz [2] számos nemzetközi konferencia kapcsolódik: *Solar Meets Glass, International Architecture Congress* és *Engineered Transparency International Conference at Glasstec*, amelyek helyszíne szintén a *Messe Düsseldorf* kiállítási és konferencia központ. Az utóbbi konferenciát, – amely a szerzők egyik úti célját is jelentette a szakmai kiállítás mellett, – immár harmadik alkalommal rendezték meg. A kétnapos konferenciára feljogosító jegy egyben ingyenes belépőnek számít ugyanazokon a napokon a *Glasstec* kiállítási részére is. Az említett konferenciák közül az *Engineered Transparency* áll legközelebb az építőmérnökök érdeklődési területéhez, melyen *Jakab András* (BME) is előadást tartott. A két nap alatt hozzávetőlegesen 70 db előadást hallhattunk, közel 200 résztvevő 26 országot képviselt (*4. ábra*).
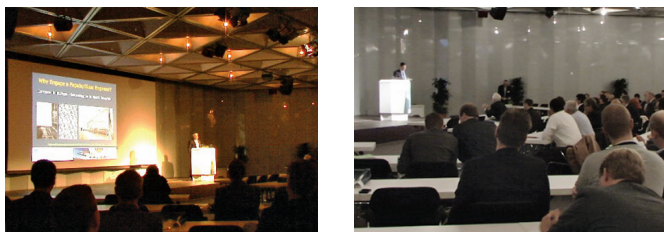
4. ábra   Engineered Transparency konferencia helyszíne.
Fig. 4.   Venue of Engineered Transparency conference.

A Drezdai és Stuttgarti Műszaki Egyetemek által szervezett konferencia délelőtti megnyitói után két-két meghívott előadó számolt be a munkájáról, kutatásaikról illetve az üveg, mint szerkezeti anyag jövőjéről. Az első előadó *Dr. Jan Knippers* a Stuttgarti egyetem Szerkezettervezési Intézetének vezetője, aki „Transparency in construction through digital workflow" *(Átlátszóság az építésben a digitalizált munkafolyamatok világában)* címmel tartott előadást. *John Kooymans* Kanadából érkezett, hogy bemutassa északi-amerikai példákon keresztül olyan épületek tervezésének és építésének lebonyolítását, amelyek több sarkalatos műszaki kihívást jelentenek (Glacier Skywalk, Jasper Nemzeti Park, Kanada; Ismaili Centre, Toronto). Az amerikai *Cristoph Timm* „Glass works", azaz „Üveg munkák" címmel tartott előadást a Skidmore, Owings & Merrill LLP (SOM) vállalat egy-két nagyobb méretű projektjéről, középpontba helyezve az üveg szerepét és alkalmazási lehetőségeit, valamint figyelembe véve az új innovatív technológiákat a tervezésben és a kivitelezésben egyaránt (pl. Chhatrapati Shivaji nemzetközi repülőtér, Mumbai). Az előadó bemutatta a chicagói Skydeck üvegpárkányának tervezési szempontrendszerét, mozgatási és tisztítási lehetőségeit is. *Winfried Heusler* (Schueco, Németország) a jelen és a jövő üveghomlokzat fejlesztéseit mutatta be három példán keresztül, tervezési és kivitelezési szempontok alapján. A példák között szerepelt az isztambuli Reneszánsz Torony bonyolult geometriával rendelkező homlokzatrendszere, ahol a tervezésben egy új paraméteres rendszert alkalmaztak a geometriai optimalizáláshoz.

Az előadásokat követően a konferencia három részre, külön előadó termekbe tagolódott, ahol a következő szekciókat lehetett meghallgatni: „Üveg és szerkezeti fa"; „Szerkezeti üvegek"; „Homlokzat és építészeti tervezés". Az „Üveg és szerkezeti fa" szekció a két anyagnak az együttdolgozási lehetőségeit tárta fel. Több előadás is „I" tartók kísérleti vizsgálatával foglalkozott, ahol az „I" tartó övei fából, míg gerince üvegből voltak. Más kutatások arra irányultak, hogy miként viselkedik a két anyag együtt, ha a megszokott üveghomlokzat nem alumínium anyagú megtámasztó rendszerrel dolgozik együtt (pl.: Schüco), hanem az alumínium zártszelvényeket fára cseréljük ki. Ezen kutatásokban vizsgálták kísérletekkel a hőtechnikai tulajdonságokat, hőre történő alakváltozások hatásait, valamint statikai teherbíró képességeit is a szerkezeteknek. A „Szerkezeti üvegek" szekció meglehetősen változatos témákat vonultatott fel, mely szekcióban hazánkat képviseltük. Többek között szó esett több szempontból is egyedülálló központosan terhelt üvegoszlopokról, ahol kísérleti és végeselemes modellezéseket is végeztek (*5. ábra*).
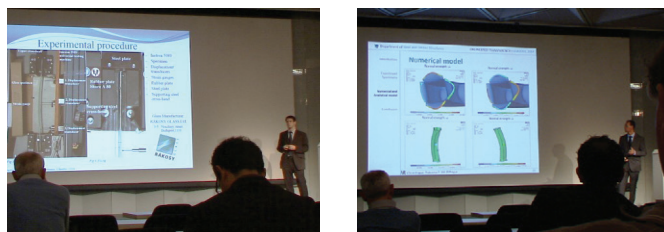
5. ábra   Engineered Transparency konferencia, „Szerkezeti üvegek" szekciója.
Fig. 5.   Structural glass section of Engineered Transparency conference.

Sokan foglalkoztak a hidegen hajlított üvegek tulajdonságaival is, a kiállításon bemutattak egy 2,4 m hosszú 0,8 m széles és 5 m-es rádiuszra hajlított üveget, melyre szenzorokat telepítettek, felosztva a felületet cellákra és a terheléssel egy időben nagyméretű kijelzőn mutatták be a leginkább terhelt felületi cellákat az adott feszültségekkel együtt (terhelési próba volt pl.: személyek áthaladása; *6. ábra*).
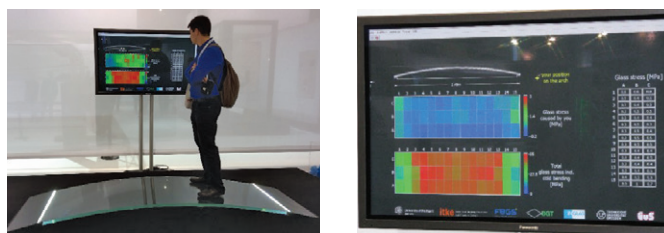
6. ábra   Integrált száloptikai szenzorokkal ellátott hidegen hajlított üveg.
Fig. 6.   Cold bent glass with integration of fiber optic sensors.

A további kutatásokban az előadók vizsgálták többek között az alkalmazott fóliák hatását a maradó teherbírásra, valamint rendkívüli terhekre pl.: robbanás által keltett légnyomásra. „A homlokzat és építészeti tervezés" szekcióban előadást tartottak a felületi paraméteres tervezési rendszerekről, az akusztikai tulajdonságokról és a hangterhelés csillapítási lehetőségeiről, valamint szó volt az üveghomlokzatok által áteresztett fény és átláthatóság tervezéséről is. A konferencia rendkívül sokszínű volt, hiszen a kísérletező tudományos kutatások mellett szakmai felüdülésnek számított a megvalósult ultramodern illetve a jövőben tervezett épületek bemutatása is.

A konferencia nyitónapjának estéjén a *Glasstec* aznapi zárása után egy exkluzív körútra invitálták a konferencia résztvevőket, ahol a Stuttgarti Műszaki Egyetem által kiállított feszített üveghídról is tartottak egy rövid előadást, habár a kiállítás idejében le volt zárva, a konferencia résztvevők ráléphettek az üveghídra, amely növelte az üveggel szembeni személyes megbízhatósági tapasztalatainkat is.

Két év múlva rendezik meg ismét az *Engineered Transparency* konferenciát 2016. szeptember 20–21-én szintén párhuzamosan a *Glasstec* kiállítással. A bővebb tájékoztatás érdekében a konferencia honlapját tudjuk ajánlani: *www.engineered-transparency.eu* [3] valamint az idei konferencia kiadványt (ISBN 978-3-86780-402-8), melyben a korábban említett témák még bővebben, alaposabban is tanulmányozhatóak.

3. Üvegipari újdonságok és modern üvegszerkezetek a kiállításon

A kiállítás a különféle szakterületek szerint, tematikusan tagozódott, átfogó és színes képet nyújtott a termékek, megmunkálási technológiák és szolgáltatások területén. Az „Intelligens üvegek" témakörében bemutatásra kerültek az üvegipari fejlesztések, intelligens épülethéjak, homlokzat és energia valamint divatos elnevezésén az „üveg design". Hangsúlyos témakörök voltak: az üveggyártás folyamatának optimalizálása és a termékminőség; vékony üvegek gyártása (megmunkálási és erősítési technológiák); innovatív üvegek az építésben (pl. funkcionális bevonatok, többrétegű hőszigetelő üvegek, napelemek, hajlított üvegek, ki/be kapcsolható üvegek), műszaki üvegek (pl. LED, LCD, száloptika, sugárzásvédő üvegek); csomagolóipari üvegek (pl. gyógyszerészeti és laboratóriumi üvegek); kézműves üvegtermékek; üvegek újrahasznosítása.

A következő alfejezetekben a mérnöki üvegszerkezetnél is fellelhető üvegipari újdonságokat mutatjuk be.

3.1. Vékony üvegek

Üvegipari újdonságként mutatkozott be Xensation® Cover néven a SCHOTT *kémiailag edzett alumínium-szilikát üvege* (*7. ábra*). A kémiailag edzett üveg különösen nagy hajlító szilárdsága lehetővé teszi vékony üvegek (pl. 0,56 mm) gyártását is. Jellemzően nagy a karcolással szembeni ellenállása és tartóssága. A tiszta, igen vékony átlátszó üveg felhasználási területe jelenleg a magas ára miatt inkább csak a kijelzők üvegezésénél terjedt el. Véleményünk szerint a mérnöki alkalmazásokban külső héjként valamint védőréteg szerepét töltheti be a jövőben pl. a laminált üvegek területén (*8. ábra*).

7. ábra   SCHOTT kémiailag edzett alumínium-szilikát üvege.
Fig. 7.   Chemical strengthened alumina-silicate glass from SCHOTT.

8. ábra   Vékony laminált üvegek alkalmazása: mozgatható, összecsukható tető, Gorilla Glass, Corning Incorporated, USA (egy réteg vastagsága 0.7 mm; a laminált üveg: 5 kg/m²).
Fig. 8.   Application of thin laminated glass: movable, foldable roof, Gorilla Glass, Corning Incorporated, USA (thickness of a layer: 0.7 mm; weight of laminated glass: 5 kg/m²).

3.2. Nagyméretű üvegek

A kiállításon nagy feltűnést keltettek a szokványos gyári alapüvegek Jumbo méretét is meghaladó *különlegesen nagyméretű üvegek*. A SEDAK GmbH & Co. KG (Németország) kiállított 3,2 m × 14 m-es üvege, többrétegű és keramikus digitálisan nyomtatott bevonattal mintázott is volt egyszerre. A cég a fejlesztései és beruházásai eredményeképpen ma már képes ilyen nagyméretű üvegek edzésére, laminálására és felületi mintázására 3,2 m × 15 m üveg méretig.

9. ábra   Nagyméretű laminált üvegek, Sedak cég terméke.
Fig. 9.   Large-scaled laminated glass, product of Sedak Ltd.

NorthGlass (Kína) is kiállította a 3,0 m × 11,2 m nagyméretű üvegét, mely 2×12 mm vastag, biztonsági laminált üveg volt ún. low iron HS 70 bevonattal ellátva. A NorthGlass cég által gyártott legnagyobb elérhető üvegméret a 3,3 m × 18,0 m. Tájékoztatásul megjegyezzük, hogy a kiállított üveg tömege 2 tonna!

10. ábra   NorthGlass cég Low-E HS hőszigetelő üveg terméke.
Fig. 10.   Low-E HS insulation glass, product of NorthGlass Ltd.

A Glas Marte Gmbh (Ausztria) bemutatta a világon egyedülálló önhordó, hidegen alakított hőszigetelő üvegét (*11. ábra*), mely kétoldali megtámasztással akár 12 m fesztávot is képes áthidalni. Ezt úgy tudták elérni, hogy hidegen hajlított *vékony membrán üvegrétegek között*, optimalizált és egyben szabadalmaztatott geometriájú távtartókat alkalmaztak.

Megjegyezzük, hogy az ilyen nagyméretű üvegek mozgatása, szállítása és beépítése rendkívüli körültekintést igényel az építésben résztvevő minden féltől, továbbá korszerű, gépesített anyagmozgatás is szükséges. A csomópontok kialakításánál a nagyméretű üvegek hőmozgásaira is megfelelő figyelmet kell szentelni.

3.3. Feszített szerkezetek

Transzparens üvegszerkezetek fejlesztésében vesznek részt közösen és mutatták be a Drezdai Műszaki Egyetem Épületszerkezeti Intézetének valamint a Thiele Glas Werk és KL-megla GmbH munkatársai a *feszített tartószerkezetüket*. Az átlátszó üvegszerkezetek fejlesztéseit a Német Gazdasági és Energiaügyi Minisztérium is kiemelten támogatja. A kiállított 1,2 m széles, járható feszített üvegszerkezet 9 m-es fesztávú, melyet a két oldalán, 2×2×12 mm-es VSG üveglapok között futó 24 mm-es átmérőjű sodronykötél feszített alá (*12. ábra*). A feszítés hatására a húzott üveg élbe bevitt nyomó igénybevétel segítségével teherbírás növekményt sikerült elérniük. Az esetleges tönkremenetelkor, a feszítőkábelek hatására a szerkezet maradó teherbírása is kedvezően alakul.

11. ábra   Membrán
           hőszigetelő üveg.
Fig. 11.   Insulating glass
           membrane.
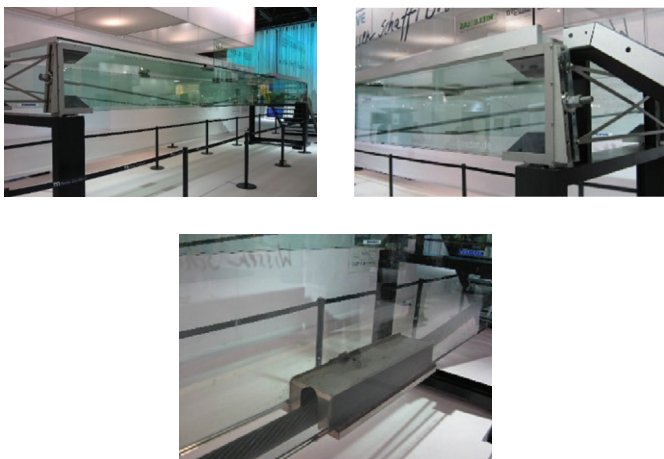
12. ábra   9 m-es fesztávú járható feszített üvegszerkezet.
Fig. 12.   Prestressed glass bridge with 9 m span.

3.4. Tenzigrid szerkezetek

A TVT GmbH és a Pizai Egyetem közösen mutatták be szabadalmaztatott üvegtartójukat, mely elnevezése „*Trave Vitrea Tensegrity*" (*13. ábra*). A tartó előfeszített acél kötelek által tartott síküveg lapokból épült fel, abból a célból, hogy az üvegben ébredő húzófeszültségeket csökkenteni tudják. A szerkezet megfelel a biztonságos tervezési alapelveknek, mivel e több elemből felépülő rendszerben kicsi a valószínűsége annak, hogy egyszerre több elem tönkremenetele is bekövetkezzen, így egy-egy elem esetleges teherbírásának kimerülése nem veszélyezteti a tartó egészét és az kellő maradó teherbírással rendelkezhet. Véleményünk szerint az elgondolás

helyes, azonban némileg ellentmondásba ütközünk, a jelenlegi tendenciákat megfigyelve, mely az egyre növekvő méretű üvegeket preferálja. A fejlesztők a kiállításon vízszintes és függőleges üveg teherhordó szerkezetek prototípusait is bemutatták (*14. ábra*).

13. ábra   „Trave Vitrea Tensegrity".
Fig. 13.   „Trave Vitrea Tensegrity".

14. ábra   Térbeli üveg elemekből felépülő oszlop.
Fig. 14.   Column made up from spatial glass elements.

### 3.5. Lamináló anyagok a maradó teherbírás tükrében

Az egy rétegű üveg rideg anyag, tönkremenetelét követően maradó teherbírással nem rendelkezik. Az építési üvegek szerkezetekben való alkalmazásakor, a *maradó teherbírás* biztosítása sarkalatos pont a mérnökök számára. Az előző fejezetekben bemutatott szerkezeteknél is e kérdést helyezik a középpontba a fejlesztésekkor. A laminált üvegek esetében a megfelelő maradó teherbírás eléréséhez kellő szívóssággal és szakítási jellemzőkkel bíró lamináló anyagok kiválasztása nagyon fontos. A kiállításon számos lamináló anyag gyártó bemutatkozott, azonban a *faraone* cég (Olaszország) a SentryGlas® Plus (SGP fólia) és az XLAB fóliával gyártott termékein, példával is illusztrálta a fóliák hatását a laminált üvegek maradó teherbírására (*15. ábra*).


15. ábra   Előtető üvegezésének tönkremenetelt követő viselkedése a különféle lamináló fóliák hatására (legfelül: SGP+40 kg/m, középen: XLAB+80 kg/m, alul: szokványos fóliák).
Fig. 15.   Post facture behaviour of glass canopy with use of different interlayer foils (in the top: SGP+40 kg/m, in the middle: XLAB+80 kg/m, in the bottom: conventional foils)

3.6. Fejlesztések a privát szféra védelmében

Az üveg, mint építőanyag egyik legfontosabb tulajdonsága az átlátszósága, ill. transzparenciája. E tulajdonsága sok esetben előnyös (pl. természetes fény belső térbe juttatása), azonban néha negatív tulajdonság is lehet, amennyiben a külső szemlélődők nem kívánt tekintetébe ütközünk és az átláthatóság a saját személyes, privát szféránkat is zavarhatja. Az üveget belső térelhatárolókban alkalmazva gyakran úgy érezhetjük, hogy eltűnt a privát szféránk és feszélyezve érezhetjük magunkat, ill. bizonyos eseményeknél pl. tárgyalások, pénzügyi tranzakciók bonyolításához szükséges lehet a beláthatóság kiküszöbölése, akár ideiglenesen is. Erre a feladatra fejlesztették ki a funkcióját tekintve *ki/be kapcsolható üvegezéseket* (*16. ábra*), melyet a kiállításon számos cég bemutatott. Az ún. LC filmben lévő kristályok (liquid crystal = folyadékkristály) feszültség hatására egy irányba rendeződnek és ezáltal a filmréteg átlátszóvá válik. Újdonságnak számított a funkcionális termékcsaládnál az egy üvegtáblán belül, több szakaszra oszthatóan működő, akár automatizált ki/be kapcsolási lehetőség (*17. ábra*).
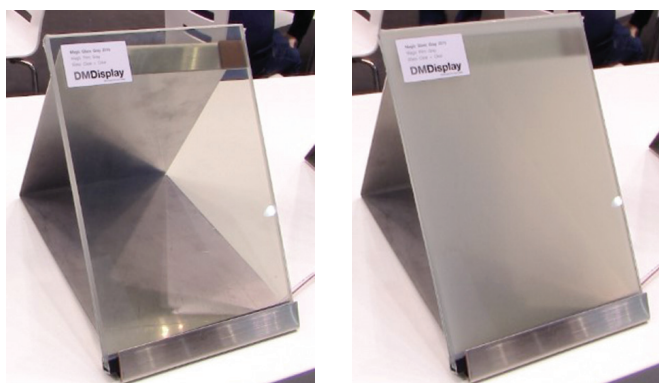

16. ábra   DMDisplay ki/be kapcsolható üvege.
Fig. 16.   Off/on switchable glass, product of DMDisplay.
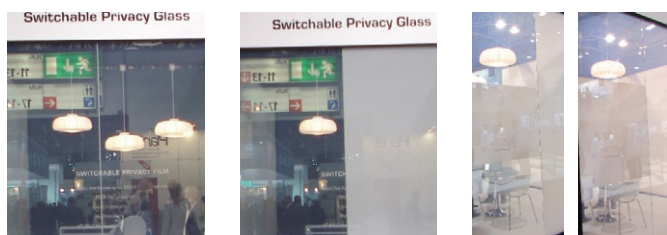
17. ábra   Részlegesen ki/be kapcsolható üvegezés.
Fig. 17.   Partially off/on switchable glass.

3.7. „Játékos" üvegek, lézertechnológia

A kiállítás legszínpompásabb csarnoka az *üvegművészeti alkotásoké* volt, ahol a játékos formáktól az ötletesen kivitelezett síküveg lapokból összeállított térbeli alkotásokig minden fellelhető volt (*18-19. ábrák*). Manapság, nem jelent technikai akadályt, hogy az üveglapok belsejében alkosson a művész mintázatokat, mivel a lézertechnológia segítségével ma már akár ipari méretekben is lehetséges. A mérnökök számára köztudott, hogy az üveg felületére felvitt mintázatok – akár savmaratással, homokfúvással vagy a beégetett keramikus bevonatok – csökkentik az üveg szilárdságát. Kérdés merül fel, hogy üvegszerkezeteknél, üveg térelhatárolóknál a jövőben alkalmazott pl. lézertechnológiával, az üvegek belsejébe bevitt mintázat milyen hatással van az üveg szilárdságára?
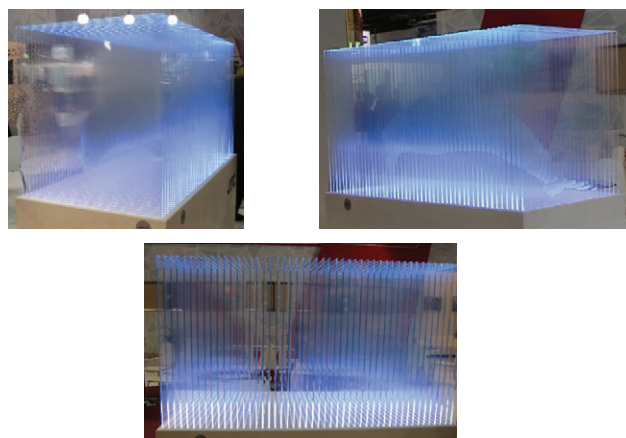
18. ábra   Belugát ábrázoló sík üveglapokból álló térbeli alkotás (JYC).
Fig. 18.   Spatial glass art consisting of plane glasses, illustrating a beluga whale (JYC).

19. ábra   A „betonos szíveket" is megmelengető üvegművészeti alkotások.
Fig. 19.   Glass art which can warm the heart of a concrete expert as well.

4. Kitekintés

A *Glasstec*-el szorosan együttműködnek más konferenciák is, amelyek hirdették magukat pl.: GPD (*Glass Performance Days*). A GPD konferencia sorozat, szintén világszinten hirdeti és reklámozza az üveget, mint építőanyagot. A GPD 2015 szervezői Düsseldorfban is jelen voltak és az óvárosban biztosítottak lehetőséget a kiállítóknak és cég képviselőknek valamint a konferencia résztvevőknek, hogy oldottabb körülmények között teremthessenek (üzleti) kapcsolatokat az ún. GPD Pubban, melynek kötetlen hangulatát mi is élvezhettük.

A 2014. évi *Glasstec* körültekintő szervezői arról is gondoskodtak, hogy a telefonokra a *Glasstec*-hez kapcsolódó alkalmazást is le lehetett előzetesen tölteni, hogy a keresett standok illetve cégek pozícióját könnyedén beazonosíthassák a látogatók. Az alkalmazás a cégkeresőn kívül még részletesebb információkat is tartalmazott pl.: a cégprofilról, elősegítette, hogy minden látogató eljusson az érdeklődési körének megfelelően a kiállító cégekhez.

A szerzők remélik sikerült az olvasók figyelmét e beszámolóval felkelteni a két évente Düsseldorfban megrendezésre kerülő *Glasstec*-re, és mások is kedvet kapnak és ellátogatnak a nemzetközi kiállításra és konferencia rendezvényre.

Hivatkozások

[1] http://www.stadttor.de/gebaeude
[2] http://www.glasstec.de
[3] http://www.engineered-transparency.eu/cms

GUIDELINE FOR AUTHORS

The manuscript must contain the followings: title; author's name, workplace, e-mail address; abstract, keywords; main text; acknowledgement (optional)**; references; figures, photos with notes; tables with notes; short biography** (information on the scientific works of the authors).

The full manuscript should not be more than 6 pages including figures, photos and tables. Settings of the word document are: 3 cm margin up and down, 2,5 cm margin left and right. Paper size: A4. Letter size 10 pt, type: Times New Roman. Lines: simple, justified.

TITLE, AUTHOR
The title of the article should be short and objective.
Under the title the name of the author(s), workplace, e-mail address.
If the text originally was a presentation or poster at a conference, it should be marked.

ABSTRACT, KEYWORDS
The abstract is a short summary of the manuscript, about a half page size. The author should give keywords to the text, which are the most important elements of the article.

MAIN TEXT
Contains: materials and experimental procedure (or something similar), results and discussion (or something similar), conclusions.

REFERENCES
References are marked with numbers, e.g. [6], and a bibliography is made by the reference's order. References should be provided together with the DOI if available.
Examples:
Journals:
[6] Mohamed, K. R. – El-Rashidy, Z. M. – Salama, A. A.: In vitro properties of nano-hydroxyapatite/chitosan biocomposites. *Ceramics International.* 37(8), December 2011, pp. 3265–3271, http://dx.doi.org/10.1016/j.ceramint.2011.05.121
Books:
[6] Mehta, P. K. – Monteiro, P. J. M.: Concrete. Microstructure, properties, and materials. *McGraw-Hill*, 2006, 659 p.

FIGURES, TABLES
All drawings, diagrams and photos are figures. The **text should contain references to all figures and tables**. This shows the place of the figure in the text. Please send all the figures in attached files, and not as a part of the text. **All figures and tables should have a title**.
Authors are asked to submit color figures by submission. Black and white figures are suggested to be avoided, however, acceptable.
The figures should be: tiff, jpg or eps files, 300 dpi at least, photos are 600 dpi at least.

BIOGRAPHY
Max. 500 character size professional biography of the author(s).

CHECKING
The editing board checks the articles and informs the authors about suggested modifications. Since the author is responsible for the content of the article, the author is not liable to accept them.

CONTACT
Please send the manuscript in electronic format to the following e-mail address: femgomze@uni-miskolc.hu and epitoanyag@szte.org.hu or by post: Scientific Society of the Silicate Industry, Budapest, Bécsi út 122–124., H-1034, HUNGARY

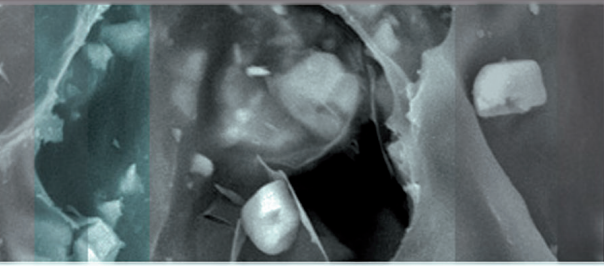**We kindly ask the authors to give their e-mail address and phone number on behalf of the quick conciliation.**

ic-rmm2

2nd INTERNATIONAL CONFERENCE ON RHEOLOGY AND MODELING OF MATERIALS
in Miskolc-Lillafüred, Hungary, 5-10 October, 2015.

Welcome to ic-rmm2

We are pleased to announce the organization of the 2nd INTERNATIONAL CONFERENCE ON RHEOLOGY AND MODELING OF MATERIALS to be held near city Miskolc in mountain Bükk in one of the most beautiful places of Hungary in Hunguest Hotel Palota Lillafüred, October 5-10, 2015.
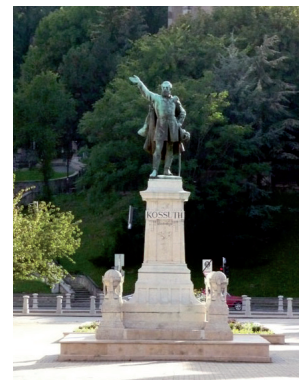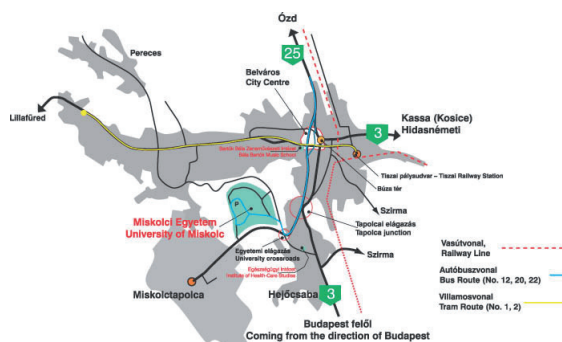
The idea to organize in Hungary the 2nd International Conference on Rheology and Modeling of Materials we have received from prospective scientists, physicists, chemists, mathematicians and engineers from Asia, Europe, North and South America including China, India, Japan, Korea, Russia, Turkey, Estonia, France, Italy, United Kingdom, Chile, Mexico, USA. As organizers we hope that you will attend on ic-rmm2 and we are looking forward to welcome you on this international conference in Miskolc-Lillafüred, Hungary. Event ic-rmm2 is sponsored by several universities, scientific journals, societies and organizations around the World.

The objectives

The aims of the 2nd International Conference on Rheology and Modeling of Materials are the fostering of interdisciplinary collaboration and interaction among scientists, researchers, PhD students as well as product and technology developer engineers. The international conference ic-rmm2 provides a platform among leading international scientists, physicists, chemists, mathematicians, researchers, PhD students and engineers for discussing recent achievements in measurement, modeling and application of rheology in materials technology and materials science of liquids, melts, solids, powders, crystals and amorphous structures.

Among the major fields of interest are the influences of temperature, mechanical stresses, deformation speeds and times on rheological properties, material structures and phase transformation of foams, emulsions, suspensions, liquids, powders, crystals, foods, cosmetics, polymers, plastics, petrochemicals, melted metals, glass and competitive materials like nanomaterials, pharmaceuticals, medical- and biomaterials, ceramics, films and coatings, advanced metal alloys, composites, hetero-modulus, hetero-plastic and hetero-viscous complex material systems, hybrid materials, ... etc.

Multidisciplinary applications of rheology as well as mechanical and rheological modeling in material science and technology encountered in sectors like food, bio- and medical materials, ceramics, glass, thin films, polymers, clays, construction materials, energy, aerospace, automotive and marine industry. Rheology in physics, chemistry, medicine, biosciences, cosmetics, environmental and earth sciences and in engineering and industries are of particular interests.

Further information can be obtained from Prof. Dr. László A. Gömze by e-mail femgomze@uni-miskolc.hu

Sustainability & the Environment

Glass is a sustainable, fully recyclable material which provides great environmental benefits such as contributing to mitigating climate change and saving precious natural resources. It is also highly appreciated in many applications for its inert nature and its contributions to safeguarding people's health and well being.

Mitigate climate change

In many of its application glass can help to save energy. It is most obvious in the case for insulating glass for windows and facades but also for less known products such as weight-lightening reinforcement glass fibre used in automotive, aviation and other transport modes to reduce the weight of vehicle and their fuel consumption.

Glass is also used to generate renewable energy through solar-thermal and photovoltaic applications and wind turbine, which largely profit from light weight reinforcement glass fibres.

Save natural resources

Glass is a resource efficient material which is made of abundant natural raw material such as sand and glass waste (cullets). Glass is a fully recyclable material that can be recycled in close loop over and over again.

This is particularly true for glass bottles which on average have a recycling rate varying from 50% to 80%. Thanks to glass recycling, significant amounts of raw materials are saved and natural resources are preserved. Glass recycling also helps in saving energy as cullets melt at a lower temperature than raw materials. Consequently, less energy is required for the melting process.

In other glass sectors, considerable efforts are made to recycle glass after use even though each sector has its own specialities and quality requirements. The amount of solid waste produced by the glass industry during manufacturing is extremely low as almost all glass waste (cullets) are immediately recycled and put back to furnaces to serve as raw material.

Safeguard people's health and well-being

Glass is among the preferred materials not only for its aesthetics but also for its own characteristics. Glass preserves taste and vitamins. As an inert material, it guarantees that food and beverages placed in glass containers are not stained by the packaging. It is also commonly used in the pharmaceutical industry to preserve the properties of medicines. In another side of the medical sector, optical glass helps improve the vision of millions of Europeans.

In construction as well, architects not only use large glazed areas for their energy-saving properties but also because they provide natural light into buildings which enhance living and working conditions of occupants. Studies show that glass in buildings, through all these benefits, contribute to people's well-being and improved health conditions.

Contact us